

Design and Analysis of Capacitive Micromachined Ultrasound Transducer

by

Mohammad Hadi Motieian Najar

B.A.Sc., The University of British Columbia, 2008

A THESIS SUBMITTED IN PARTIAL FULFILLMENT OF
THE REQUIREMENTS FOR THE DEGREE OF

MASTER OF APPLIED SCIENCE

in

The Faculty of Graduate Studies

(Electrical and Computer Engineering)

THE UNIVERSITY OF BRITISH COLUMBIA

(Vancouver)

September 2010

© Hadi Najar, 2010

Abstract

Capacitive Micromachined Ultrasound Transducers (CMUTs) have been recently introduced as a viable substitute to piezoelectric transducers in medical ultrasound imaging. CMUT possesses advantages such as allowing high frequency, having wide bandwidth, high sensitivity, low cost, CMOS compatibility and being easy to fabricate.

This thesis is motivated by movement towards a better detection of breast tumors using ultrasound imaging techniques, which CMUTs have promised to achieve. Therefore, CMUTs were designed to fulfill requirements of this application in terms of resonant frequency, pull-in voltage and geometrical dimensions. The entire design and analysis were performed considering that the CMUTs are to be fabricated using PolyMUMPs technology, for this technology being precise, accurate and well established in the micro-electromechanical systems (MEMS) community.

CMUTs were first analytically modeled and designed by exploiting the parallel-plate capacitor equations. A behavioral model was developed in VHDL-AMS, which, unlike previous models, incorporates the non-linear electromechanical relations of the CMUT. The behavioral model has the advantage of being more time efficient than finite element models (FEM) and more accurate than analytical models.

Prior to fabrication, a 3D FEM was developed in COMSOL Multiphysics® software. Resonant frequency analysis determined the frequency response and eigenfrequencies of the CMUT, which could not be determined using previous models. Parametric analysis determined the pull-in voltage, the spring constant and spring softening effect, the variation in capacitance and the electromechanical efficiency of the CMUT. The CMUT resonated at 5.868MHz frequency and

the collapse voltage was determined at 275V using FEM results, which were close to analytical modeling results and in excellent agreement with behavioral modeling results. The thickness and the radius of the circular CMUT membrane were found to be 1.5 μm and 32 μm , respectively. The air/vacuum gap distance was 0.75 μm and the insulation layer was 0.6 μm .

The CMUTs were fabricated in cell and array form. An array of 128 elements each containing 118 cells were fabricated to be compatible with existing ultrasound probes. Unfortunately, due to mal-fabrication by the company, which was experimentally proved, the experimental results were not as successful.

Table of Contents

Abstract.....	ii
Table of Contents	iv
List of Tables	vi
List of Figures.....	vii
Acknowledgements	xi
Dedication	xii
1 Introduction.....	1
1.1 Background on CMUTs and Ultrasounds	2
1.2 Advantages of CMUTs over Piezoelectric Materials.....	4
1.3 Research Motivation.....	5
1.4 Objectives and Methods	6
2 Modeling of CMUT.....	9
2.1 Principle of Operation of CMUT.....	9
2.2 Analytical Modeling of CMUT	11
2.2.1 Collapse Voltage Calculation.....	15
2.2.2 Resonant Frequency Calculation.....	20
2.2.3 Spring Softening Coefficient.....	25
2.2.4 Electromechanical Coupling Effect	29
2.3 Electromechanical Equivalent circuit of CMUT	31
3 Simulation.....	36
3.1 Finite Element Simulation of CMUT	36
3.1.1 CMUT Model Setup.....	37
3.1.2 Eigen Frequency Analysis and Frequency Response.....	41
3.1.3 Parametric Analysis.....	44
3.1.3.1 Pull-in Phenomenon	44
3.1.3.2 Spring Softening Effect	49
3.1.3.3 Electromechanical Coupling Coefficient.....	52

3.2 Behavioral Modeling with VHDL-AMS of CMUT	53
3.2.1 Frequency Analysis	55
3.2.2 Pull-in Analysis	56
4 Fabrication.....	59
4.1 Previously Fabricated Processes.....	59
4.1.1 Surface Micromachining	60
4.1.2 Bulk Micromachining	63
5 Testing and Characterization	71
5.1 Experimental Setup.....	71
5.1.1 Electrical Testing Setup	71
5.1.2 Mechanical Testing Setup	73
5.1.3 Acoustical Testing Setup.....	75
5.2 Experimental Results	77
6 Conclusions and Future Work.....	82
6.1 The Road Ahead	84
References.....	86
Appendices.....	92
Appendix A – COMSOL Multiphysics Simulation Setup for Parametric Analysis	92
Appendix B – Images of CMUT Masking Layouts, Fabricated Devices, and Pin Configuration	98

List of Tables

Table 1. Combinations of layers in PolyMUMPs to fabricate CMUT	18
Table 2. List of important parameter values	23
Table 3. List of important parameters to design the CMUT calculated analytically	35
Table 4. Summary of FEM and behavioral results and their relative errors.....	58
Table 5. Rectangle parameters in COMSOL	93
Table 6. Boundary settings for electrostatics in COMSOL	95
Table 7. Boundary settings for moving mesh in COMSOL	95
Table 8. Subdomain settings for solid, stress-strain in COMSOL.....	96

List of Figures

Figure 1. Cross-section of a basic unit of a CMUT	10
Figure 2. Principle of operation of a CMUT cell in (a) transmission mode and (b) receiving mode.....	11
Figure 3. First order lumped electromechanical model of a CMUT.....	12
Figure 4. Electrostatic and spring forces as a function of gap distance in analytical modeling of CMUT when $V_{DC} < V_{collapse}$ [27]	16
Figure 5. Electrostatic and spring forces as a function of gap distance in analytical modeling of CMUT when $V_{DC} = V_{collapse}$ [27]	17
Figure 6. The relationship between pull-in voltage and the radius of the CMUT membrane	20
Figure 7. Relationship between the resonant frequency and the radius of the CMUT membrane	23
Figure 8. Analytical pull-in voltage versus resonant frequency of the CMUT membrane.....	25
Figure 9. The effect of spring softening when increasing bias DC voltage on (a) resonant frequency and (b) apparent spring constant.....	28
Figure 10. Variation of kinetic energy with respect to applied harmonic voltage component.....	31
Figure 11. Two-port schematic of a moveable plate capacitor[15]	32
Figure 12. Full electromechanical equivalent circuit of CMUT [15].....	33
Figure 13. (a) Finite element model setup in COMSOL showing half of CMUT cell, (b) Simplified cross-section of the CMUT cell model[15].....	38
Figure 14. Fully coupled electro-mechanical simulation algorithm for non-linear devices[48] ..	39
Figure 15. FEM analysis of an electrostatic bar using (a) standard method and (b) moving mesh technique[48].	40
Figure 16. First five eigen frequency modes of the designed CMUT membrane (a)-(e) and the meshed structure (f). The eigen frequencies are (a) 5.86 MHz, (b) 12.21 MHz, (c) 20.02 MHz, (d) 22.83 MHz, (e) 29.73 MHz.....	42
Figure 17. The frequency response of the CMUT membrane	43

Figure 18. Membrane displacement versus DC bias voltage illustrating the collapse/pull-in phenomenon for FEM model.....	45
Figure 19. Shape of the membrane for increasing DC bias voltages. The curves progress from top to bottom in steps of 5V from 80V-270 V.....	47
Figure 20. Capacitance of a CMUT with increasing DC bias voltage in steps of 5V from 5V to collapse voltage, 270V.....	48
Figure 21. Spring constant of a CMUT cell versus increasing DC bias voltages depicting spring softening effect.....	50
Figure 22. Decrease in resonant frequency versus increasing DC voltage for FEM shown by solid line and analytical modeling shown with dashed line	51
Figure 23. Electromechanical coupling coefficient of a CMUT cell versus increasing DC bias voltage from 5V to pull-in voltage.....	52
Figure 24. Modified diagram of the CMUT as a moveable plate capacitor attached to a mechanical spring-damper system [15].....	54
Figure 25. Complete Simplorer circuit used for transmission simulations[15].....	55
Figure 26. Power density frequency responses of CMUT for (a) air transmission and (b) water transmission[15].....	56
Figure 27. CMUT membrane displacement versus increasing DC bias voltage indicating pull-in phenomenon[15].....	57
Figure 28. Surface micromachining (sacrificial release process) of CMUT cell, (a) substrate doping, deposition of insulation layer (LPCVD Si_3N_4), deposition of first sacrificial layer (LPCVD poly-Si), (b) deposition of second sacrificial layer, (c) patterning the CMUT shape, (d) deposition of membrane, (e) create release holes, (f) membrane release (wet etch KOH) (g) sealing membrane (LPCVD Si_3N_4), (h) depositing top electrode and patterning [16].....	62
Figure 29. Bulk micromachining (wafer bonding process) of CMUT cells, (a) thermal oxide growth on the prime wafer and defining the cavity using photolithography and patterning step (b) growth of a second oxide layer for insulation purposes (c) direct bonding of SOI wafer to the prime silicon wafer (d) removal of top silicon layer and the buried oxide layer to release the membranes (e) sputtering metal and using photolithography and patterning step to form electrodes (f) photolithography and etching silicon to define elements [16].....	64
Figure 30. Cross sectional view of 7 layers of PolyMUMPs process [59].....	65

Figure 31. Cross sectional view of a CMUT cell showing fabrication process in PolyMUMPs, (a) deposition of silicon nitride on a doped substrate, (b) deposition of poly-silicon layer and photolithography patterned to be used as bottom electrode and membrane posts, (c) depositing oxide layer as sacrificial layer, (d) deposition and photolithography patterning a poly-silicon layer as top membrane, (e) creating etch holes and releasing the membrane by removing the oxide layer.....	67
Figure 32. Cross sectional view of simplified fabrication process in PolyMUMPs, (a) deposition of silicon nitride as insulation on a doped substrate, (b) deposition of a poly-silicon layer and photolithography patterned to be used as membrane posts, (c) deposition of an oxide layer as sacrificial layer, (d) deposition and photolithography patterning a poly-silicon layer as top membrane, (e) creating etch holes and releasing the membrane by etching the oxide layer using HF	69
Figure 33. Packaged CMUT chip	70
Figure 34. Schematic of experimental setup to measure input impedance [61]	72
Figure 35. Complete experimental setup to mechanically characterize a CMUT cell	74
Figure 36. Experimental setup for pulse-echo measurement [64]	76
Figure 37. I-V curve of the CMUT cell structure with nitride insulation.....	77
Figure 38. I-V curve of the CMUT cell structure without Nitride insulation.....	78
Figure 39. The X profile of a CMUT cell with insulation between the electrodes.....	80
Figure B1. (a) Masking layout and, (b) fabricated device of a CMUT cell with a layer of metal atop and using substrate as the ground electrode.....	98
Figure B2. (a) Masking layout and, (b) fabricated device of a CMUT cell structure using the substrate as the ground electrode	98
Figure B3. (a) Masking layout and,(b) fabricated device of CMUT cells with different radii and using substrate as the ground electrode	99
Figure B4. (a) Masking layout and, (b) fabricated device of CMUT arrays and the ground pad100	
Figure B5. (a) Masking layout and, (b) fabricated device of CMUT arrays and their interconnecting tracks	101
Figure B6. Photos of CMUT cells with burnt tracks after high current I-V characterization indicating presence of short-circuit on the dies	102
Figure B7. Pin configuration and the interconnecting tracks to the bond pads	103

Figure B8. PGA 209 package pin layout 104

Acknowledgements

I would like to wholeheartedly appreciate my parents and my siblings for their unconditional help, feedback and support throughout my entire life. Without them, traveling this road would have been impossible. I acknowledge Dr. Seyyed Mohammad Soleimanpanah for his unbounded spiritual education and awareness that guided me in the proper direction of life.

I offer my enduring gratitude to my supervisor, Professor Edmond Cretu, for his thorough guidance, patience and constant support, financially and academically, throughout my graduate studies. I would like to wholeheartedly thank him for his presence whenever a question was raised or an unexpected problem occurred.

I would like to thank Professor Robert Rohling for helping me with his extensive knowledge on ultrasound imaging systems and applications as well as encouraging me in this research path. I acknowledge Professor Shahriar Mirabbasi for his constant help and profound insight about CMOS world and answering all the questions I had in that regard, and Professor Tim Salcudean who kept my head in the big picture about ultrasound imaging systems. My acknowledgments would not be complete without thanking Professor Kenichi Takahata and professor Boris Stoeber, for providing me with experimental equipment throughout my research at UBC.

I must appreciate the support and feedback of my respected friends and colleagues, Hussein Al-Chami and Ellie Sarraf, who helped me in exploring novel ideas in my research, Sultan Mohammad for training me with μ EDM, Samuel Frew, Parisa Behnamfar and Wei You with their knowledge contributions in this project. In addition, I would like to acknowledge the support of Leo Hwang in COMSOL Multiphysics and other two organizations: Ultrasonix, and Natural Sciences and Engineering Research Council of Canada (NSERC).

Dedication

To My Mother,

*Who has always been there for me, and to whom I owe everything
what so little I have achieved!*

Chapter 1

Introduction

Long before the technology for constructing very small machines were discovered, their potentials were appreciated. When Richard Feynman's famous lecture in 1959 at CalTech, "There's Plenty of Room at the Bottom", were publicized, no one believed one day we could be living among these small machines without noticing them. Micro Electro-Mechanical Systems (MEMS) are influencing our lives and changing our way of living. From micro-gyroscopes in iPhones to ultrasound transducers in ultrasound machine probes, MEMS structures play important roles. Recently, a relatively new transducer technology called Capacitive Micromachined Ultrasound Transducer (CMUT) has emerged from MEMS research community. CMUT is thought to be a viable substitute to piezoelectric materials in medical ultrasound imaging machines.

In this introductory chapter, a background on CMUT and its applications are given. Reasons for why CMUTs are viable substitutes of piezoelectric materials in ultrasound imaging are also discussed. Eventually, the motivation that inspired the research, the objectives and methods are presented.

1.1 Background on CMUTs and Ultrasounds

Ultrasound is an imaging tool with many applications from nondestructive testing to medical imaging. About 100 year ago ultrasound waves were considered initially for underwater navigation. When Lord Rayleigh introduced his writings on the theory of sound, and the Curie brothers discovered the piezoelectric effect in 1800s the science of acoustic sensing drew more attention. During World War I, acoustical devices were used for underwater detection of large objects such as submarines. In the 1930s ultrasound entered the medical field and was used initially as medical therapy tool for tissue heating. In the 1940s, ultrasound transmission was used as an imaging tool for detecting tumors. Later, pulse-echo ultrasound imaging was discovered and enabled scientists to image soft tissues. As electronics improved during the 1970s, electronic coupled transducer arrays replaced fixed-focus mechanical sector scanners. The improvement in technology enabled a more enhanced resolution and more rapid ultrasound imaging. More detailed information on background of ultrasound imaging and transducers can be found in [1-4].

Piezoelectric crystals, polymers, ceramics and piezocomposite materials have dominated the ultrasonic transducer technology even though the idea and the concept of electrostatic actuation is not relatively new compared to piezoelectric transducers. Piezoelectric materials are exploited to generate and detect acoustic waves in the sonic and ultrasonic frequency range. Capacitors were discovered to be a suitable alternative to piezoelectric materials in acoustic applications. They are mainly used to detect acoustic waves in audio applications such as microphones. However, as Langevin predicted, in order to be able to compete with piezoelectric materials, a high electric field was required to be generated across the plates of the capacitors to force them to actuate[2]. According to Paschen Law, to be able to generate high electric field strength in

capacitors without any breakdown one needs to achieve small gaps. Recently, as microfabrication techniques advanced in MEMS area, they have enabled the MEMS research community to achieve small gaps enabling the capacitor transducers to be a capable competitor of piezoelectric transducers. The first generation of micromachined electrostatic transducers – or capacitive transducers – were manufactured and reported in the 1980s [5],[6]. These electrostatic transducers were not well characterized and their performances were not as good as their piezoelectric counterparts. As more advanced fabrication technologies emerged in the MEMS community, improved versions of capacitive micromachined ultrasound transducers with submicron gaps were fabricated and characterized [7]. Extensive research has been done on CMUTs since the introduction of microfabrication techniques, and CMUT technology continues to improve [8-11].

Although CMUTs can be used in many acoustics applications, its application to medical ultrasound imaging is predominant. CMUT is a promising MEMS device, which has inspired researchers and scientists to explore real-time volumetric ultrasonic imaging as well as enhancing the resolution of this imaging modality. The key to this solution is to design and fabrication of 2-D CMUT arrays. These 2-D arrays can also be integrated with electronics using flip-chip bonding to control the transducers. Some of these goals have been achieved [12],[13] and some improvement and optimization yet remain to be explored. The next section discusses the main advantages of CMUTs over piezoelectric materials and why CMUTs are viable alternatives to conventional transducers and continue to be promising.

1.2 Advantages of CMUTs over Piezoelectric Materials

Although piezoelectric transducers have been used for many years, CMUT offers many advantages that make them a viable substitute for piezoelectric transducers. Using piezoelectric transducers, especially in medical applications, are a bit challenging due to the impedance mismatching problem. For instance, the characteristic impedance of piezoelectric ceramic is ~ 33 MRayl, which is considerably larger than that of tissues like blood and fat (~ 1.6 MRayl). One of the main advantages of CMUT, which makes it a good alternative to piezoelectric transducer, is the low impedance of its thin membrane. Having low impedance in CMUT eliminates the need of using matching layers[14].

Another significant advantage of CMUT technology is its wider bandwidth and sensitivity than piezoelectric transducers, enabling CMUTs to generate ultrasound images with higher resolution[15]. The increased bandwidth in CMUT does not only increase the resolution but also offers the ability to design new image modality analysis tools[16]. Tissue harmonic ultrasonic imaging is an important area of research in medical imaging, where the generated ultrasound wave is transmitted at a fundamental frequency and the image is formed from the second harmonic received[17],[18]. The other important feature of CMUT is its capability of generating very high frequency ultrasound waves. High frequency applications, such as intravascular ultrasound imaging (IVUS), can exploit and benefit from this CMUT feature into its small probes. High frequency CMUT elements have been fabricated in the range of 60 MHz and successfully tested[19-21].

The CMUT is able to be fabricated using similar technologies to those used for fabricating integrated circuits (IC). This advantage gives CMUT the potential of being fabricated with a CMOS layer on the same chip, and could eliminate, for example, the need of having wiring

between the ultrasound probe and the rest of the ultrasound system in ultrasound machines. Fabricating large 2D transducers requires a significant amount of wiring, which is one of the limitations in achieving high resolution, real-time 3D ultrasound imaging[22]. The improved MEMS fabrication technologies makes it possible to fabricate CMUTs in a much smaller scale than piezoelectric transducers and hence achieve smaller devices. Other advantages of CMUT include ease of fabrication and operation over a wider range of temperatures[23].

1.3 Research Motivation

Ultrasound imaging forms about 25% of clinical imaging techniques. As a soft-tissue imaging modality, ultrasound has the advantages of being inexpensive and rapid compared to other imaging modalities such as Magnetic Resonance Imaging (MRI). Furthermore, it does not use any unsafe radiation (e.g. ionizing radiation) such as X-rays and computed tomography (CT). Ultrasound imaging is by far the safest imaging tool in medical clinics[24]. However, due to the previously mentioned disadvantages of piezoelectric transducers, such as high characteristic impedance, some limitations on ultrasound imaging are present. Therefore, the focus of research on CMUT technology was on designing and analyzing an alternative technology to piezoelectric transducers to improve medical ultrasound imaging. As discussed in the previous subsection, CMUT was an achievable substitute, which offered advantages such as wider bandwidth, ease of fabrication, integration with microelectronics, better electro-acoustic coupling, and higher sensitivity than piezoelectric transducers[14],[23].

Ultrasonic imaging is used in many areas such as obstetric sonography for pregnancy, cardiology, ophthalmology, intravascular ultrasound and tumor detection. In October 2009, the BC Cancer Agency reported that “One woman in nine will develop breast cancer in her lifetime

if she lives to age 80” and that the most common cancer in women in BC is breast cancer. Thus, it seemed appropriate to tune CMUT parameters to be able to generate ultrasound waves in a range suitable for detecting breast tumors. In summary, this thesis focuses mainly on designing and analyzing CMUTs in the frequency range of 5MHz to 9MHz as well as presenting various approaches in fabricating this MEMS device.

1.4 Objectives and Methods

The main parameters to design, analyze and fabricate the CMUT are:

- **Frequency range:** as discussed in section 1.3, the frequency of the CMUT needs to be approximately in the range of 5MHz to 9MHz. The ultrasound penetration depth in tissue is inversely proportional to the frequency of the ultrasound waves. This frequency requirement ensures ultrasound waves can penetrate to the desired distance to be able to image the entire breast.
- **Low pull-in voltage:** CMUT is usually biased with a DC voltage to increase its sensitivity. The closer the bias voltage to pull-in voltage, the higher the sensitivity one can achieve. Therefore, to be able to obtain the maximum sensitivity, the CMUT needs to be biased at a DC voltage close to its pull-in voltage. A lower pull-in voltage means lower power consumption and attaining higher sensitivity faster, easier and safer.
- **Feasibility of Fabrication:** the fabrication of CMUT requires precise alignments and submicron thick layers. To be able to construct a transducer probe, CMUTs also need to be fabricated in array form. Thus, using a suitable fabrication technology to facilitate batch fabrication is a crucial requirement. A fabrication technology, which provides this

requirement, is PolyMUMPs (MEMSCAP, Inc. NC, USA). Other novel in-house fabrication approaches using polymers were as alternatives.

The design methodology will use a top-down hierarchical approach, with different levels of design and simulation. This work began with analytical modeling of the CMUT to meet the previously mentioned criteria. Analytical modeling provides preliminary design parameters of CMUT. The analytical modeling was performed using MATLAB/MAPLE(Mathworks, Natick, MA, U.S.A). To obtain a more accurate and realistic design, finite element simulations (FES) were performed using COMSOL Multiphysics © (COMSOL AB, Stockholm, Sweden). As an intermediate step, a behavioral model was developed before performing lengthy FES and costly fabrication to optimize the performance of CMUT. The behavioral model was developed in VHDL-AMS (IEEE Std 1076.1-1999) using Simplorer software (Ansoft, LLC, Pittsburgh, PA, USA). Eventually, mask layouts were generated according to parameters obtained from analyses and sent for fabrication. The PolyMUMPs process was used for CMUT fabrication, for the technology is stable, well characterized, and gives the ability to check the design methodology and the performance of the transducers. Note that all the analyses were performed taking into consideration that the device will be fabricated with PolyMUMPs technology.

The novelty of this research is to come up with a thorough design and simulation of the CMUT behavior besides its fabrication. CMUT cell was linearly modeled and its static behavior was simulated in MATLAB. The inherent non-linear property of CMUT was simulated in COMSOL Multiphysics© FEM software. A third novel approach was introduced to model the behavior of CMUT using VHDL-AMS. The CMUT was fabricated using PolyMUMPs technology using poly-silicon as the lower electrode and the poly-silicon membrane as the top electrode.

This thesis is organized as follows: in the second chapter the basic CMUT structure and its principle of operation are introduced. This chapter also presents an analytical model and electromechanical equivalent circuit of a CMUT based on piston-like movement of parallel plate capacitors. Chapter 3 shows thorough finite element analyses of a CMUT cell. Analyses such as eigenfrequency, frequency response, static, and parametric analysis were performed and discussed. This chapter also presents the behavioral modeling of CMUT in VHDL-AMS and compares the finite element modeling (FEM), analytical modeling and behavioral modeling results. Chapter 4 illustrates a few previous fabrication technologies of CMUTs as well as new fabrication approaches. Chapter 5 discusses the experimental setups and results of fabricated CMUTs , and Chapter 6 describes the future work, possible improvements and a summary of the important results of this promising technology.

Chapter 2

Modeling of CMUT

Before investing in fabrication, it is required to model the CMUT and obtain the crucial parameters such as geometry dimensions. To become more familiar with CMUTs, this chapter first introduces principle of operation of the MEMS device. It then presents the analytical modeling of CMUT to extract important parameters using software such as MATLAB and MAPLE. Moreover, the CMUT electromechanical equivalent circuit is presented. The equivalent circuit analysis allows identifying the figures of merit that determine the transducer performance. All the analyses were performed considering that the device will be compatible with PolyMUMPs process, a precise and well-established fabrication technology.

2.1 Principle of Operation of CMUT

The basic unit of CMUTs is called a CMUT *cell*. As shown in figure 1, a CMUT cell consists of a supported membrane, the air/vacuum gap, the top and bottom electrodes and a substrate. The membrane is suspended over a substrate and is separated by a small gap. Two electrodes are usually embedded in - or deposited on - the membrane and the substrate.

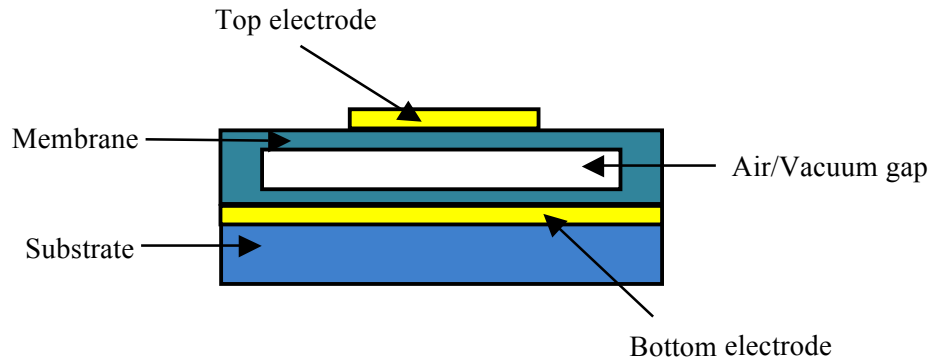


Figure 1. Cross-section of a basic unit of a CMUT

The principle of operation of CMUT is based on electrostatic force between the top and bottom electrodes. When a voltage is applied between two electrodes, the Coulomb force causes the electrodes to attract each other. If the bottom electrode, which resides on the substrate, were kept stationary, the electrostatic force would displace the suspended membrane as it is attracting the top electrode. When an alternating voltage is applied, the membrane would vibrate and generate acoustic waves into the medium with which the moving plate is in contact.

CMUT can be used both in transmission and receiving modes. In actuating mode, the CMUT is usually biased by applying a DC voltage between the two electrodes. The DC bias voltage electrostatically attracts the membrane towards the substrate and increases the mechanical sensitivity. An AC voltage is then superimposed to actuate the membrane and create acoustic waves. In sensing mode, the acoustic pressure on the membrane causes a mechanical displacement and results in a change in capacitance between the electrodes. Therefore, an AC signal can be detected if a proper readout circuitry is used. Figure 2 illustrates this principle of operation in transmission and receiving modes.

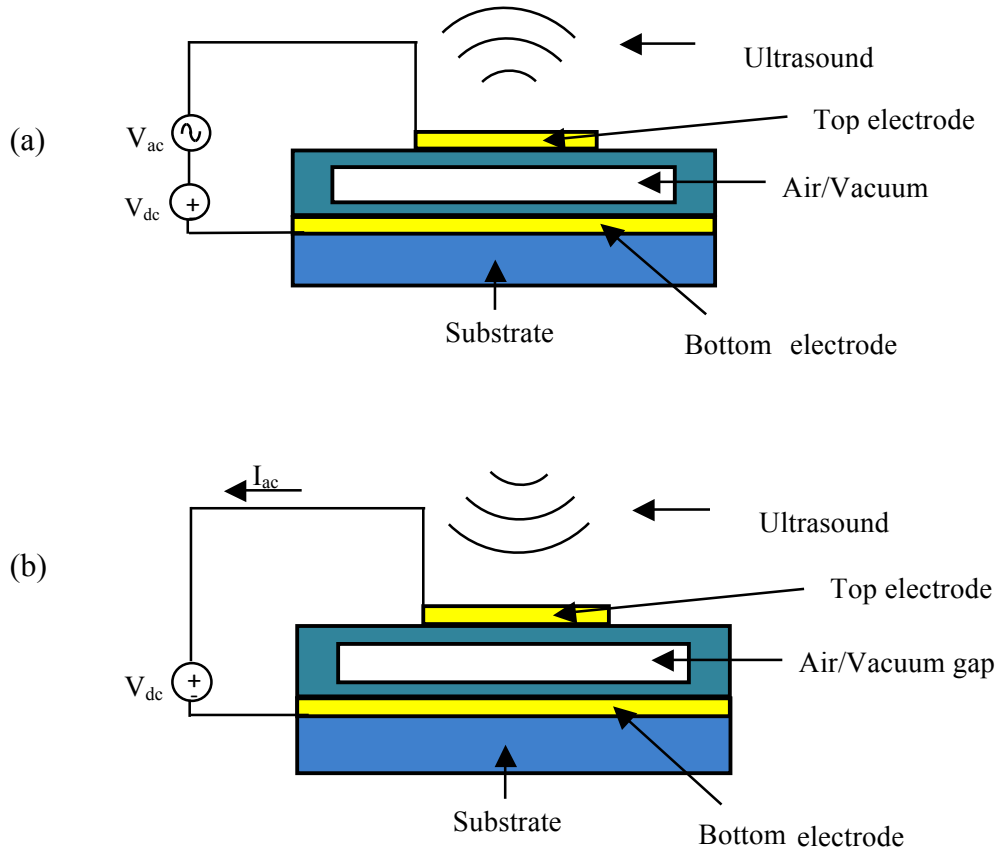


Figure 2. Principle of operation of a CMUT cell in (a) transmission mode and (b) receiving mode

CMUT *element* is formed by fabricating hundreds or thousands of CMUT *cells* on the same die. In a CMUT element, the cells are usually excited in phase to ensure adequate acoustic power transmission for different applications of interest. A transducer consists of tens or hundreds of CMUT *elements*. A transducer array typically contains about 64 or 128 elements.

2.2 Analytical Modeling of CMUT

To be able to characterize the behavior of a CMUT, it is important to model the device analytically. Analytical modeling would offer an insight into the operation of this MEMS device as well as providing results for preliminary analysis. Due to complexity of analytical modeling of

CMUT, reduced order models are presented. To highlight the most important aspects of CMUT behavior, several approximations were assumed to simplify the model to the first order analysis. Furthermore, electrical fringing fields at the edge of the membrane are ignored, and all the contacts and conductors are assumed to be perfect. It is also assumed that the relation between the restoring force and displacement is linear, and the CMUT is operating in vacuum with no loading on the membrane. Operation of a CMUT in a vacuum means there is no load on the membrane and the acoustic damping is not fully taken into consideration. These are the conditions for the work in this chapter for simplicity. A more advanced representation of the following model is introduced in Chapter 3. The membrane is designed to be circular due to the fact that the stress of a circular membrane around its edge is least compared to all other membrane shapes[25]. Note that throughout all the analyses from hereafter the top membrane acts both as the membrane and the top electrode, and the substrate acts as the bottom electrode. Ladabaum et al. [26] introduced the early version of analytical model of a CMUT. They performed an analysis on a lumped electromechanical modeling, which consist of a mass, a linear spring and a parallel plate capacitor. A system of such is shown in figure 3.

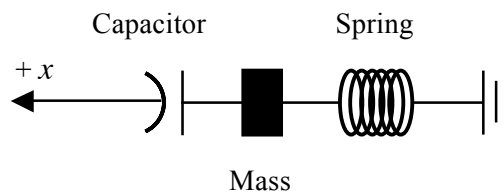


Figure 3. First order lumped electromechanical model of a CMUT

Note that Figure 3 only models the electro-mechanical properties of the CMUT. An improved version of this model is shown in Figure 23 in Chapter 3, where the acoustical property of CMUT (i.e. acoustic damping) is taken into consideration. In this model, the capacitor represents

the capacitance of the CMUT, the mass denotes the mass of the membrane and the mechanical spring models the elasticity of the membrane. The damping term in the complete model comes from the energy transfer from the electrical domain to the acoustical domain. More specifically, the major damping system comes from and represents the acoustic impedance of the medium into which ultrasound is to be transmitted.

The force of spring and capacitor cause the mass to actuate.

$$F_{capacitor} + F_{spring} = F_{mass} \quad \text{Eqn. 1}$$

$F_{capacitor}$ is the generated electrostatic force when a voltage is applied across the electrodes. The electrostatic force could be found by differentiating the potential energy of the capacitor with respect to the mass position.

$$F_{capacitor} = \frac{-d}{dx} \left(\frac{1}{2} CV^2 \right) = -\frac{1}{2} V^2 \left[\frac{d}{dx} \left(\frac{\epsilon_0 A}{d_0 - x} \right) \right] = \frac{\epsilon_0 AV^2}{2(d_0 - x)^2} \quad \text{Eqn. 2}$$

In equation 2, V is the applied voltage across the capacitor, A is the surface area of the capacitor, C is the capacitance, ϵ_0 is the permittivity of free space, d_0 is the effective gap distance between top and bottom electrode and x is the displacement of the capacitor plates in positive direction from equilibrium as shown in figure 3. The displacement is assumed to be uniform over the whole membrane and is the displacement of the centre of the membrane. The spring force, F_{spring} , which is the restoring force of the membrane, is linearly proportional to displacement, x .

$$F_{spring} = -kx \quad \text{Eqn. 3}$$

where k is the spring constant of the capacitance membrane.

The mass force, F_{mass} , is the resultant force of spring and capacitor, and follows Newton's second law of motion.

$$F_{mass} = m \frac{d^2x(t)}{dt^2} \quad \text{Eqn. 4}$$

Substituting the three force terms, equation 1 gives a time dependant equation.

$$m \frac{d^2x(t)}{dt^2} - \frac{\epsilon_0 AV(t)^2}{2[d_0 - x(t)]^2} + kx(t) = 0 \quad \text{Eqn. 5}$$

To avoid any short-circuit when the top membrane collapses, the substrate is usually coated with an insulation layer. Silicon nitride is a commonly used material as an insulator in MEMS fabrication processes. Thus, the separation of the capacitor plates, d_0 , changes to an effective gap distance as following:

$$d_0 = d_g + \frac{d_{ins}}{\epsilon_{ins}} \quad \text{Eqn. 6}$$

In equation 6, d_g is the air/vacuum gap distance, d_{ins} is the thickness of the insulation layer and ϵ_{ins} is the relative dielectric permittivity of the insulation dielectric. Note that we will neglect the effect of such insulation layer because conceptually it is more explicable to assume d_{ins} and ϵ_{ins} can be neglected until collapse[26]. The reason can be explained if one considers equation 6 once more. Since the air/vacuum gap distance is generally much larger than insulation layer, the second term (i.e. $\frac{d_{ins}}{\epsilon_{ins}}$) can be neglected.

2.2.1 Collapse Voltage Calculation

Equation 5 describes the behavior of the system and is a time dependant nonlinear second order differential equation. To decrease its complexity and to extract the significant terms of the system, one can consider the case where $V(t) = V_{DC}$. In that case the harmonic terms are eliminated and we obtain:

$$\frac{\epsilon_0 A V_{DC}^2}{2(d_0 - x)^2} = kx \quad \text{Eqn. 7}$$

Note that as DC bias voltage is increased, the gap distance becomes smaller; therefore, the spring force increases. Figure 4 shows the electrostatic and spring forces as a function of normalized gap distance for a bias voltage smaller than collapse voltage. When the membrane is at equilibrium, the magnitude of electrostatic force and spring force are equal. At any voltages bellow collapse, there are two physical solutions to the displacement where the spring and electrostatic forces are equal. At one of these equilibrium points, namely point B, when the equilibrium is disturbed to further increase the displacement, the electrostatic for becomes larger than spring force. Thus, the equilibrium is lost to further increase the displacement. Although point B is a mathematical solution, physically it is an unstable equilibrium. On the other hand, at point A, when the equilibrium is disturbed towards increasing the displacement, the spring force becomes greater than the electrostatic force. Hence the displacement is pushed back to its equilibrium point. Consequently, point A is a stable equilibrium point.

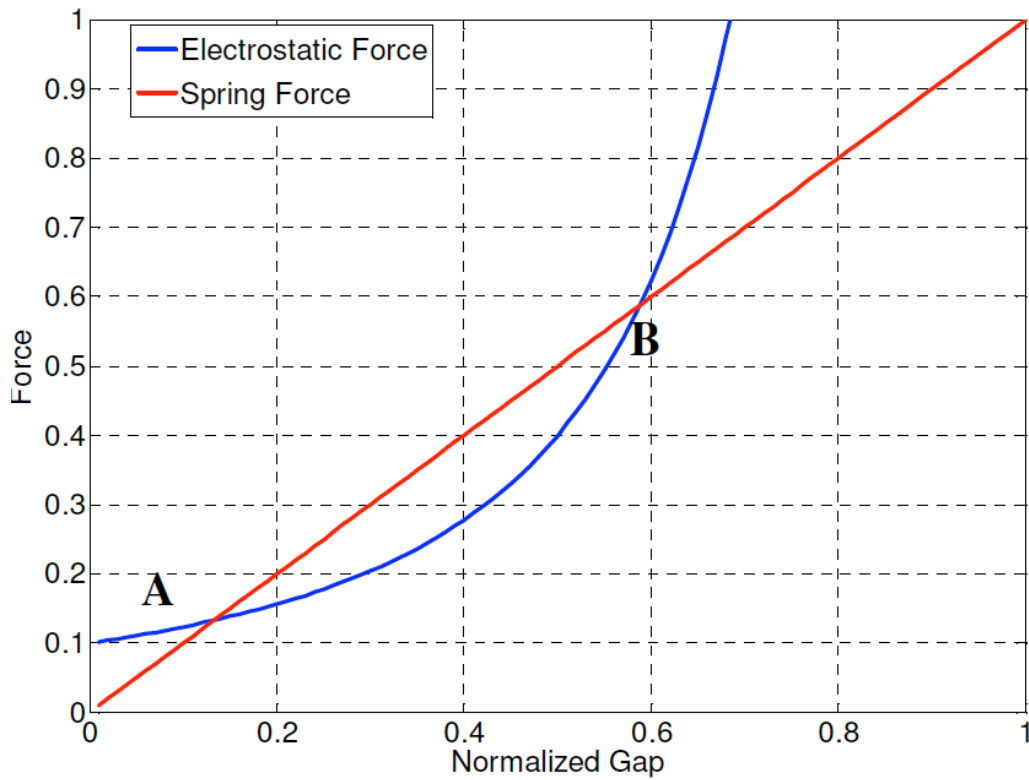


Figure 4. Electrostatic and spring forces as a function of gap distance in analytical modeling of CMUT when $V_{DC} < V_{collapse}$ [27]

When the DC voltage is increased, the electrostatic force increases with a square dependency on voltage. However, the spring force does not increase with bias voltage since the force is only dependent on displacement. Hence, when the voltage reaches a certain value, the equilibrium points reduces to one as shown in figure 5. At this point electrostatic force overwhelms the spring force and the membrane collapses. The voltage at which this phenomenon occurs is called *collapse* or *pull-in* voltage.

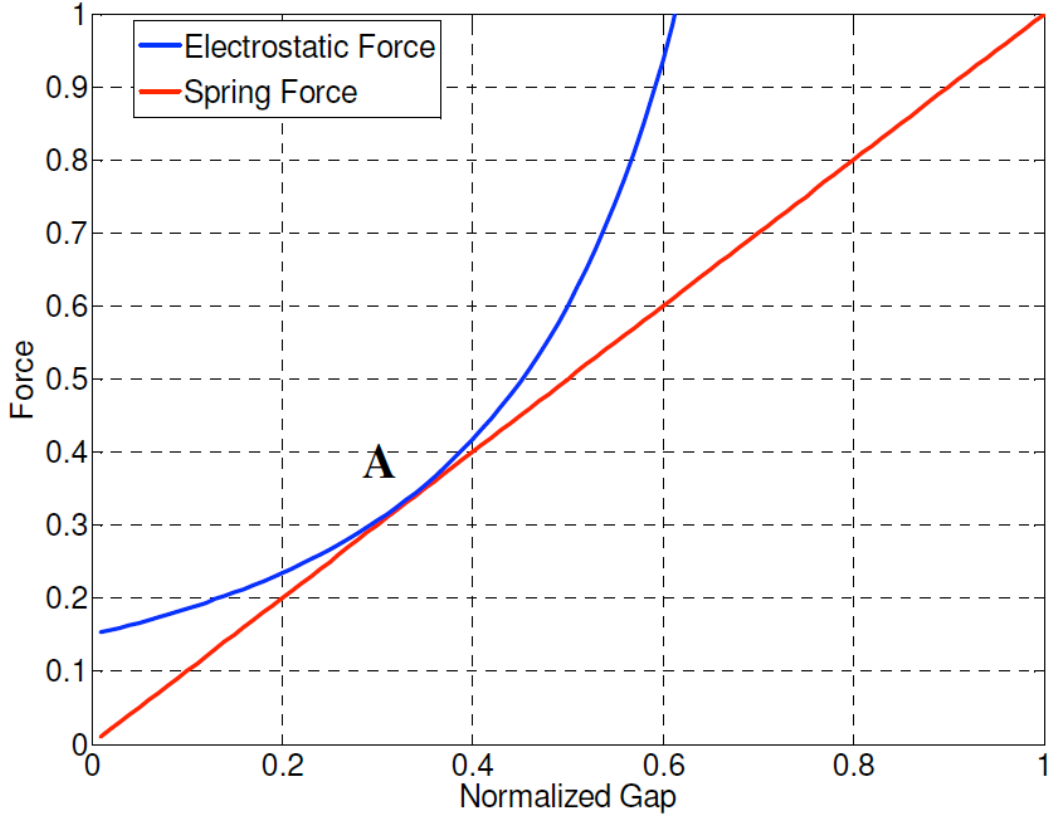


Figure 5. Electrostatic and spring forces as a function of gap distance in analytical modeling of CMUT when $V_{DC}=V_{collapse}$ [27]

The pull-in voltage can also be found analytically by rearranging equation 7 to obtain a third degree linear polynomial in x . Solving the polynomial and considering the one physically meaningful solution, the pull-in voltage is found.

$$V_{collapse} = \sqrt{\frac{8kd_0^3}{27\epsilon_0 A}} \quad \text{Eqn. 8}$$

The displacement of the membrane when pull-in occurs is only a third of the air/vacuum gap. This relation can be calculated parametrically by substituting equation 8 in equation 7.

$$d_{collapse} = \frac{2}{3}d_0 \quad \text{Eqn. 9}$$

In reality, the displacement of a CMUT membrane at pull-in is greater than a third of the gap distance since the movement of the CMUT is not perfectly piston-like. This fact will be more explored in the next chapter.

In order to perform any further analytical results, the first step is to extract geometrical dimensions of the CMUT; that includes finding the gap distance, membrane thickness and radius to comply with the requirements mentioned in previous chapter. Since CMUT would be fabricated using PolyMUMPs technology, there were only four possible designs[28]. The possible CMUT configurations in PolyMUMPs process are listed in table 1.

Designs	Membrane thickness	Structural Material	Gap distance	Sacrificial Material
Design 1	2.0 μm	Poly 1	2.00 μm	Oxide 1
Design 2	3.5 μm	Poly 1+ Poly 2	2.00 μm	Oxide 1
Design 3	1.5 μm	Poly 2	0.75 μm	Oxide 2
Design 4	1.5 μm	Poly 2	2.75 μm	Oxide 1+ Oxide 2

Table 1. Combination of layers in PolyMUMPs to fabricate CMUT

Referring to previous chapter, one of the important requirements is to keep pull-in voltage as low as possible. Note that in equation 8, the pull-in voltage has a direct relationship with the gap distance. Therefore, to have a low pull-in voltage, the gap distance requires being small. Creating the gap distance requires using a sacrificial layer, which is silicon dioxide in the case of PolyMUMPs technology. Hence, the smallest sacrificial layer was chosen to form the gap distance (i.e. Oxide 2). Complete fabrication process of CMUTs in PolyMUMPs is described chapter 4. It is important to note that variation in gap distance would not have a crucial effect on other requirements including the resonant frequency.

Using Oxide 2 as the sacrificial layer would limit us to only use Poly2 layer as the membrane of the CMUT (i.e. Design 3). As a result, the membrane thickness and gap distance would be $1.5\mu\text{m}$ and $0.75\mu\text{m}$, respectively. According to this result, the only parameters that can be varied so that we obtain the required constraints are the spring constant, k , and the surface area of membrane, A .

The CMUT membrane resembles a circular membrane under a distributed load and its spring constant is [29]:

$$k = \frac{16\pi E d_m^3}{3R^2(1 - \nu^2)} \quad \text{Eqn. 10}$$

E is the Young's modulus of the membrane and it is 160 GPa for poly-Silicon. d_m is the membrane thickness, R is the membrane radius and ν is the dimensionless Poisson's ratio - $\nu=0.23$ for poly-Silicon - .

On the other hand, the area of the circular membrane CMUT is defined as:

$$A = \pi R^2 \quad \text{Eqn. 11}$$

Note that in both equation 10 and 11, the only parameters over which we have control are the radius, R , since the Young's modulus and Poisson's ratio are the intrinsic properties of the materials.

Substituting equation 10 and 11 in equation 8, and replacing the geometrical values obtained from fabrication technology, a relation between the pull-in voltage and the CMUT membrane radius can be obtained. Such relation is shown in equation 12 and plotted in figure 6.

$$V_{collapse} = \sqrt{\frac{128}{81} \frac{E d_m^3 d_0^3}{\epsilon_0 (1 - \nu^2)} \frac{1}{R^4}} \quad \text{Eqn. 12}$$

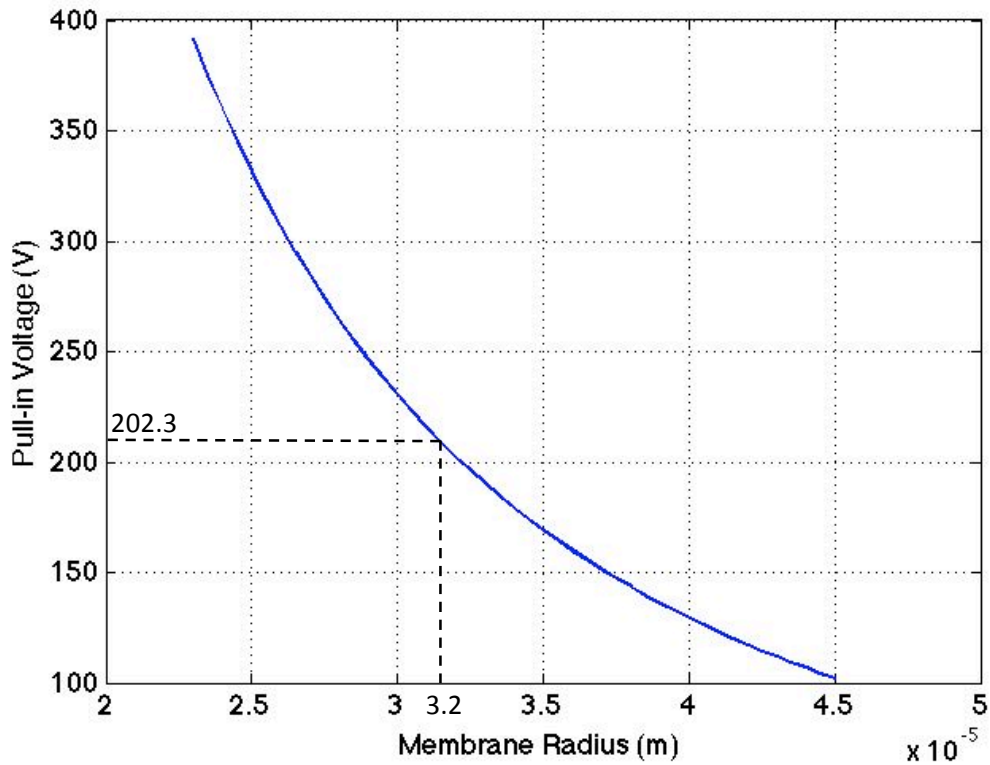


Figure 6. The relationship between pull-in voltage and the radius of the CMUT membrane

Note that the pull-in voltage is inversely proportional and sensitive to the square of the membrane radius. For further studies in pull-in phenomenon of general MEMS devices refer to [30] by Cretu et al.

2.2.2 Resonant Frequency Calculation

The other important requirement of the CMUT that is to be considered is the resonant frequency. As discussed before, the target application of CMUT in this work is the detection of breast tumors using ultrasound machine. Therefore, the frequency of the ultrasound machine probe is required to be within the range of 5 MHz to 9 MHz. This range of frequency comes from considering penetration depth, size of the tumors and attenuation of ultrasound signals at these

frequencies. If we assume that the average penetration depth is about 10cm and the speed of sound in a fatty tissue (i.e. breast) is about 1540 m/s, the wavelength of an ultrasound wave with a frequency of 5MHz is about $\lambda=0.308\text{mm}$ (i.e. $\lambda = c/f$). This is a desired wavelength since resolution is typically a few wavelength, so is sufficient for depicting tumors typically a few cm in size. Furthermore, this frequency is suitable for breast tumor detection in terms of tissue attenuation. According to ultrasound attenuation equation (i.e. $Attenuation[dB] = \alpha[dB/(MHz \times cm)]L[cm].f[MHz]$), the higher the frequency the more attenuation is obtained. Taking an average attenuation of 0.5dB/cm for each MHz frequency, the ultrasound wave at 5MHz is attenuated about 25dB to reach a tumor located 10cm deep in a fatty tissue. This attenuation is adequately low to enable detecting the ultrasound pressure waves reflected from the tumor. Higher frequencies increase the attenuation and hence the detection of the echo would be very difficult if not impossible. Lower frequencies would decrease the performance of the image forming as well as not being suitable for desired tumor sizes. Keeping this frequency range in mind, one can optimize the geometry of the CMUT. The fundamental frequency, which is the desired resonant frequency, is found by:

$$f_0 = \frac{1}{2\pi} \sqrt{\frac{k}{M_0}} \quad \text{Eqn. 13}$$

In equation 13, f_0 , is the resonant frequency, M_0 is the effective mass and k is the spring constant of the CMUT membrane as described in equation 10. The effective mass of the membrane with clamped edges is also calculated.

$$M_0 = \rho_m d_m A \left(\frac{2\sqrt{2}}{(\lambda_a)_{mn}} \right)^4 \quad \text{Eqn. 14}$$

where ρ_m is the density of the membrane and $(\lambda_a)_{mn}$ is a constant corresponding to the mode shapes of the membrane. The number of concentric circles on the membrane is denoted by m and the number of diametral lines is denoted by n . For a membrane vibrating at its fundamental frequency (i.e. $m=0$ and $n=0$), this constant is $(\lambda_a)_{00} = 3.196$ [31]. Note that this factor accounts for the fact that the CMUT membrane moves in a bowl-like shape rather than piston-like way, with the centre of membrane deflecting more than the outer radius. Substituting spring constant from equation 10 and effective mass from equation 14 into equation 13, one can find the following resonant frequency relation.

$$f_0 = \frac{1}{R^2} \frac{(\lambda_a)_{00}^2}{2\pi} \sqrt{\frac{Ed_m^2}{12(1-\nu^2)\rho_m}} \quad \text{Eqn. 15}$$

One can observe from equation 14 the relation between the radius of the membrane and its resonant frequency. Other parameters are either the intrinsic properties of the membrane material or constants that cannot be modified. Note that the resonant frequency of a CMUT is not dependant on the gap distance, as mentioned earlier. Figure 7 illustrates the resonant frequency as a function of membrane radius in a CMUT cell. The values of important parameters are also listed in table 2.

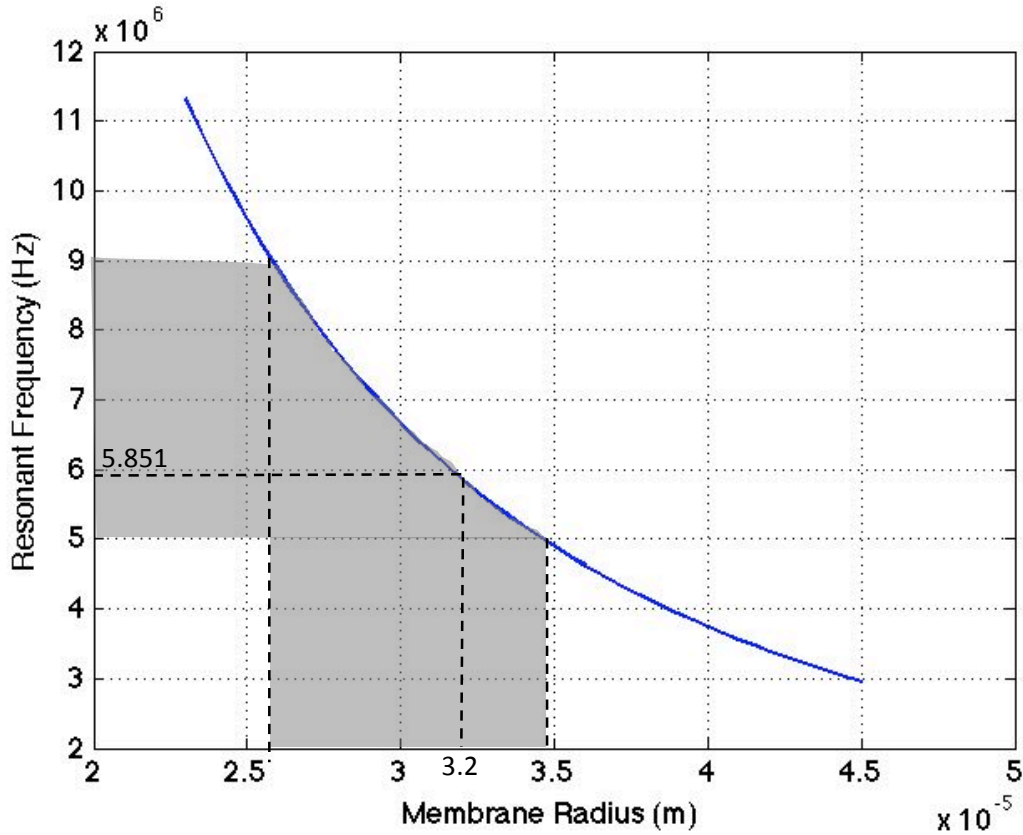


Figure 7. Relationship between the resonant frequency and the radius of the CMUT membrane

Symbol	Value	Unit	Parameter
E	160	GPa	Young's modulus of the membrane material
ν	0.23	-----	Poisson's ratio of membrane material
$(\lambda_a)_{00}$	3.196	-----	Mode shape constant at fundamental frequency
ρ_m	2332	kg/m ³	Density of membrane material
ϵ_0	8.854×10^{-12}	F/m	Permittivity of free space
d_m	1.5	μm	Membrane thickness
d_0	0.75	μm	Air/Vacuum gap distance

Table 2. List of important parameter values

In figure 7, the shaded area is the region of interest (ROI) that meets the frequency requirement. We need to determine a membrane radius, which falls in the required frequency region while lowering the pull-in voltage. To achieve so, one can find a relation between resonant frequency and pull-in voltage. Since both the collapse voltage and resonant frequency are functions of membrane radius, R , one can rearrange equation 12 and 13 for R and equate the two to obtain the following relation.

$$V_{collapse} = 2\pi f_0 \sqrt{\frac{512}{27} \frac{\rho_m d_m d_0^3}{\epsilon_0 (\lambda_a)_{00}^4}} \quad \text{Eqn. 16}$$

It is observed that the relation between pull-in voltage and resonant frequency is linear. This means, the more the resonant frequency is increased, the higher the pull-in voltage will be. In order to keep the pull-in voltage as low as possible, we chose the resonant frequency to be close to its lower boundary region and acquire the radius of the membrane. A resonant frequency about 6 MHz would be adequately high and reasonable. Note that the boundary value of frequency was not chosen (i.e. 5 MHz). The reason is that the analytical frequency analysis is only an approximation and does not fully characterize the damping of the CMUT. The damping would decrease the resonant frequency by an amount. Putting all together, we obtain a radius of about **$R=32 \mu\text{m}$** that corresponds to a resonant frequency of **$f_0=5.851 \text{ MHz}$** .

To observe the analytical pull-in voltage one can refer to figure 6, find the 32-micron radius on x-axis and trace it back to the corresponding collapse voltage. The analytical pull-in voltage in that case would be **$V_{collapse}= 202.3 \text{ V}$** . Another approach would be to plot equation 16 (i.e. $V_{collapse}$ and f_0 relation) and find the pull-in voltage, as shown in figure 8.

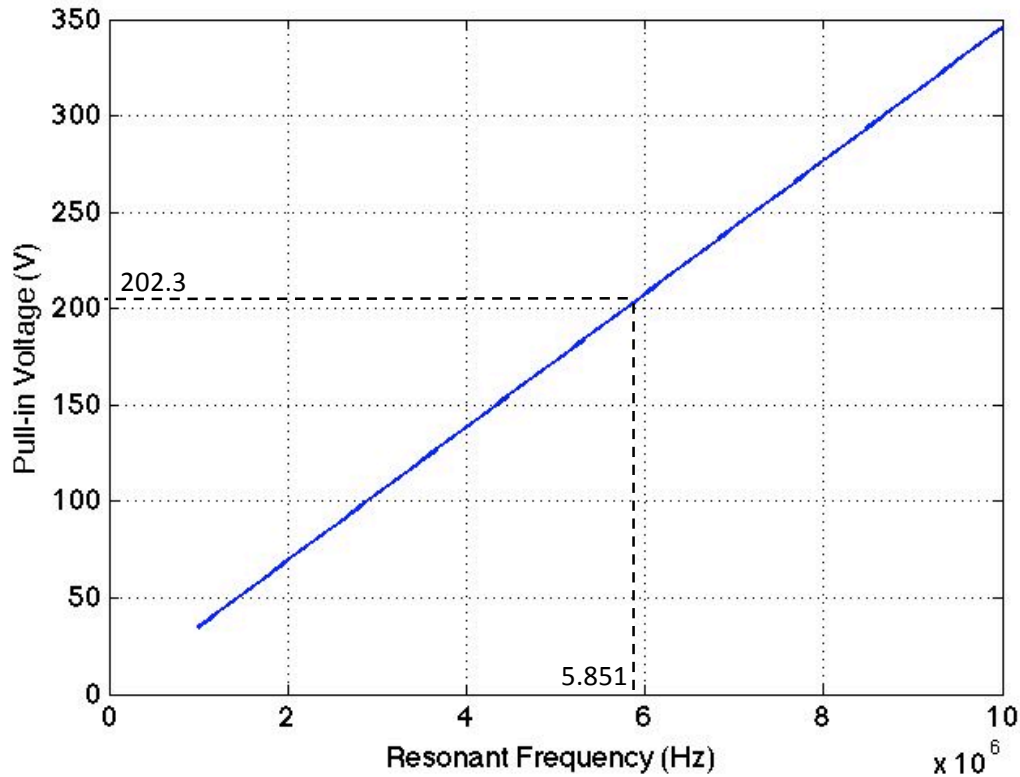


Figure 8. Analytical pull-in voltage versus resonant frequency of the CMUT membrane

The extracted values later are used for finite element and behavioral modeling of CMUT in the next chapter.

2.2.3 Spring Softening Coefficient

Due to non-linearity of the system, besides collapse voltage phenomenon, electrostatic spring softening also occurs, which is more evident, experimentally. Note that the spring constant mentioned in equation 10 is simply valid and accurate for an unbiased membrane. In reality, the apparent spring constant changes as the voltage varies. The reason is that as the membrane displaces, a spring force is generated in opposite direction; however, the displacement under a constant DC voltage causes an increase in electrostatic force in the same direction as the

displacement. This increase in electrostatic force is interpreted as spring softening. To develop a mathematical expression for electromechanical behavior of CMUT membrane, one can linearize equation 5 by using Taylor expansion about the point $x(t)=0$ and obtain:

$$m \frac{d^2 x(t)}{dt^2} - \left[\frac{\epsilon_0 A V_{DC}^2}{2d_0^2} + \frac{\epsilon_0 A V_{DC}^2}{d_0^3} x(t) \right] + kx(t) = 0 \quad \text{Eqn. 17}$$

Collecting like terms in the equation yields a recognizable equation:

$$m \frac{d^2 x(t)}{dt^2} + \underbrace{\left(k - \frac{\epsilon_0 A V_{DC}^2}{d_0^3} \right)}_{k_{soft}} x(t) = \frac{\epsilon_0 A V_{DC}^2}{2d_0^2} \quad \text{Eqn. 18}$$

Thus, the softened spring constant is given by:

$$k_{soft} = k - \frac{\epsilon_0 A V_{DC}^2}{d_0^3} \quad \text{Eqn. 19}$$

To be more realistic, one can linearize equation 5 using Taylor series expansion about the point $x(t) = \frac{2}{3}d_0$ rather than $x(t) = 0$. The reason is because the CMUT will operate close to collapse voltage and the displacement about the collapse voltage is two third of the initial gap distance.

Hence we obtain:

$$m \frac{d^2 x(t)}{dt^2} - \left[\frac{\epsilon_0 A V_{DC}^2}{3} d_0 - \frac{18\epsilon_0 A V_{DC}^2}{d_0^2} + \frac{27\epsilon_0 A V_{DC}^2}{d_0^3} x(t) \right] + kx(t) = 0 \quad \text{Eqn. 17 (b)}$$

collecting like terms would yield:

$$m \frac{d^2 x(t)}{dt^2} + \underbrace{\left(k - \frac{27\epsilon_0 A V_{DC}^2}{d_0^3} \right)}_{k_{soft}} x(t) = \frac{\epsilon_0 A V_{DC}^2}{3} d_0 - \frac{18\epsilon_0 A V_{DC}^2}{d_0^2} \quad \text{Eqn. 18 (b)}$$

and the spring constant is:

$$k_{soft} = k - \frac{27\epsilon_0 AV_{DC}^2}{d_0^3}$$

Other analytical approaches have been taken to compute the softened spring[26],[32]. Spring softening effect, decreases the resonant frequency of the CMUT, as the DC bias voltage is increased. The frequency shift can be calculated by using k_{soft} for spring constant in equation 13. Resonant frequency and spring constant variation versus increasing V_{DC} are shown in figure 9.

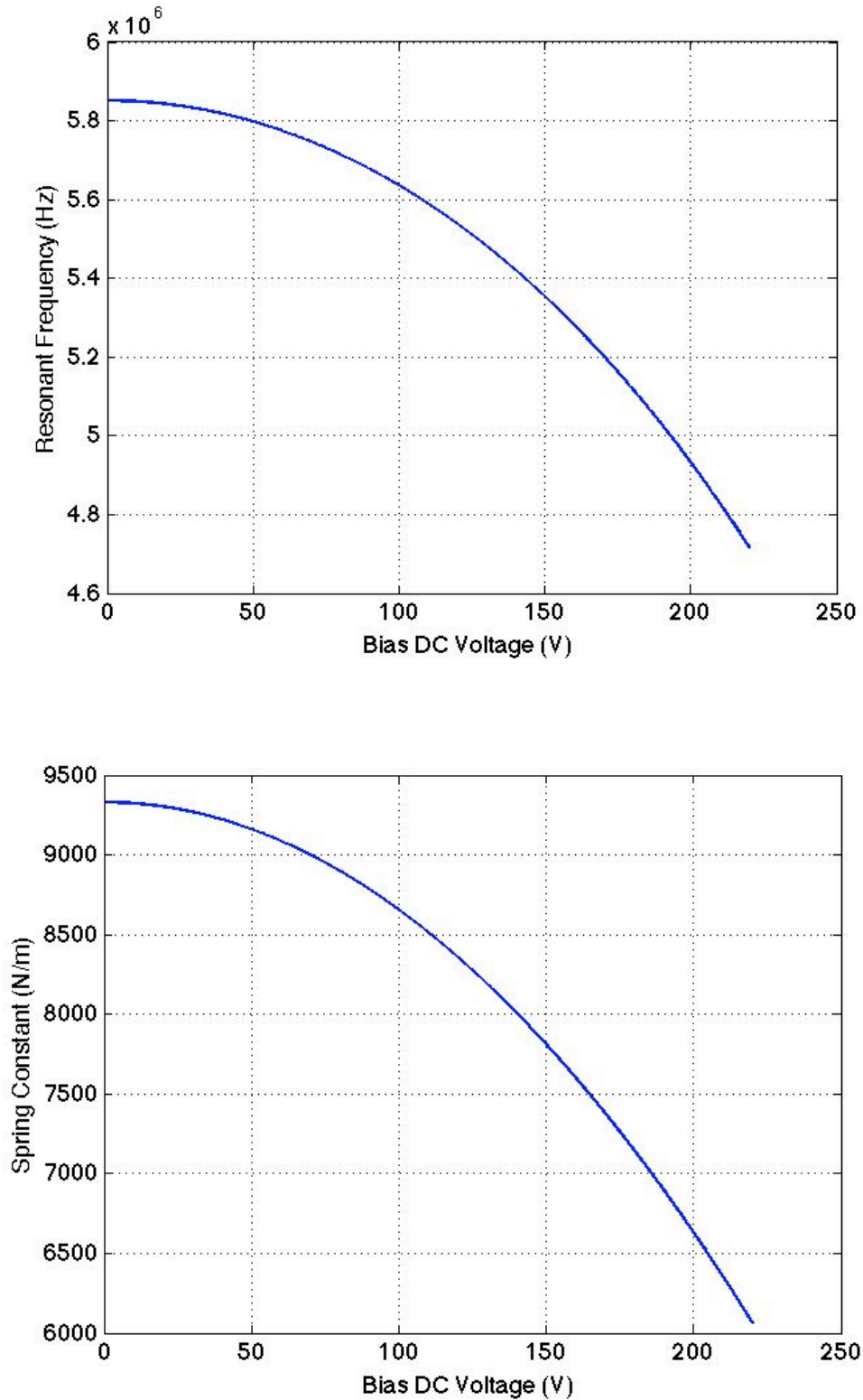


Figure 9. The effect of spring softening when increasing bias DC voltage on (a) resonant frequency and (b) apparent spring constant

One would observe the spring constant decreases as the DC voltage increases from the figure. If the CMUT is biased to 80% of the collapse voltage, the frequency shifts by **583kHz** and the resonant frequency drops to **5.268 MHz**. It is worth noting that the spring softening effect would be greater in reality due to the fact that the gap distance, d_0 , would change under different bias voltages. A more accurate spring softening value is calculated numerically while performing finite element analysis in chapter 3.

2.2.4 Electromechanical Coupling Effect

A transducer is a device, which converts a form of energy to another. In CMUTs the energy conversion is from electrical to mechanical and vice-versa. Hence another important parameter of CMUT to consider is its electromechanical coupling coefficient. This coefficient determines the energy conversion efficiency of electrical to mechanical domains. Basically, the electromechanical coupling coefficient, k_T^2 , is the ratio of mechanical energy of the CMUT to the total energy stored in the MEMS structure.

$$k_T^2 = \frac{E_{mech}}{E_{total}} = \frac{1}{1 + \frac{E_{elec}}{E_{mech}}} \quad \text{Eqn. 20}$$

where $E_{total} = E_{mech} + E_{elec}$. For a parallel plate capacitor finding this coefficient is rather simple.

Hunt used the parallel plate capacitor to model a condenser microphone [2].

$$k_T^2 = \frac{2x}{d_0 - x} \quad \text{Eqn. 21}$$

The model assumes a rigid piston-like movement with electric potential applied to the top electrode and grounding the bottom electrode. With no DC bias voltage applied, the

displacement is zero and hence the efficiency is zero. As the displacement increases with increasing voltage, the efficiency increases, too. At a displacement equal to one-third of the gap, when the membrane collapses, the efficiency is equal to 1. k_T^2 was calculated by Fraser et al. [33] for a CMUT membrane that uses fixed, C^S , and free, C^T , capacitances of the transducer. Instead of using displacement, the derivation uses voltage and charge. The fixed capacitance is the capacitance of the CMUT at a given DC voltage and the free capacitance is the derivative of the charge with respect to DC voltage (i.e. the slope of the charge-voltage relation). The equations of fixed and free capacitance are given bellow, respectively.

$$C^S = \frac{Q(x)}{V} \Big|_{x_{DC}, V_{DC}} = C(x) \Big|_{x_{DC}, V_{DC}}, \quad \text{Eqn. 22}$$

$$C^T = \frac{dQ(x)}{dV} \Big|_{x_{DC}, V_{DC}} = \frac{d}{dV} (VC^S) \Big|_{x_{DC}, V_{DC}} \quad \text{Eqn. 23}$$

The approach used to find the coupling coefficient of CMUT is calculated as following [32],[16],[34]:

$$k_T^2 = 1 - \frac{C^S}{C^T} \quad \text{Eqn. 24}$$

The coupling coefficient describes the electromechanical efficiency of our MEMS device and thus is important to consider. This coupling coefficient is in agreement with Hunt's[2] approach for parallel plate capacitor. Detailed derivations of the coupling coefficient are not fully presented in this work. For detailed derivations please refer to [32], [34], [16] or [2]. To further analyze the efficiency, one can look into both AC and DC components of the applied voltage. Knowing that the combination of AC and DC components of the applied voltage is smaller or equal to pull-in voltage (i.e. $V_{AC} + V_{DC} = V_{PI}$), there is a point where this combination of DC and

AC voltages lead to maximum kinetic energy, W_{kin} . This maximum kinetic energy is in fact the optimum acoustic energy from the CMUT membrane and more importantly the maximum efficiency. Figure 10 illustrates the variation of kinetic energy of the CMUT as a function of AC voltage component. k_T^2 would be revisited in FEM section (i.e. Chapter 4) to obtain more accurate numerical results.

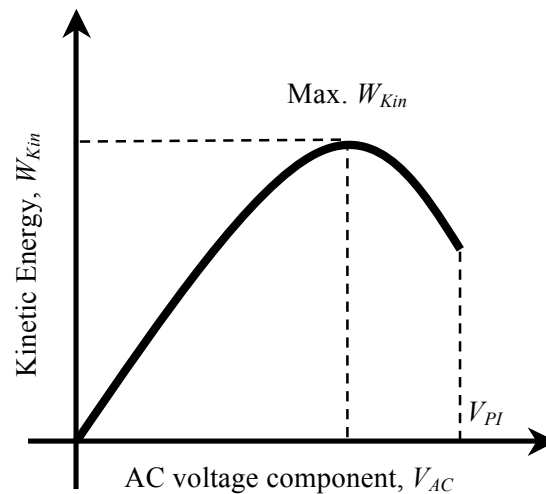


Figure 10. Variation of kinetic energy with respect to applied harmonic voltage component

2.3 Electromechanical Equivalent Circuit of CMUT

CMUT, similar to piezoelectric transducer, is an energy converter between electrical and mechanical domains. When operating as a transmitter, the CMUT converts the applied AC electrical energy to mechanical vibration. As a receiver, the acoustic pressure causes a mechanical vibration and is converted to electrical energy. One can use a two-port network to model a moveable plate capacitor and find a relationship between electrical parameters, voltage

and current, and mechanical parameters, force and velocity. Such two-port model is shown in figure 11.

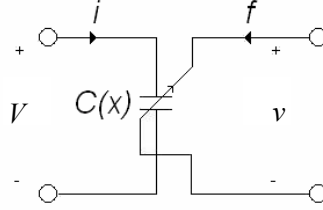


Figure 11. Two-port schematic of a moveable plate capacitor[15]

In this representation, the current in electrical domain corresponds to force in mechanical domain while the voltage in electrical domain corresponds to velocity in mechanical domain. Recall that the variable capacitance, $C(x)$, is given by:

$$C(x) = \frac{\epsilon_0 A}{(d_0 - x)} \quad \text{Eqn. 25}$$

Assuming that the harmonic part of the voltage is much smaller than the DC part (i.e. $V_{ac} \ll V_{DC}$) the current through the device is:

$$I = \frac{d}{dt} Q = \frac{d}{dt} (C(t)V(t)) = C(t) \frac{d}{dt} V(t) + V(t) \frac{d}{dt} C(t) \quad \text{Eqn. 26}$$

Substituting the variable capacitance equation we obtain the first relation equation between electrical and mechanical domain:

$$I = C(x) \frac{d}{dt} V + \frac{\epsilon_0 A}{(d_0 - x)^2} v V \quad \text{Eqn. 27}$$

In the equation, v is the velocity of the displacement (i.e. $v = \partial x / \partial t$).

Using conservation of energy, the second relationship is obtained.

$$F = \frac{\epsilon_0 A}{2(d_0 - x)^2} V^2 \quad \text{Eqn. 28}$$

Equation 28 is a simplified version of equation 2, which describes the electrostatic force on the membrane by applying voltage to the parallel plate capacitor. Equations 26 and 28 along with mechanical parameters of equations 10 (i.e. spring constant equation) and equation 14 (i.e. effective mass equation), result in an electromechanical equivalent circuit of CMUT, which is shown in figure 12.

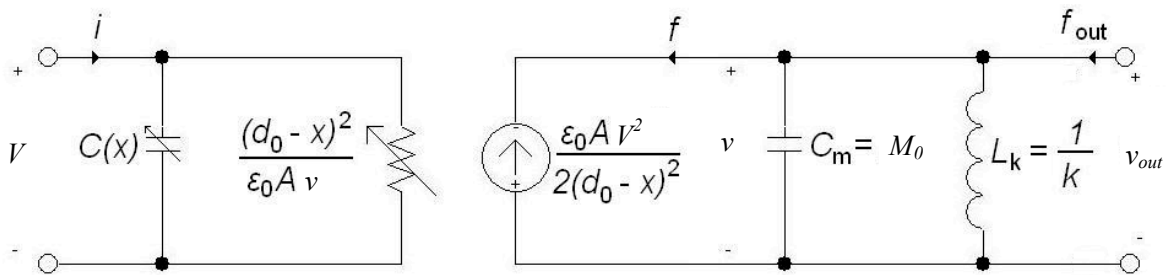


Figure 12. Full electromechanical equivalent circuit of CMUT [15]

In the circuit, C_m and L_k are electrical equivalents of the mechanical parameters of effective mass, M_0 , and spring constant, k , respectively. Note that the implemented model by Frew et al. [15] avoids small-signal linearization of electromechanical relations about a DC point. Similar “linearized” models have been previously implemented[26],[16],[35][36],[37] base on Mason’s work[38]. In linearized models, a fixed capacitor represents the capacitance of the parallel electrodes of the CMUT, an ideal transformer performs the conversion of energy from the electrical to the mechanical domain, and a complex impedance models the mechanical impedance of the membrane. The circuit shown in figure 12 is also used in behavioral modeling of the CMUT in the next chapter. One can observe the equivalent circuit as a transformation from electrical to mechanical domain where the transformer ratio can be calculated from

equation 27 and is:

$$n = \frac{\epsilon_0 A}{(d_0 - x)^2} V \quad \text{Eqn. 29}$$

Note that the transformer ratio is directly proportional to the applied voltage and inversely proportional to the square of the effective gap. This means, the higher the bias voltage or the smaller the effective gap, the larger the transformer ratio and hence a better electromechanical energy transformation. It is also interesting to observe that the CMUT would operate up until it reaches collapse voltage. Equation 16 states that the collapse voltage is proportional to the gap distance (i.e. $V_{collapse} \propto d_0^{3/2}$). On the other hand, equation 29 gives another relation between transformer ratio and gap distance (i.e. $n \propto d_0^{-2}$). Now taking these two relations and putting them into equation 29, we obtain a relationship between transformer ratio and the gap distance:

$$n \propto \frac{1}{\sqrt{d_0}} \quad \text{Eqn. 30}$$

It is interesting to note that at collapse voltage, maximum transformer ratio is achieved and is inversely proportional to the square root of the initial gap distance. Hence, the smaller the initial gap distance, the higher the transformation. This is a confirmation on choosing the smallest sacrificial layer in PolyMUMPs process to be used to form the gap distance.

In summary, to meet all the requirements, the values in table 3 were analytically considered and calculated.

Symbol	Value	Unit	Parameter
R	32	μm	Radius of the membrane
d_m	1.5	μm	Membrane thickness
d_0	0.75	μm	Air/Vacuum gap distance
d_{ins}	0.60	μm	Insulation thickness
f_0	5.851	MHz	Undamped resonant frequency
f_{0_damped}	5.268	MHz	Damped resonant frequency
$V_{collapse}$	202.3	V	Collapse Voltage

Table 3. List of important parameters to design the CMUT calculated analytically

Note that f_{0_damped} is the damped resonant frequency due to spring softening when the CMUT is biased at 80% of the pull-in voltage.

Chapter 3

Simulation

Although analytical computation provides a quick and simple analysis on CMUT characteristics, it is just an approximation and is based on assumptions, which are not entirely correct for a CMUT device. An example is ignoring the bowl-shape movement of the diaphragm and assuming the membrane moves like a rigid piston. Hence, the analytical modeling lacks accuracy and precision and ignores the non-linear property of the CMUT. On the other hand, to discover the reliability and validity, the analytical modeling of CMUT was compared with other accurate analyses similar to finite element. This would ensure that the analytical model could be used in future for quick analysis and optimization of CMUT parameters.

This chapter focuses on finite element analysis (FEA) and behavioral modeling of CMUT to fully characterize the device. The results of the two analyses are extracted and then are compared to the analytical modeling results from chapter 2. It would present a profound insight on CMUT behavior.

3.1 Finite Element Simulation of CMUT

Finite element analysis is proving to be a nearly indispensable tool in all MEMS development including CMUT design and analysis. This tool is especially useful in non-linear MEMS structures. Non-linear properties of MEMS devices make the analytical modeling cumbersome if

not impossible. Therefore, FEA method is used to analyze various performance parameters of CMUT such as resonant frequency, collapse voltage, coupling coefficient and electrostatic spring softening.

Finite element modeling of CMUT has been previously reported using ANSYS (ANSYS Inc., Canonsburg, PA), a commercially available software. Characterization of different aspects of CMUT such as static and quasi-static analysis[39-42], harmonic analysis[43], predicting output pressure[44], membranes cross-talk[45] and time-domain non-linear behavior of CMUTs[46],[47] have been performed using this FEA tool. Another commercially available software, COMSOL Multiphysics® (COMSOL Inc., Burlington, MA, USA), was used to perform FEA of CMUT in this report. COMSOL Multiphysics® has the advantage of having an intuitive graphical user interface as well as being capable of coupling unlimited physics for a MEMS structure. The following sections describe CMUT cell model setup as well as parametric and resonant frequency analyses in 3D.

3.1.1 CMUT Model Setup

A 3D CMUT cell was modeled in COMSOL Multiphysics®. Simulating in 3D would help one to better visualize the behavior of a CMUT cell besides being more stable than 2D or 2D-axial symmetry. The first model was constructed to obtain the resonant frequencies and frequency response of the CMUT, and uses *structural mechanics* subdomain of *MEMS module*. Since the eigen frequency and frequency response analyses are not very time consuming, the entire CMUT cell membrane was constructed. In a second setup, the symmetry option was used to only model half of the CMUT cell in 3D. The latter setup couples *structural mechanics* subdomain with

electrostatics and *deformed mesh* subdomains. The 3D model in COMSOL and its simplified cross section is shown in figure 13.

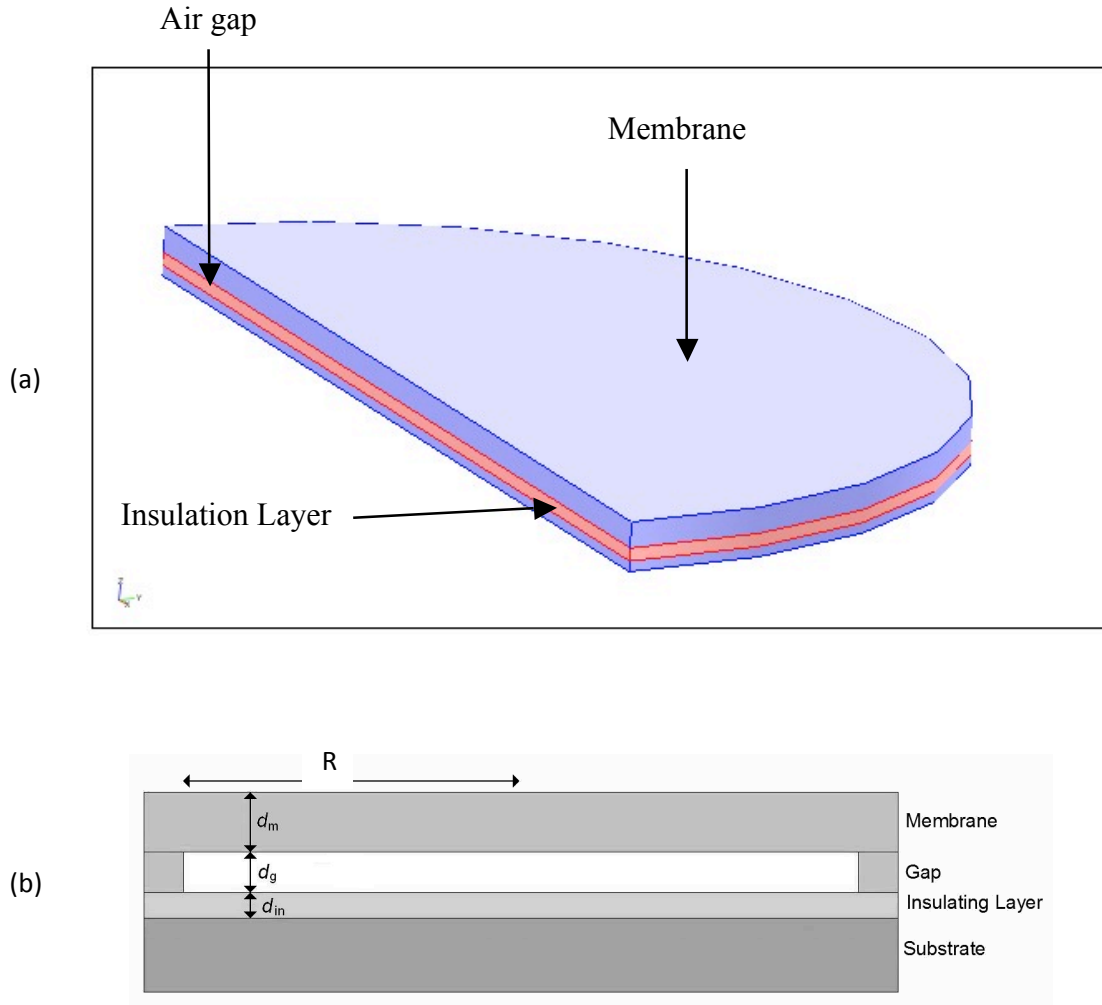


Figure 13. (a) Finite element model setup in COMSOL showing half of CMUT cell, (b) Simplified cross-section of the CMUT cell model[15]

For simplicity, the substrate and the supporting post are not shown in FEM setup. The *structural mechanics* subdomain accounts for mechanical properties of the CMUT behavior and includes the poly-silicon membrane, which is clamped at the boundary, and the stationary silicon nitride insulation on the substrate. The *electrostatics* subdomain is also included to simulate the electric field, the charge on the membrane and electrostatic force by applying a voltage across the device.

Note that the voltage is applied on the membrane, and the substrate is grounded (i.e. bottom of the insulation layer). In FEA of a CMUT, it is important to strongly couple all the fields to ensure accuracy in numerical results. The algorithm of a fully coupled system for non-linear electromechanical devices is displayed in figure 14.

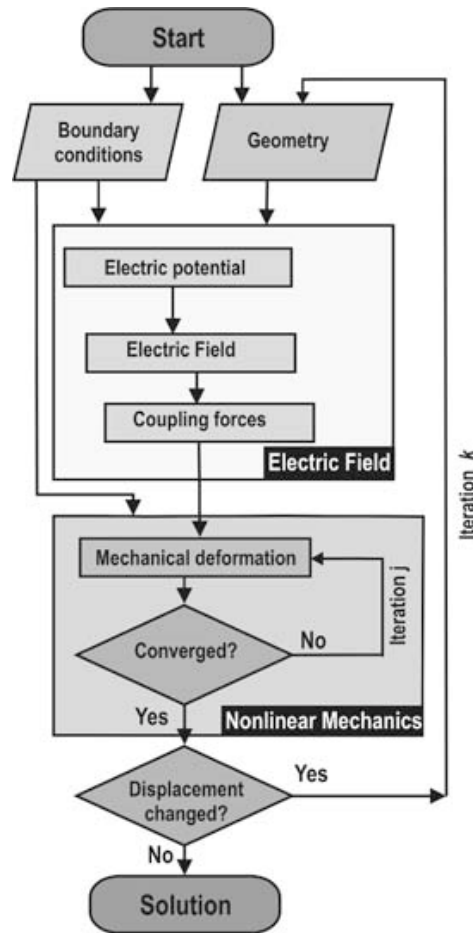


Figure 14. Fully coupled electro-mechanical simulation algorithm for non-linear devices[48]

The *electrostatics* subdomain applies a voltage and generates an electrostatic force on the CMUT membrane. The electrostatic force affects the *structural mechanics* subdomain, which deforms the membrane. The structural deformation decreases the gap distance, which would affect the

electrostatic force in return in *electrostatics* domain and so forth. Thus, one can see the strong bidirectional coupling between the two domains.

When FEA is performed on electrostatic devices, the mechanical structures will move or deform and lead to deformation of electrostatic field finite elements. This would lead to numerical inaccuracy. The finite elements deformations must be controlled and require to be re-meshed before intersection of finite elements. To avoid this problem, *moving mesh* technique is used. In this technique, the electric field finite elements are modified to properly handle mechanical degrees of freedom[48]. Figure 15 illustrates a bar and the effect of *moving mesh* technique on FEM analysis.

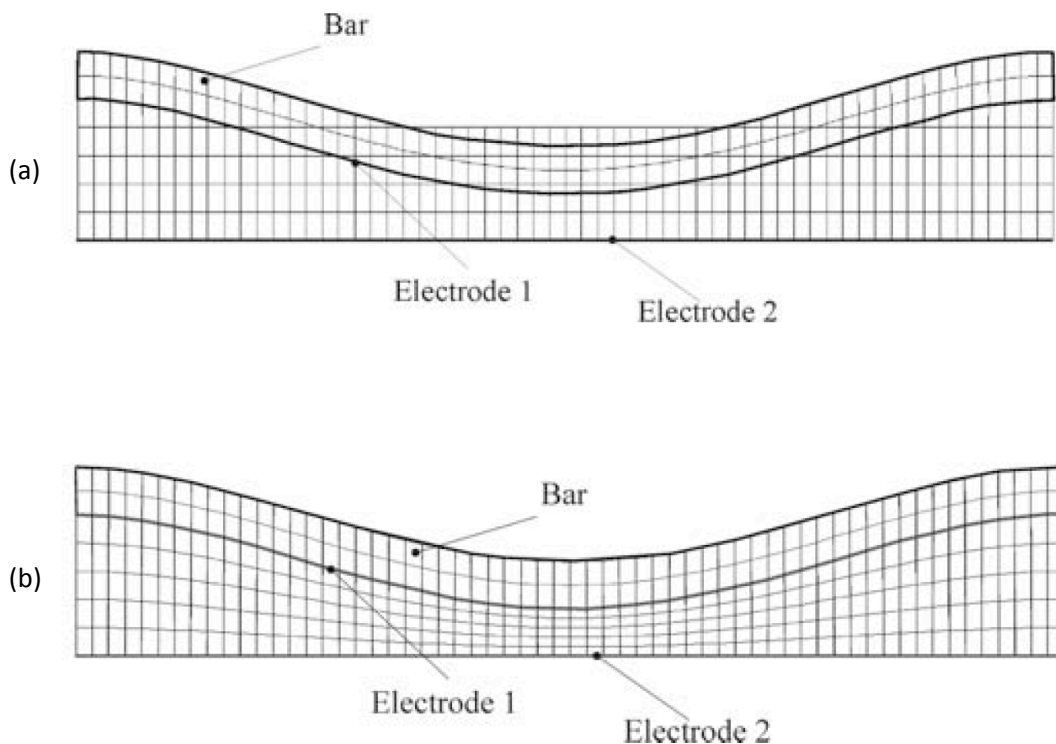


Figure 15. FEM analysis of an electrostatic bar using (a) standard method and (b) moving mesh technique[48].

Figure 15 (a), uses a standard method to perform FEA on an electrostatic bar illustrating the intersection of finite element as the analysis progresses. On the other hand, in figure 15 (b), the deformation of the bar acts on all finite elements between the top and bottom electrodes and not only on the first layer of finite elements beneath the bar. In FEM of the CMUT cell in COMSOL Multiphysics® , *moving mesh technique* is applied using *deformed mesh* subdomain to ensure numerical accuracy. The following sections describe FEA of a CMUT cell based on the parameters listed in table 3 in section 2.3. For a full description on how to setup and model a CMUT cell in COMSOL Multiphysics® refer to Appendix A.

3.1.2 Eigen Frequency Analysis and Frequency Response

In designing CMUTs, eigen frequencies and mode shapes are of particular interest. Resonant (eigen) frequencies present the maximum responses of a system and resemble the characteristics of an under-damped system. Eigen frequency analysis also determines the membrane's higher-order vibrational resonances, which cannot be determined using other types of analyses. The first five mode shapes and the meshed CMUT structure for this type of analysis are shown in figure 16. Note that the eigen frequencies in figure 16 are purely due to mechanical properties of the membrane. The frequency shift due to spring softening effect is discussed in section 3.1.3.2.

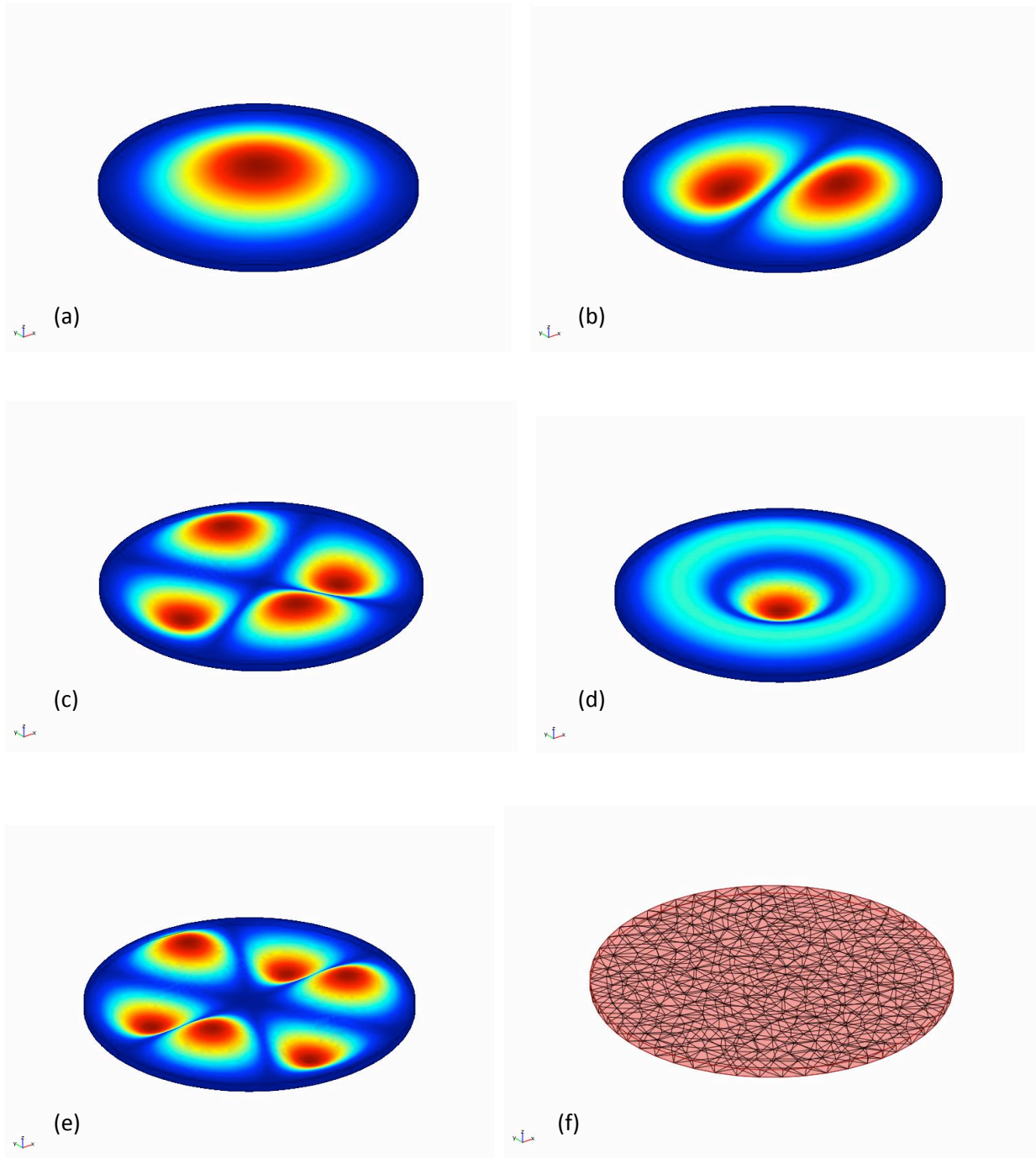


Figure 16. First five eigen frequency modes of the designed CMUT membrane (a)-(e) and the meshed structure (f). The eigen frequencies are (a) 5.86 MHz, (b) 12.21 MHz, (c) 20.02 MHz, (d) 22.83 MHz, (e) 29.73 MHz

Note that the colors show the relative displacement where the warmer colors show larger displacements. Observe that the first resonant mode, **5.868 MHz**, is in close agreement with the analytical value, **5.851 MHz**, in section 2.2.2. Furthermore, the first harmonic is a suitable mode for CMUT operation and the other frequency modes are not required for uneven shapes of membrane and hence non-uniform pressure radiation[49]. One can further investigate the resonant frequency and obtain the frequency response of the CMUT membrane as shown in figure 17.

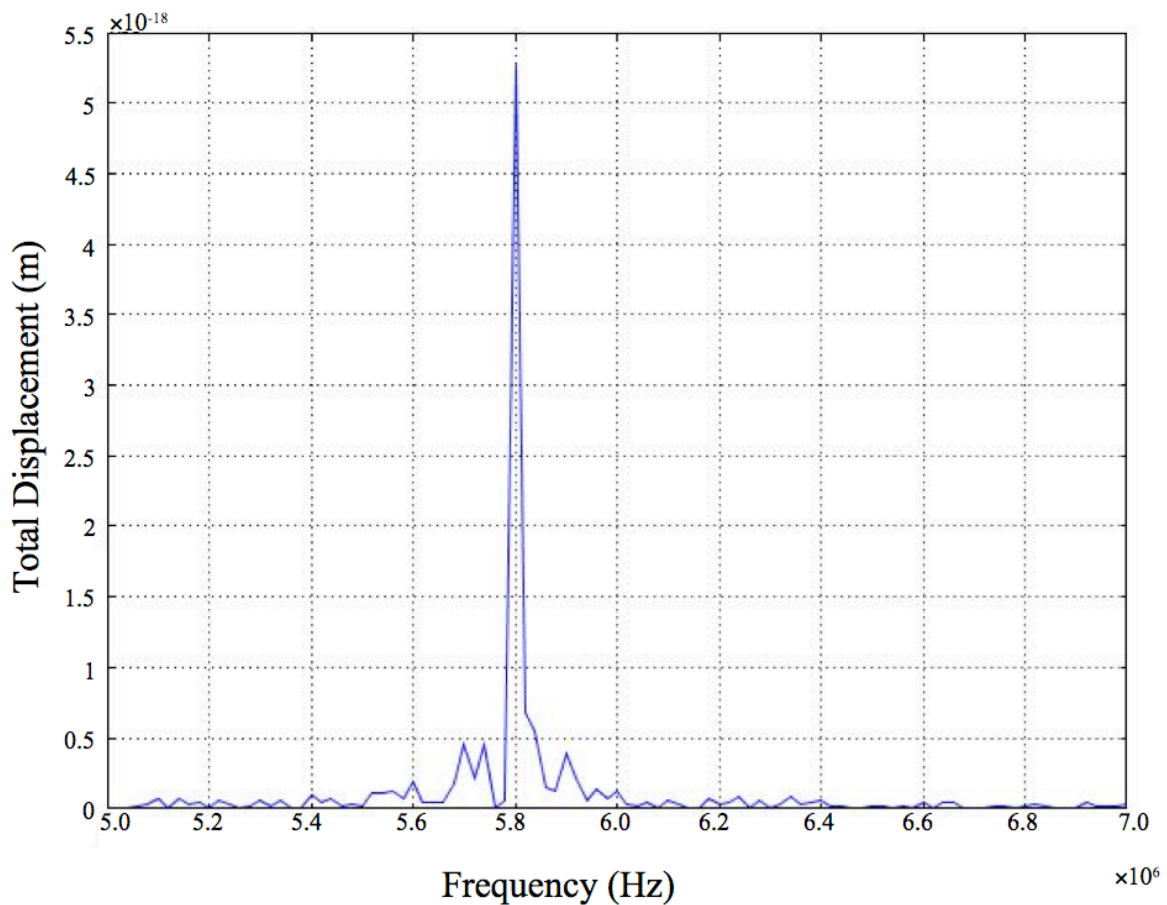


Figure 17. The frequency response of the CMUT membrane

3.1.3 Parametric Analysis

To fully characterize the CMUT cell, it is required to perform parametric finite element analysis. In order to find phenomena such as pull-in and spring softening, and to obtain electromechanical coupling coefficient, parametric analysis needed to be performed with *voltage* being the varying parameter. Parametric analysis is a sequence of static analyses, which solves the electric field within the air gap and the structural deformation. The electric field calculation uses the differential form of electrostatic equation:

$$-\nabla(\epsilon\nabla V) = 0 \quad \text{Eqn. 31}$$

The force density that acts on the CMUT membrane results from the Maxwell's stress tensor:

$$F_{es} = -\frac{1}{2}(ED)n + (nE)D \quad \text{Eqn. 32}$$

where E the electric field vector, D is electric displacement vector, and n is the outward normal vector of the boundary. The orientation of this electrostatic force is always normal to the boundary[50]. To solve the coupled field physics, *parametric segregated* solver was used instead of normal *parametric* solver with *Direct (SPOOLS)* linear system solver. The reason is that *parametric segregated* solver, solves the model sequentially and thus is memory efficient. The parametric analysis took approximately 2.5 hours on a 2.80 GHz desktop PC.

3.1.3.1 Pull-in Phenomenon

To perform the parametric analysis, a range of voltages is applied and the model is run through a sequence of static analyses for different parameter values. Every sequence follows through a certain number of iterations as was shown in figure 14 and the convergence is inspected. The

process is repeated and the voltage is incremented until the membrane is about to contact the insulation layer. At this point, the solution ceases to converge and the simulation simply terminates. The last voltage value before divergence of the solution is the pull-in or collapse voltage. The pull-in voltage with our design parameters was found to be $V_{collapse} = 275V$. One can further investigate the variation in capacitance and displacement before reaching the pull-in voltage. Figure 18 shows the centre point displacement of a CMUT cell when the voltage is increased from 5 V to pull-in voltage.

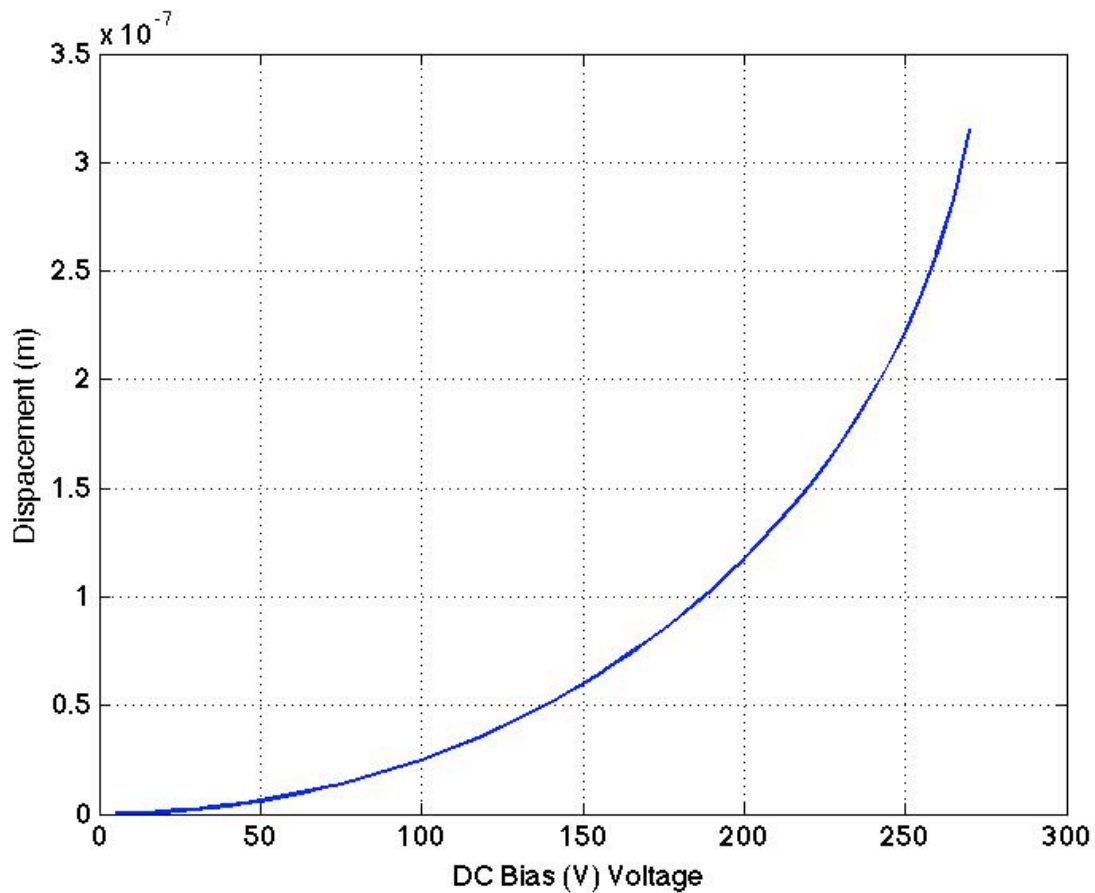


Figure 18. Membrane displacement versus DC bias voltage illustrating the collapse/pull-in phenomenon for FEM model

Observe from figure 18 that at pull-in the CMUT membrane displacement is **0.315 μm** . This value is larger than one third of the gap distance. The CMUT uses the air gap distance more effectively than a parallel plate capacitor and uses **42%** of the air/vacuum gap before it collapses. The error between the analytical and FEM displacement results at pull-in is calculated as following:

$$\%Error = \frac{|x_{analytical} - x_{FEM}|}{x_{FEM}} \times 100 = 20.635\% \quad \text{Eqn. 33}$$

The reason for this error is due to the fact that the CMUT membrane does not move like a rigid-piston. In reality, the membrane shape is curved with no displacement at the fixed outer edges and large displacement at the centre. Figure 19 illustrates the bowl-shape membrane of a CMUT when various DC voltages are applied.

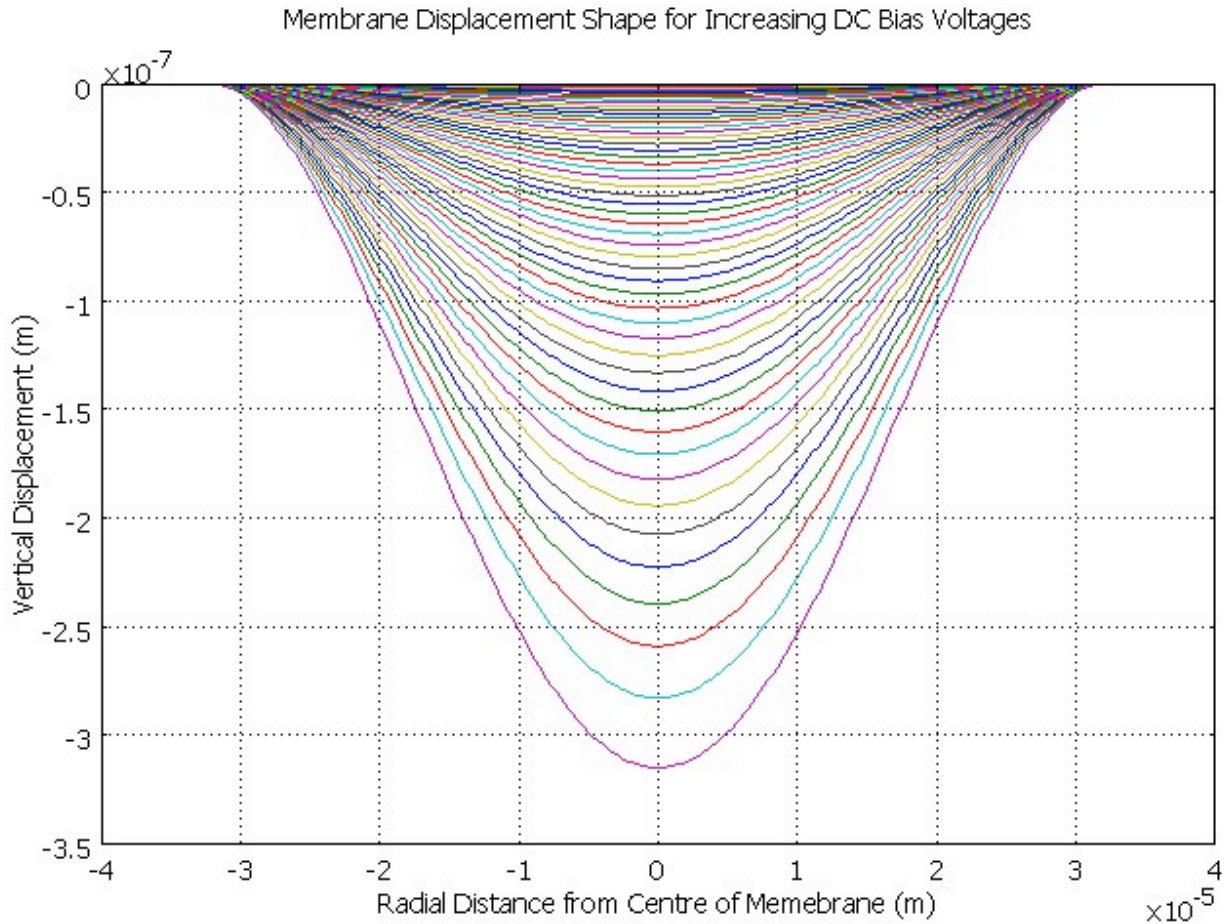


Figure 19. Shape of the membrane for increasing DC bias voltages. The curves progress from top to bottom in steps of 5V from 80V-270 V

Note that the large DC bias voltages cause a greater membrane curvatures and maximum displacements. The same analysis could be performed for capacitance variation of a CMUT cell to determine the pull-in voltage. Figure 20 illustrates the CMUT cell capacitance with varying DC bias voltages.

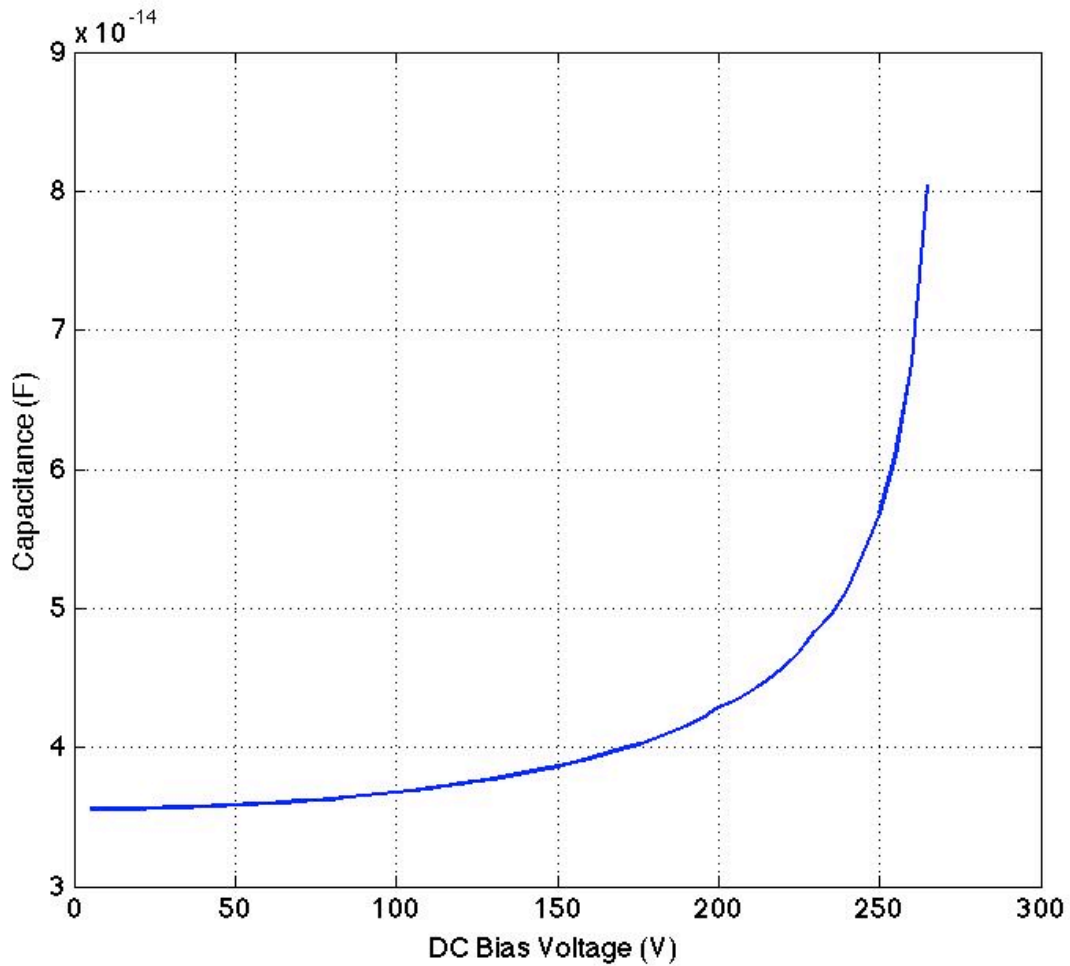


Figure 20. Capacitance of a CMUT with increasing DC bias voltage in steps of 5V from 5V to collapse voltage, 270V

The same error analysis could be performed for capacitance at pull-in point using equation 33. To calculate the analytical capacitance at pull-in, the capacitance equation 25 was used with pull-in displacement being equal to one third of the initial gap distance. The error between analytical and FEM is then **29.18%** as shown bellow:

$$\%Error = \frac{|C_{analytical} - C_{FEM}|}{C_{FEM}} \times 100 = \frac{|56.94 fF - 80.40 fF|}{80.40 fF} \times 100 = 29.180\% \quad \text{Eqn. 34}$$

The capacitance values extracted from FEA is further used to obtain the electromechanical coupling coefficient in section 1.1.3.3.

3.1.3.2 Spring Softening Effect

As explained in section 2.2.3, the spring constant varies as different DC bias voltages are applied. This apparent variation in spring constant is called spring softening effect, which is due to non-linearity of the CMUT electrostatic force. The spring softening effect was derived analytically in section 2.2.3, and the spring constant was plotted versus increasing DC bias voltages for a CMUT cell of our defined geometry. To validate the results, FEA was performed and the spring constant was extracted. Figure 21 clearly illustrates the spring softening effect as applied voltage is increased. The solid and dashed plots depict the FEA and analytical spring constants, respectively.

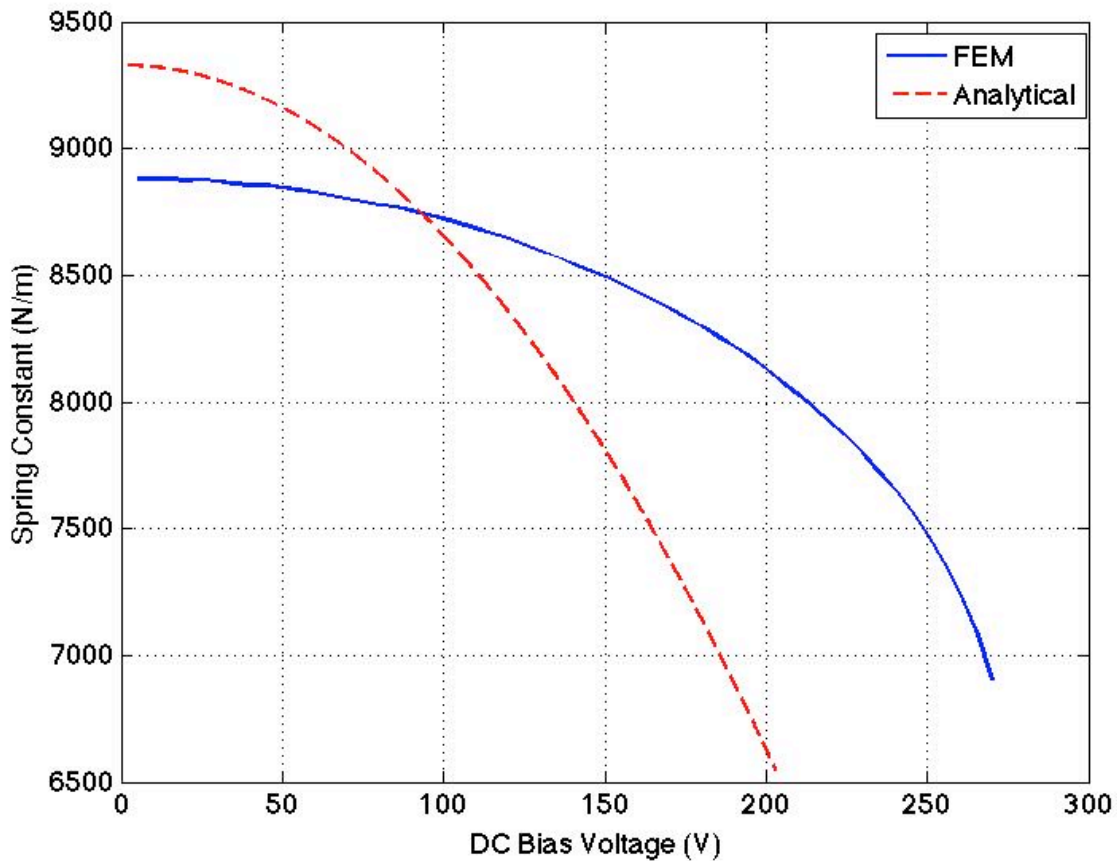


Figure 21. Spring constant of a CMUT cell versus increasing DC bias voltages depicting spring softening effect

Note that the maximum error occurs at pull-in, and the percentage error of FEM and analytical results at pull-in is **18.99%**. In a similar approach, the decrease in resonant frequency can be simulated as the spring softening occurs. Figure 22 illustrates the decrease in resonant frequency using FEM –solid line – and analytical modeling – dashed line –.

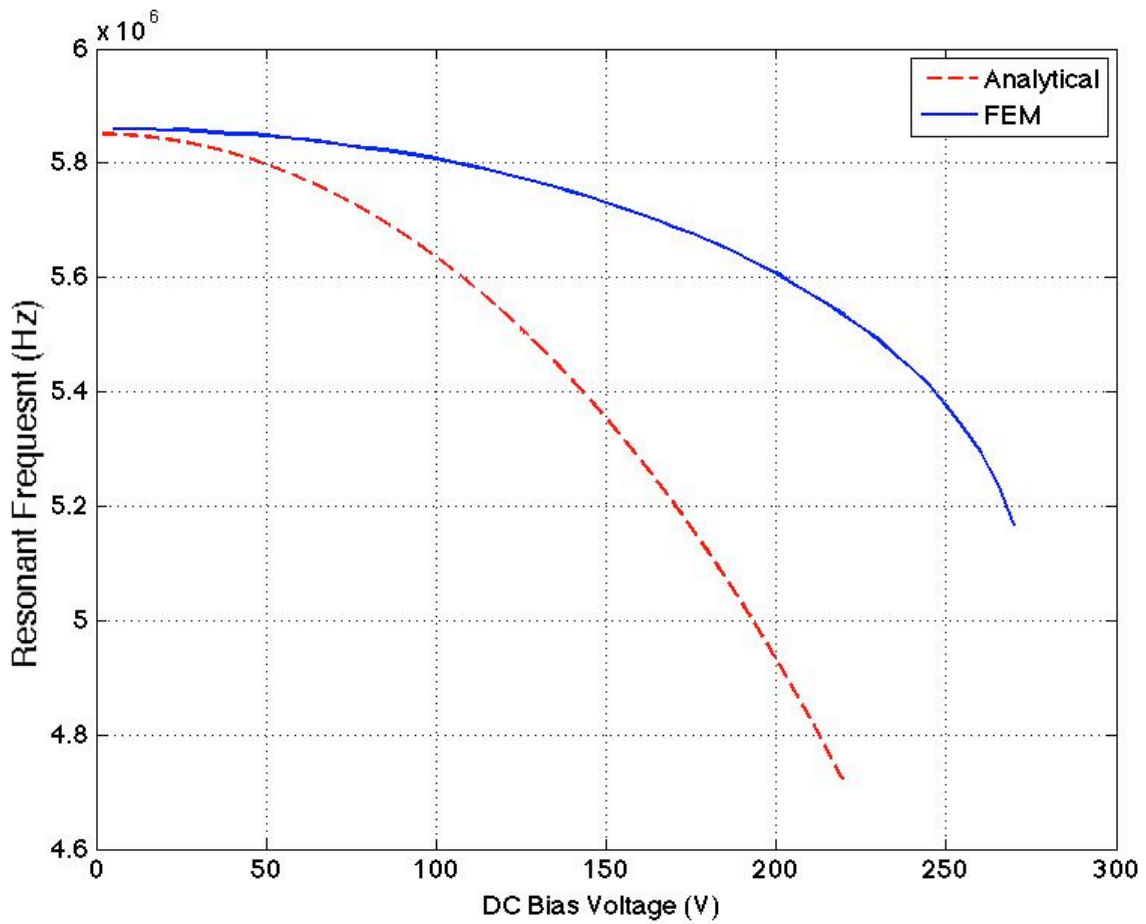


Figure 22. Decrease in resonant frequency versus increasing DC voltage for FEM shown by solid line and analytical modeling shown with dashed line

If the CMUT were to be biased at 80% of pull-in voltage, the resonant frequency shifts by **326KHz** and would drop to **5.534 MHz**. Furthermore, the percentage error at this DC biased voltage between analytical result and FEM result is **14.78%**.

3.1.3.3 Electromechanical Coupling Coefficient

Electromechanical coupling coefficient, k_T^2 , is the ratio of mechanical energy of the CMUT to the total energy stored in CMUT structure. This coupling coefficient was thoroughly calculated and explained in section 2.2.4, analytically. To obtain this important coefficient using FEM, the fix capacitance of a CMUT cell, C^S , and its slope with respect to voltage (i.e. free capacitance, C^F) were computed using the FEM software. Using the concept of fix and free capacitances (i.e. equation 22 and 23) and the coupling coefficient equation (i.e. equation 24), one can plot the electromechanical coupling coefficient, k_T^2 , of a CMUT cell, versus increasing DC voltages as shown in figure 23.

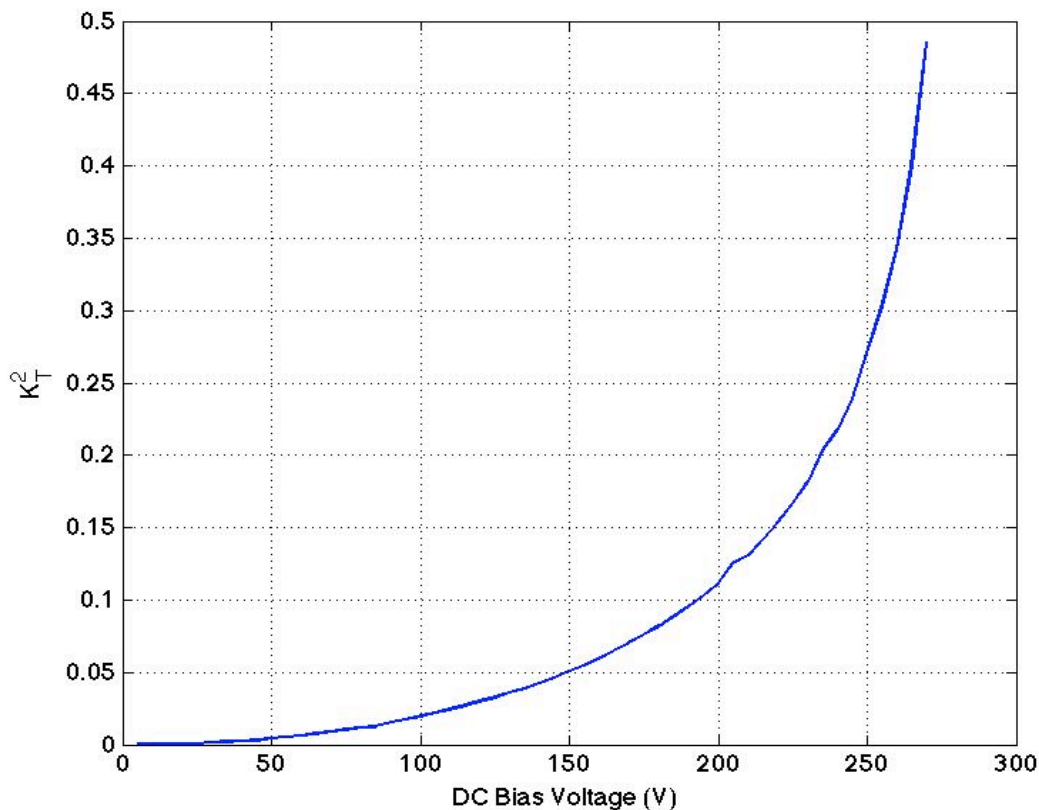


Figure 23. Electromechanical coupling coefficient of a CMUT cell versus increasing DC bias voltage from 5V to pull-in voltage

As the figure illustrates, the nearer the CMUT is biased to pull-in voltage, the more efficient its operation would be. This agrees with previously reported results[51] and depicts the bias voltage to be an essential parameter in determining CMUT efficiency.

3.2 Behavioral Modeling with VHDL-AMS of CMUT

Implementing and simulating the CMUT using numerical method (i.e. FEM) is time consuming and in some cases complex. To avoid performing lengthy simulation or prior to investing in fabrication, the performances of CMUT designs were examined using a developed behavioral model. The behavioral modeling has proven to reach quicker solution than FE simulation and more accurate than analytical modeling. It can further be incorporated into a macromodel along with models of the driving and receiving electronics. This is a notable advantage in the case where the CMUT and the electronics are to be fabricated on the same IC chip. It also allows the whole IC, which includes MEMS and CMOS layers, to be simulated together and gives the ability to optimise the parameters of the CMOS electronics with those of the CMUT.

As explained in section 2.3, The behavioural model developed in this work is different from previous models in that it is not based on a linearised small-signal model. That means, the inherently non-linear relationships between electrical and mechanical domains are preserved. Moreover, the model is bidirectional and has the ability to be used as a transmitter and a receiver. The CMUT model was implemented in VHDL-AMS (IEEE Std 1076.1-1999), for the first time by Frew. et al.[15]. The advantage of this implementation of CMUT in VHDL-AMS is that the software is a well-recognised standard and compatible with various software platforms, allowing the MEMS transducer to be simulated in different environments.

The CMUT was modeled as a moveable plate capacitor as was shown in figure 3 of section 2.2.

In havioural modeling, a damper component, B , was added to the diagram to represent the acoutic medium damping, as shown in figure 24.

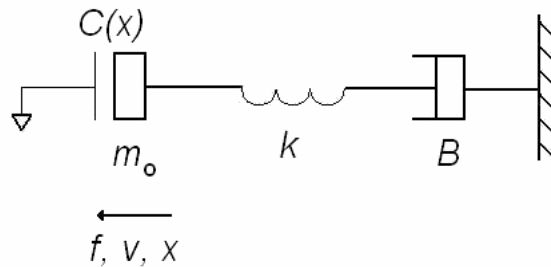


Figure 24. Modified diagram of the CMUT as a moveable plate capacitor attached to a mechanical spring-damper system [15]

The relation between damping coefficient, B , and the charaterstic acoustic impedance of the acoustic medium, Z_0 , is:

$$B = Z_0 A = (\rho c) A \quad \text{Eqn. 35}$$

where A is the surface area of the CMUT membrane, ρ is the density of the medium and c is the speed of sound in the medium. The equivalent circuit model was previously derived and explained in section 2.3 and the full circuit for CMUT was shown in figure 12.

The VHDL-AMS model of CMUT was implemented in the software package Simplorer (Ansoft, LLC, Pittsburgh, PA, USA) for simulation as the software has the ability to import and integrate the model with electrical components from its standard libraries. The CMUT VHDL-AMS model was imported as a two-port component with force and velocity in mechanical domain being analgous to current and voltage in electrical domain, respectively. Note that velocity and force, similar to voltage and current, are cross and through variables, repectively[30].

In transmission mode, to represent the driving electronics, a voltage source was attached to electrical port, and to represent the acoustic medium, a resistive load was connected to mechanical end as shown in figure 25.

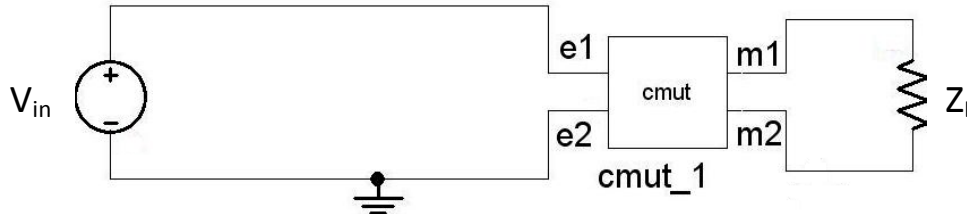


Figure 25. Complete Simpler circuit used for transmission simulations[15]

In the schematic, the “*cmut_1*” block contains the CMUT equivalent circuit as was shown in figure 12, and the electrical load resistance, Z_L , is inversely proportional to the damping coefficient, B :

$$Z_L = \frac{1}{B} \quad \text{Eqn. 36}$$

3.2.1 Frequency Analysis

To observe the frequency response of the CMUT using the equivalent circuit, the input voltage was set to generate a sinusoid with 20 V peak amplitude superimposed on a 90 V DC bias voltage. Using equations 35 and 36, the load Z_L was calculated to be 725.01 k Ω , 201.85 Ω for water and air transmission simulations, respectively. The output power density frequency responses in air and water are shown in figure 26. In air response, the behavioral model presents a sharp resonant peak at **5.78 MHz**. In water response, there is no distinct resonant peak but a much higher bandwidth (i.e. approximately **115 MHz**).

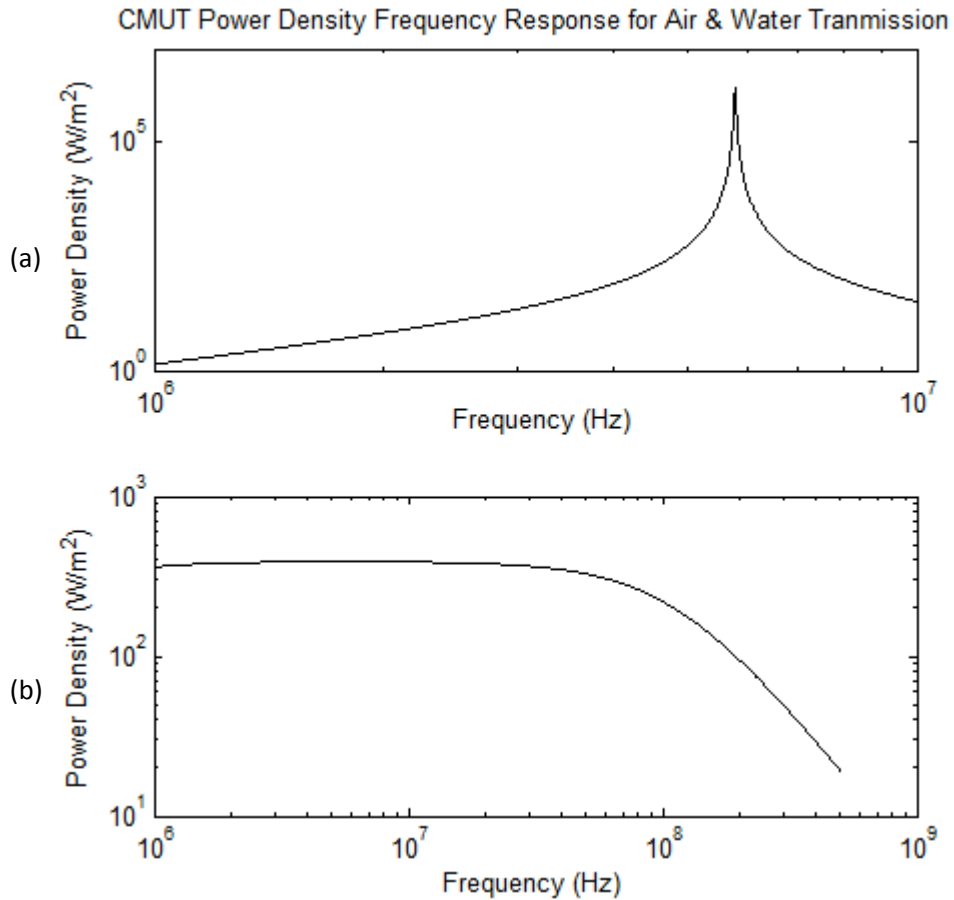


Figure 26. Power density frequency responses of CMUT for (a) air transmission and (b) water transmission[15]

One can compare the air response from behavioral modeling and observe that the result is close to **5.86 MHz** obtained from FEM. The error in this case is **1.226%**.

3.2.2 Pull-in Analysis

The behavioral modeling has the advantage to model non-linear nature behavior of CMUT to investigate its pull-in phenomenon. The displacement of the CMUT membrane with increasing DC bias voltage was simulated in Simplorer and is shown in figure 27 with FEM result.

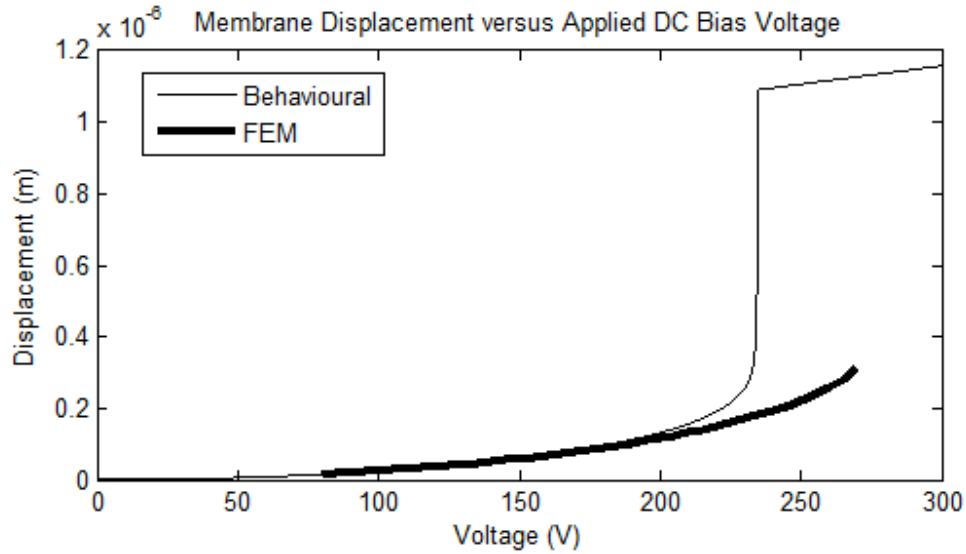


Figure 27. CMUT membrane displacement versus increasing DC bias voltage indicating pull-in phenomenon[15]

The thick solid line represents the FEM and the thin line represents the behavioral results. The large discontinuity in the behavioural model shows the pull-in voltage and occurs at approximately **230 V**. At higher voltages, the given displacement exceeds the value of d_g , indicating an invalid solution. The displacement at pull-in is approximately **$0.265 \mu\text{m}$** for behavioural model. The pull-in voltage and displacement results from FEM were **275 V** and **$0.315 \mu\text{m}$** , respectively. Notice that the FEM terminates the simulation when the solution ceases to converge, and thus the plot simply stops. The behavioural model and FEM pull-in simulations indicated a good agreement for voltage and displacement. As mentioned previously, the error comes from the piston-movement assumption of the CMUT membrane rather than bowl-shape movement. The piston-movement assumption causes a lower pull-in voltage and displacement since parallel plate undergoes a higher electrostatic force compared to a curve plate with the same centre point displacement for a given bias voltage.

The error in behavioral model for *pull-in voltage* is approximately **16.36%** due to mentioned assumptions, which is yet a great improvement to previously reported errors of **30-40%** for parallel plate approximation[52]. The behavioural model *displacement* error is approximately **15.87%**. The important behavioral, FEM and analytical results and the corresponding errors between behavioral and FEM results are summarized in table 4.

Symbol	Behavioral	FEM	Analytical	Error	Parameter
$V_{collapse}$	230 V	275 V	202.3 V	16.36%	Pull-in Voltage
$x_{collapse}$	0.265 μm	0.315 μm	0.25 μm	15.87%	Pull-in Displacement
C_0	35.08 fF	35.56 fF	37.98 fF	1.35%	Cell base Capacitance
f_0	5.78 MHz	5.71 MHz	5.67 MHz	1.226%	Resonant frequency

Table 4. Summary of FEM, behavioral and analytical results and the relative behavioral and FEM error

The behavioral modeling in VHDL-AMS was proven to be a suitable model to be used prior to lengthy FEM simulation and costly fabrication. The behavioral modeling results in more accuracy and flexibility than previously reported models, for the model being able to simulate the non-linear nature of the CMUT without linearization. The behavioral simulation took 3.1s on a 2.8GHz desktop PC with 4GB of RAM.

Chapter 4

Fabrication

Fabrication is a crucial step after performing designing and analyzing a MEMS device. Thus, various fabrication techniques are described, in this section. Previously fabricated CMUTs used both surface micromachining (sacrificial release process) and bulk micromachining (wafer bonding process). In this work, a third fabrication process was introduced using PolyMUMPs, which is explained, in section 4.2. It is worth noting that other novel in-house approaches using polymers have been initiated.

4.1 Previously Fabricated Processes

In this section two important fabrication processes are explained that were used previously to fabricate CMUTs: *surface micromachining (sacrificial release process)* and *bulk micromachining (wafer bonding process)*. Note that fabricating CMUTs with our designed geometry requires precise masking alignment (i.e. less than one micron) and special equipment. Having the equipment in the future would enable to step towards in-house silicon-based fabrication.

4.1.1 Surface Micromachining

Although there are many ways of fabrication CMUT cells or arrays using surface micromachining, it should suffice to introduce only one simple method. For other approaches of sacrificial release process one may refer to [16],[53],[35],[54],[34],[55]. Detailed surface micromachining fabrication process is shown in figure 28.

CMUT cell fabrication with accurate geometric dimensions requires doping a silicon wafer with the appropriate dopant to obtain a high conduction at the surface. This doped surface will then act as the CMUT back electrode. A silicon nitride (Si_3N_4) layer is then deposited on the silicon substrate to form an etch stop layer as well as an insulation layer to protect the CMUT from short-circuiting at collapse. Since the insulation layer introduces a series capacitance with active gap capacitance, it cannot be arbitrary thick. Typically less than a micron thickness is used. Deposition and patterning sacrificial layer is performed in two steps so that the channel used to release the sacrificial layer is thinner than the gap distance. The sacrificial layer used in this work is poly-silicon. The first step, a layer of poly-silicon is deposited using LPCVD. Using photolithography, regions of reduced channel heights are defined as shown in figure 28 (a). Note that dry etch is used to completely remove all poly-silicon layer in the defined region, which would eventually stop at etch-stop layer (i.e. Si_3N_4). A second thin layer of poly-silicon is then deposited (Fig. 28(b)). The thickness of the second layer of poly-silicon is the thickness of the sacrificial release channel. The first and second layer of poly-silicon determines the height of the cavity. Depositing both poly-silicon layers requires a low deposition temperature (560°C) to have control over both thicknesses [16]. A second photolithography and dry etch is performed to define the membrane shape, the etch channels and the cavity (Fig. 28(c)).

The next step is to create the membrane by depositing silicon-nitride using LPCVD at 785°C (Fig. 28(d)). Since a low-stress silicon nitride film is desired, the composition of gasses is of crucial importance (dichlorosilane to ammonia ratio of 14:1 [16]). This is not the final membrane thickness since another layer of silicon nitride is yet to be deposited to seal the cavity. A lithography and dry etch step creates release holes through the silicon nitride membrane (Fig. 28(e)). The wafer is then immersed in KOH solution to etch away the sacrificial layer and release the membrane. Note that the poly-silicon etch rate of KOH is dependant on the temperature[56]. The temperature choice depends on the size of the membrane and cavity. Typically, the temperature should be above room temperature for in room temperature it would take days for poly-silicon to be completely etched away.

Subsequently, another layer of silicon nitride is deposited to seal the cavity and to form the final thickness of the membrane (Fig. 28(g)). Because the deposition process is done in low pressure using LPCVD (200mTorr at 785°C [16]), the cavity is assumed to be vacuum-sealed. The top electrode is formed by sputtering a thin layer aluminum or gold over the whole wafer. The metal layer is then patterned with lithography and wet etch (Fig. 28(h)).

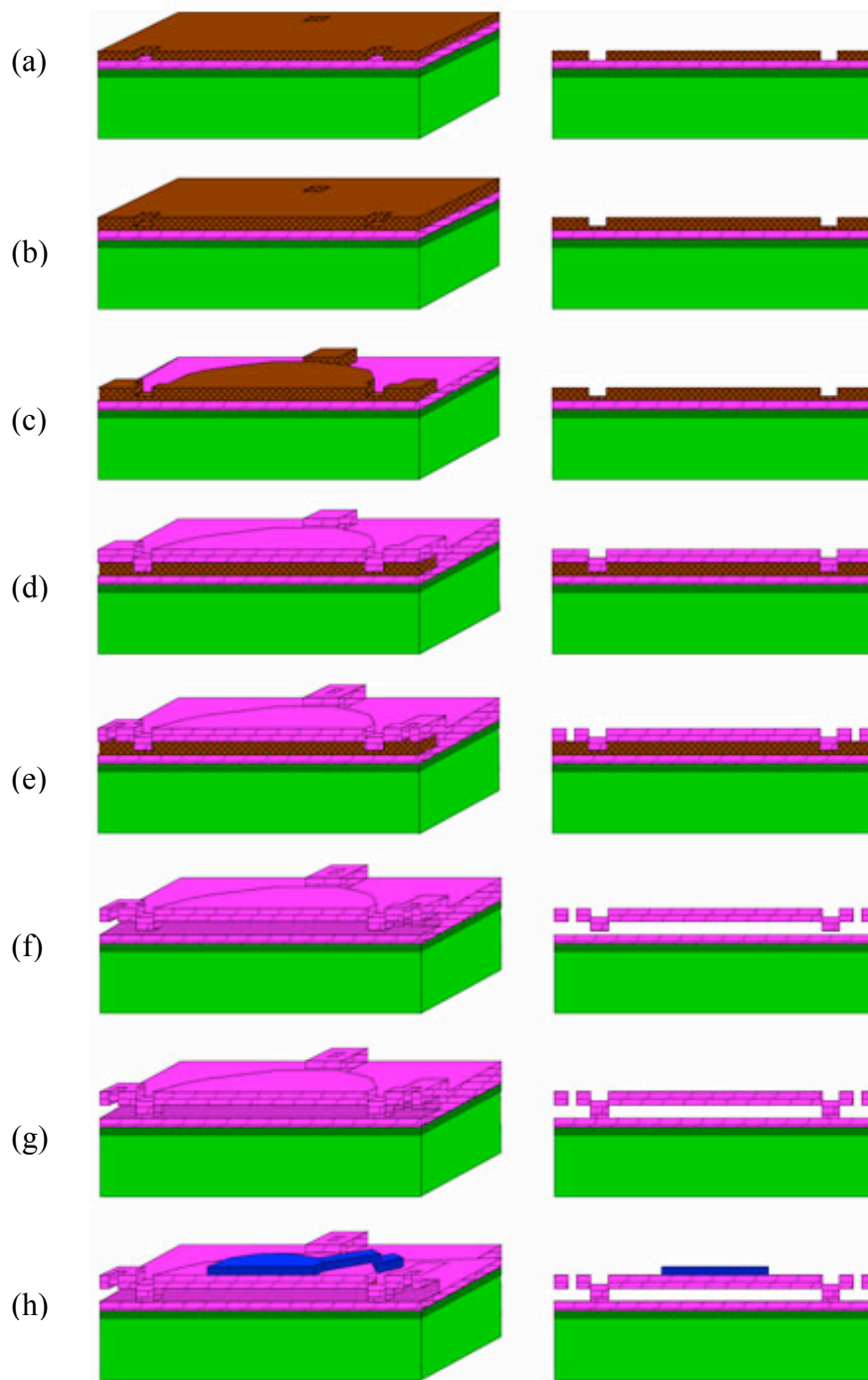


Figure 28. Surface micromachining (sacrificial release process) of CMUT cell, (a) substrate doping, deposition of insulation layer (LPCVD Si_3N_4), deposition of first sacrificial layer (LPCVD poly-Si), (b) deposition of second sacrificial layer, (c) patterning the CMUT shape, (d) deposition of membrane, (e) create release holes, (f) membrane release (wet etch KOH) (g) sealing membrane (LPCVD Si_3N_4), (h) depositing top electrode and patterning [16]

4.1.2 Bulk Micromachining

Bulk micromachining is a fabrication process, which is yet widely used and is older than surface micromachining process. *Wafer bonding*, which is a bulk micromachining process, consists of three techniques: anodic bonding, fusion bonding, and adhesive bonding. Among these three techniques, silicon fusion bonding is a more advanced technique in today's technology and is used for many MEMS applications. CMUTs can also be fabricated using the silicon fusion bonding technique.

Fabricating CMUTs using wafer bonding[57] requires a primary silicon wafer and a Silicon-on-Insulator (SOI) wafer. The first step is to thermally grow oxide on the silicon wafer. The thickness of the thermal oxide determines the thickness of the cavity. A photolithography step is used to define the shape of the cavity. The oxide is then wet etched using HF or dry etched to the silicon substrate, as shown in figure 29 (a). It is required to deposit a layer of insulation to avoid short-circuiting between the top electrode and the conductive substrate at pull-in. Therefore, another layer of silicon dioxide is thermally grown (Fig. 29(b)). Note that the thermal oxide is a well-controlled process and thus the cavity depth can be precisely controlled. After the second oxide layer, the SOI wafer is brought to the prime wafer (Fig. 29(c)). As soon as the two wafers come to proximity, the Van der Waals forces and weak hydrogen bonds are formed. To make strong covalent bond, the wafer are annealed at 1100°C. After annealing, the silicon thickness of SOI wafer is reduced to 50µm -100µm with a grind step. Silicon is removed by wet etch using KOH or TMAH. The next step is to remove the buried oxide using hydrofluoric acid, which stops at the silicon membrane (Fig. 29(d)). Eventually, the top electrodes are sputtered and patterned by a photolithography and wet etch step (Fig. 29(e)). The final step is to define the elements by etching isolating trenches as shown in figure 29(f)[58].

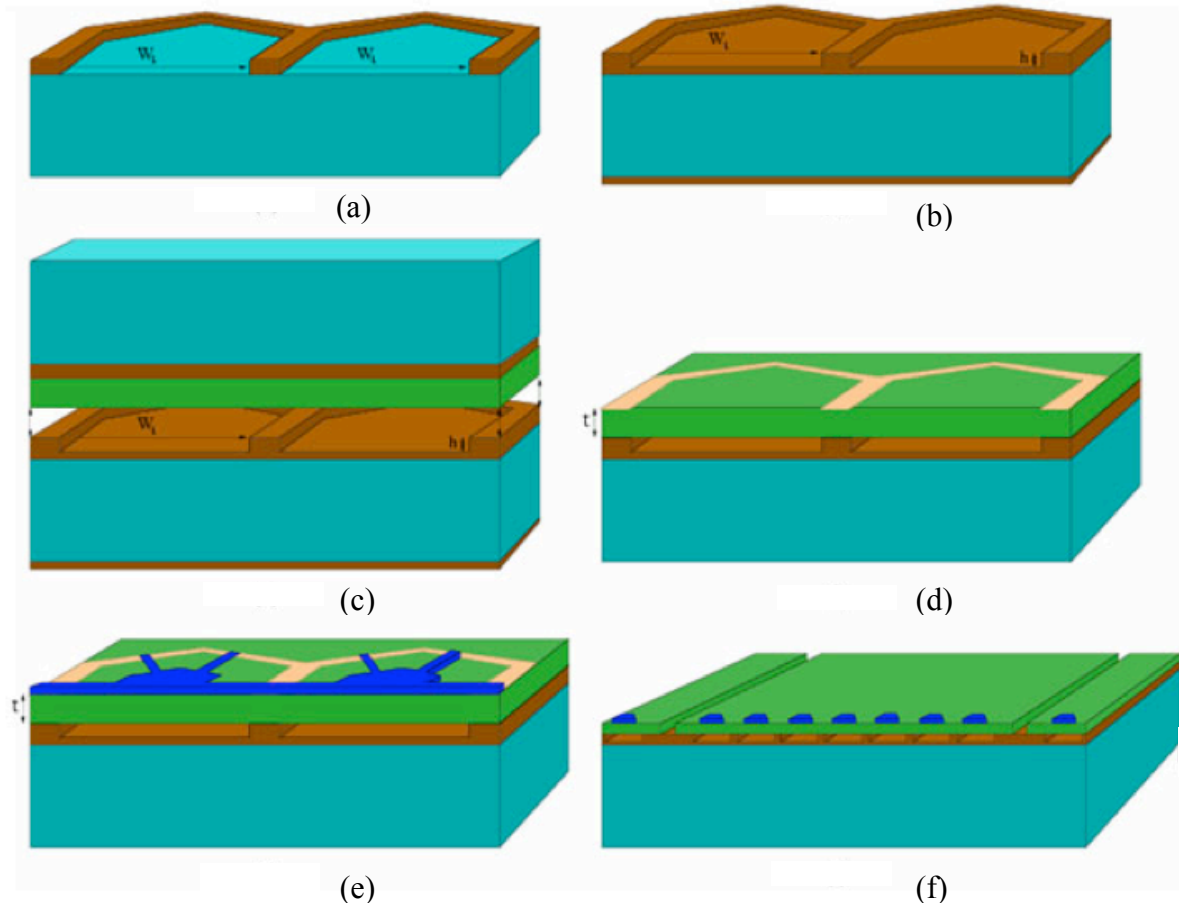


Figure 29. Bulk micromachining (wafer bonding process) of CMUT cells, (a) thermal oxide growth on the prime wafer and defining the cavity using photolithography and patterning step (b) growth of a second oxide layer for insulation purposes (c) direct bonding of SOI wafer to the prime silicon wafer (d) removal of top silicon layer and the buried oxide layer to release the membranes (e) sputtering metal and using photolithography and patterning step to form electrodes (f) photolithography and etching silicon to define elements [16]

4.2 Fabrication with PolyMUMPs Technology

CMUTs were decided to be fabricated using PolyMUMPs process. PolyMUMPs is a three-layer poly-silicon surface micromachining process and is a precise, accurate and well-established fabrication technology. Another advantage of PolyMUMPs process is that it is compatible with mass production, allowing the design to be easily transferred from experimental to commercial fabrication in the future. The PolyMUMPs process consists of seven layers in total: 1 nitride layer, 3 poly-silicon layers, 2 oxide layers and a metal layer. The nitride layer is used for insulation and has a fix thickness of $0.6\mu\text{m}$. The two oxide layers are used as sacrificial layers and have thicknesses of $2\mu\text{m}$ and $0.75\mu\text{m}$. The three poly-silicon layers are used as structural layers and have thicknesses of $0.5\mu\text{m}$, $2\mu\text{m}$ and $1.5\mu\text{m}$. The metal layer is the last layer and is used as metallic contacts of the MEMS structure, which has a thickness of $0.5\mu\text{m}$. Figure 30 illustrates the cross sectional view of PolyMUMPs layers and their thicknesses.

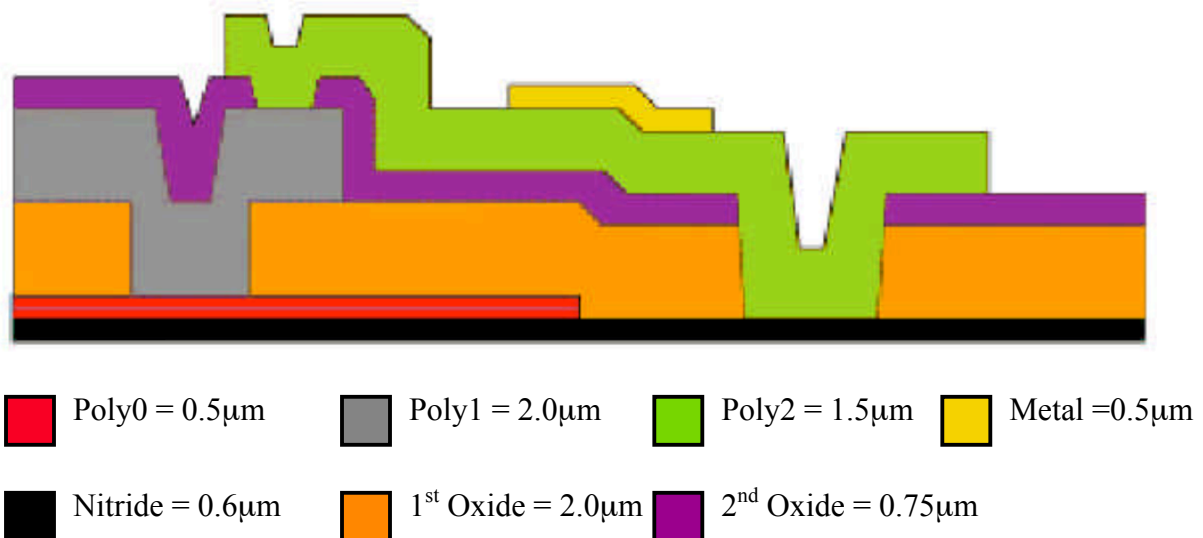


Figure 30. Cross sectional view of 7 layers of PolyMUMPs process [59]

There are five different approaches to fabrication CMUTs in PolyMUMPs, four of which were briefly explained in section 2.2.1. However, only two of these approaches fulfill our CMUT design requirements. The first approach starts by using a heavily p-doped n-type substrate. Silicon nitride is deposited to form the etch-stop layer over the entire substrate as shown in figure 31(a). A layer of poly-silicon (i.e. Poly0) is deposited and patterned using photolithography to create the bottom electrodes, the CMUT posts and the interconnecting tracks (Fig 31(b)). Next is to deposit a layer of silicon dioxide (i.e. Oxide2) to be used as sacrificial layer. The oxide layer is then photolithography patterned and RIE etched to form the cavity (Fig 31(c)). To create the membrane, another layer of poly-silicon (i.e. Poly2) is deposited over the oxide layer, photolithography patterned and RIE etched. This layer would form the CMUT membrane and the top electrode (Fig. 31(d)). The final step is to release the membrane by removing the sacrificial layer. Therefore, release holes were created on the poly-silicon membrane using a photolithography and etching step. The oxide layer is removed through the release holes and the membrane is released by emerging the die into an HF bath for about 2 minutes (Fig. 31(e)). A simplified fabrication process is shown in figure 31.

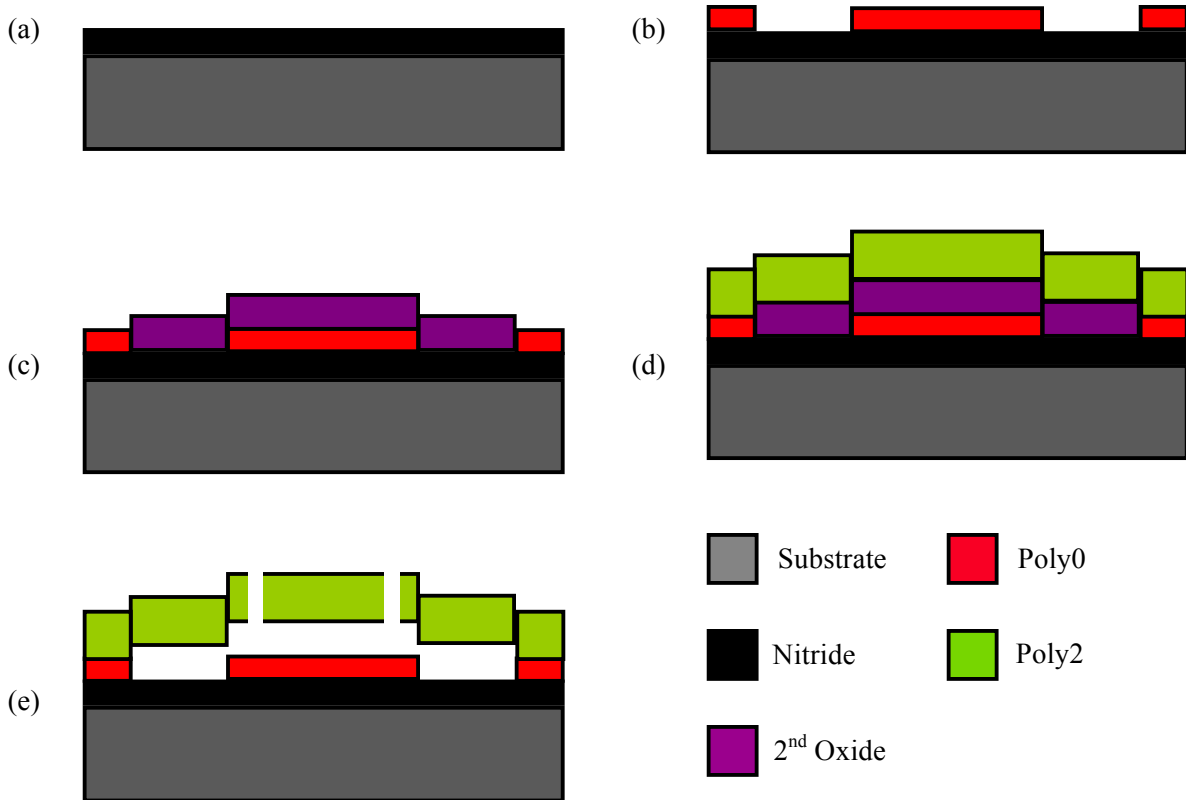


Figure 31. Cross sectional view of a CMUT cell showing fabrication process in PolyMUMPs, (a) deposition of silicon nitride on a doped substrate, (b) deposition of poly-silicon layer and photolithography patterned to be used as bottom electrode and membrane posts, (c) depositing oxide layer as sacrificial layer, (d) deposition and photolithography patterning a poly-silicon layer as top membrane, (e) creating etch holes and releasing the membrane by removing the oxide layer

A complete and detailed fabrication process for general MEMS structures is described in “*PolyMUMPs Design Handbook*”[59], which is widely available on the World Wide Web. Note that no metal was deposited on the top membrane since depositing metals would alter the resonant frequency and pull-in voltage of the CMUT by making its membrane thicker and heavier. Moreover, poly-silicon is adequately conductive to behave as an electrode. In this design, the top poly-silicon membrane has a thickness of $1.5\mu\text{m}$, and the cavity is $0.75\mu\text{m}$. These

values correspond to the third row of table 1. Although this design was very recently reported in literature but was never fabricated [28].

Although this design has many advantages, it yet suffers from having no insulation between the top and bottom electrodes. To prevent the CMUT from short-circuiting, the device needs to be operated away from the collapse voltage.

A second novel approach to fabricate CMUTs in PolyMUMPs uses a similar process with the difference that it uses the substrate as the bottom electrode instead of a poly-silicon layer. To do so, a small area of the deposited nitride layer is breached at the corner of the die to reach the substrate. The breached area is then used as a bond pad and the substrate is grounded through this pad. The rest of the process is to deposit and pattern a poly-silicon layer (i.e. Poly0) as membrane posts, an oxide layer (i.e. Oxide2) as the sacrificial layer, and a poly-silicon (i.e. Poly2) layer as the top electrode and the membrane of CMUT. The final step is to create release holes on the membrane to remove the sacrificial layer and release the membrane. The simplified fabrication process of this approach is shown in figure 33.

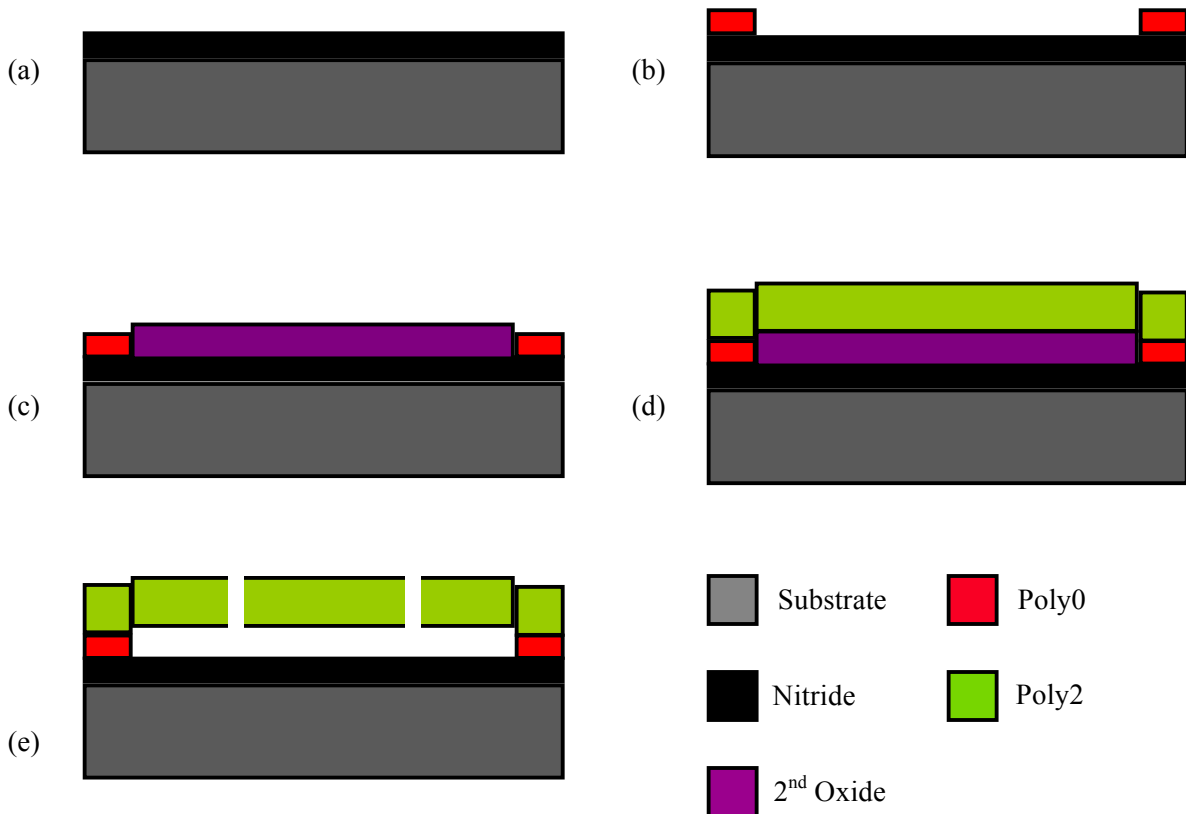


Figure 32. Cross sectional view of simplified fabrication process in PolyMUMPs, (a) deposition of silicon nitride as insulation on a doped substrate, (b) deposition of a poly-silicon layer and photolithography patterned to be used as membrane posts, (c) deposition of an oxide layer as sacrificial layer, (d) deposition and photolithography patterning a poly-silicon layer as top membrane, (e) creating etch holes and releasing the membrane by etching the oxide layer using HF

The advantage of this design is to have an insulation layer between top and bottom electrode. Thus, one can safely operate the CMUTs close to their collapse voltages without any concern of short-circuiting. Note that in both mentioned designs the effect of residual stress on the membrane is present. The residual stress alters the performance of the CMUT. A high residual stress increases and a low residual stress decreases the resonant frequency of the CMUT membrane. In this case, a low residual stress slightly sags the membrane and decreases the resonant frequency. Moreover, CMUTs can be tested in regular and collapse regime [60]. Single

CMUT cells, as test structures, and arrays were fabricated using this latter approach. In array form, 128 CMUT elements with each element containing 118 cells were fabricated. That is the number of elements ultrasound probes generally use, and the fabricated chip can be simply embedded into existing ultrasound machines. Besides poly-silicon, the interconnecting tracks use a 0.5-micron layer of metal atop for better electrical conduction. The dies were packaged using Pin Grid Array (PGA) with 209 pins. The packaged CMUT chip is shown in figure 34. For complete masking layouts, pictures of fabricated CMUTs, and pin configuration refer to Appendix B.

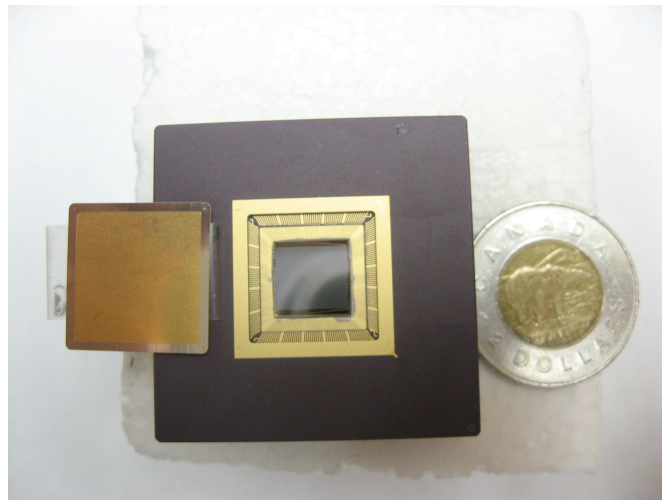


Figure 33. Packaged CMUT chip

Chapter 5

Testing and Characterization

An important step after fabricating a MEMS device is characterization. Characterization would help one to obtain the actual CMUT properties, which could be compared to the modeling results. It also helps to obtain those parameters of the CMUT that could not be determined using the models. The following sections present the experimental setups to characterize the CMUTs.

5.1 Experimental Setup

In this subsection, the experimental setups are presented to obtain the electrical, mechanical and acoustical properties of CMUTs.

5.1.1 Electrical Testing Setup

The electrical characterization helps to obtain important CMUT parameters such as resonant frequency, quality factor, static pull-in voltage, device capacitance, and resistance. Most of these parameters can be acquired by measuring the input impedance of CMUT. The input impedance can be simply measured using a network analyzer and obtaining the scattering parameter (S11).

A schematic of this experimental setup is shown in figure 37.

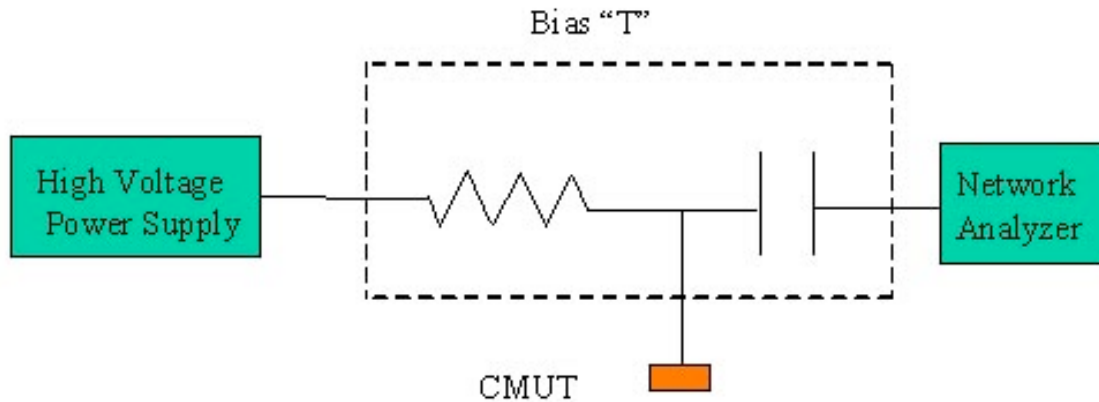


Figure 34. Schematic of experimental setup to measure input impedance [61]

A high voltage power supply is required to provide a DC bias voltage to the CMUT. To protect the network analyzer from high DC voltages, a bias “T” is used. A bias “T” would block high DC voltages and protects the network analyzer from being damaged, while allowing the AC voltage components to pass for impedance measurement. Suitable high frequency network analyzers are available at System-on-Chip (SoC) lab at UBC.

Another approach to determine the device capacitance, resistance and collapse voltage is to use an RLC meter. The experimental setup is similar to what is shown in figure 37, but it uses an RLC meter instead of network analyzer. Note that the bias “T” is still required to protect the RLC meter from high DC voltages, and the value of protection capacitance needs to be considered while measuring the capacitance of the CMUT. When the DC bias voltage is increased, the CMUT capacitance would increase due to increasing transduction efficiency. As soon as the electrostatic force overwhelms and surpasses the spring force, the membrane collapses to the substrate and CMUT capacitance would dramatically change. At this point, the observed DC voltage is the pull-in voltage [62],[63]. Note that FLUKE® PM6303 Automatic RCL Meter (Fluke Everett, WA, U.S.A) was used to perform the measurement.

Another approach to measure the pull-in voltage and the series resistance is to perform I-V characterization. This approach is an effective way to obtain the electric breakdown of the insulation layer for the CMUT structures that their electrodes do not contact at collapse voltage; however, this approach is particularly useful in determining the pull-in voltage and resistance of the CMUT structures that use no insulation between the top and bottom electrodes. The reason is with no insulation, the CMUT experiences a short-circuit at pull-in and a sudden increase in current indicates reaching the pull-in voltage. The CMUT is connected to an increasing current generator and the voltage is measured. The current and voltage information are stored and plotted in MATLAB software. Initially, no resistance should be observed (i.e. the I-V curve is a horizontal line) since the electrodes are apart. At collapse voltage, the electrodes will be in contact and the plot would show a sudden increase in current (i.e. the I-V would show a positive sloped line). The slope of the plot represents the resistance of the CMUT cell. To generate the current and measure the voltage, Keithly 2602 Source-Meter® System (Keithley Instruments Inc., Ohio, U.S.A.) was used. The source-meter is connected to a PC for acquiring data and plotting voltage and current data.

5.1.2 Mechanical Testing Setup

The mechanical characterization would enable one to measure the resonant frequency, the displacement and the profile of a CMUT membrane under various bias voltages. To measure the resonant frequency and membrane displacement of CMUT cells, a fiber vibrometer OFV-551 (Polytec GmbH, Waldbrunn, Germany) was used which is based on the idea of the Mach-Zehnder interferometer. The vibrometer is attached to a Micro System Analyzer MSA-500

(Polytec) and a vibrometer controller OFV-500 (Polytec) that can detect frequencies up to 20MHz. The Micro System Analyzer contains a junction box MSA-E-500 (Polytech) and a measurement microscope MSA-I-500 (Polytec) to observe the Device Under Test (DUT). The entire system is connected to a PC through the fiber vibrometer to perform digital analysis. Figure 38 shows the complete experimental setup to characterize the mechanical properties of the CMUT cell.

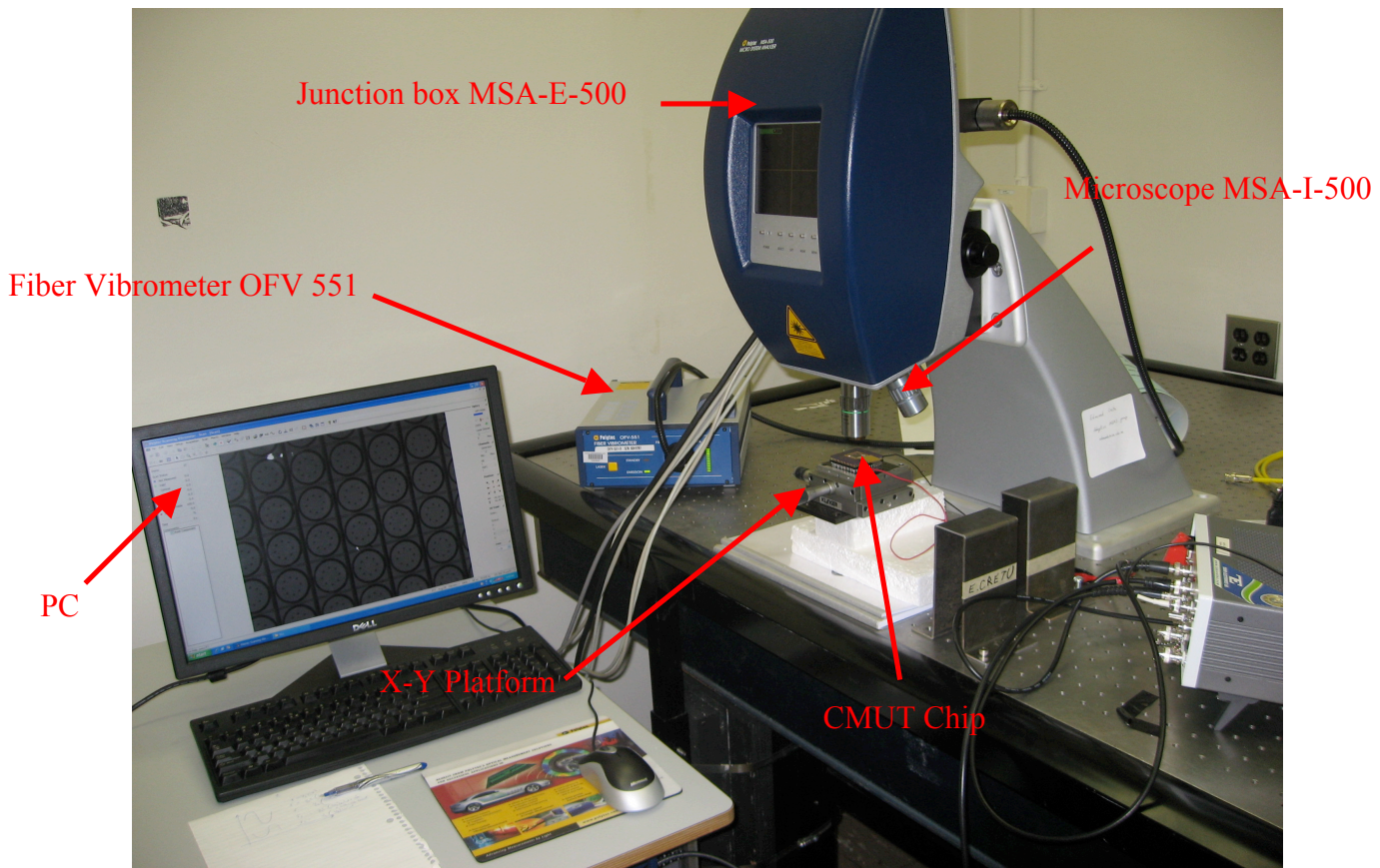


Figure 35. Complete experimental setup to mechanically characterize a CMUT cell

The Micro System Analyzer does not provide large DC voltages to the MEMS device. Therefore, an external power supply needs to be added if one wishes to DC bias the CMUTs with high

voltages. Once again, a bias “T” is required to be installed, as was shown in figure 37, prior to performing any experiment to avoid damaging the setup equipment.

5.1.3 Acoustical Testing Setup

To fully characterize the CMUT for different applications, some of its key characteristics need to be determined such as output pressure and receive sensitivity. These are the two important characteristics, which determine the penetration depth in ultrasound applications. Since in many applications, such as ultrasound imaging, the CMUT is operated in contact with tissue or in immersion, the tests are required to be done in immersion.

To measure the output pressure, CMUT is immersed into an oil tank (e.g. soybean oil) at one end and a high frequency hydrophone at the other end. The CMUT is biased with a DC power supply and excited by a function generator in electrical domain. The generated ultrasound wave from the membrane propagates in the oil medium and is detected by the hydrophone. Note that the bias “T” needs to be embedded into the system to protect the function generator from high DC voltages.

To observe the transmit/receive behavior of CMUTs, pulse-echo measurement is used. The CMUT is immersed into the oil tank and DC biased using a high voltage power supply. It is then connected to a DC bias network (i.e. bias “T”) to protect the low voltage equipment. The network is connected to a function generator, which would excite a broadband electric pulse. At the other end of the tank, a plane reflector (e.g. an Aluminum block) is positioned perpendicular to the direction of ultrasound wave propagation. The excited pulse is reflected from the plane reflector and vibrates the CMUT membrane when it comes in contact with the CMUT. The

vibration of the membrane changes the capacitance and thus the voltage across the CMUT. The generated electric signal is amplified and readout by an oscilloscope. The Fourier Transform of the received signal would show the band shape. The pulse-echo measurement setup is shown in figure 39.

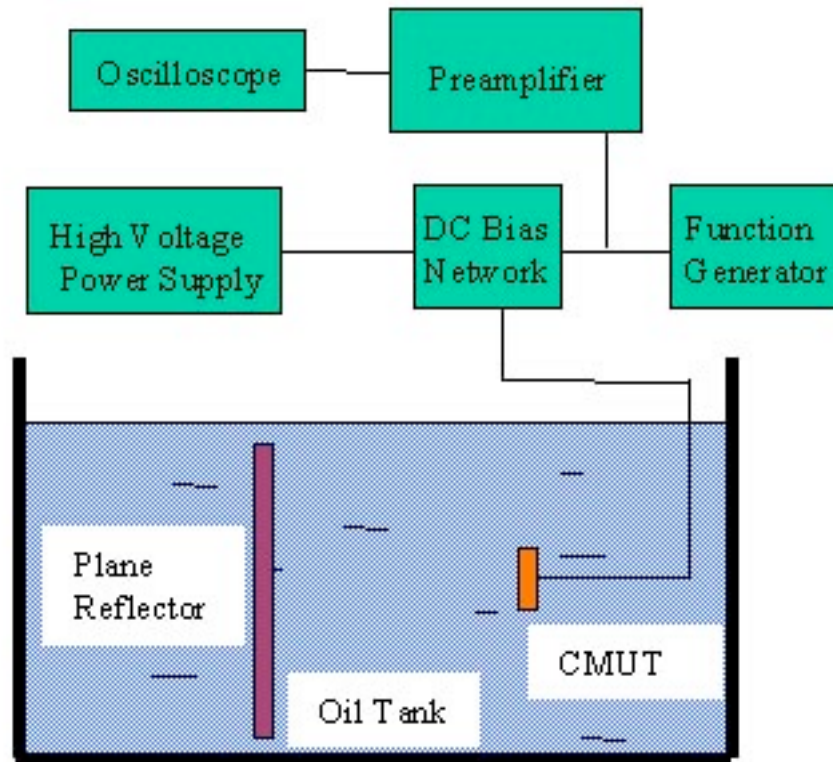


Figure 36. Experimental setup for pulse-echo measurement [64]

Note that in both output pressure and pulse-echo experiments, medium attenuation and diffraction are required to be taken into consideration for accurate measurement results.

5.2 Experimental Results

The fabricated CMUT dies were received and tested. Unfortunately, the experimental results were not as expected. The reason was due to mal-fabrication of the CMUTs. One reason, which was experimentally proved, was that the insulation layer (i.e. nitride) was not deposited. To experimentally determine the faultiness, CMUT cells were undergone I-V characterizations. Figure 40 shows the I-V curve of the CMUT cell, which uses substrate as the bottom electrode and the membrane as the top electrode. The current was limited to 100mA and the voltage was readout. Note that due to the substrate being insulated from the membrane, the top and the bottom electrodes should not be in contact and the relationship between the voltage and the current should not be linear; however, we clearly observe a short-circuit.

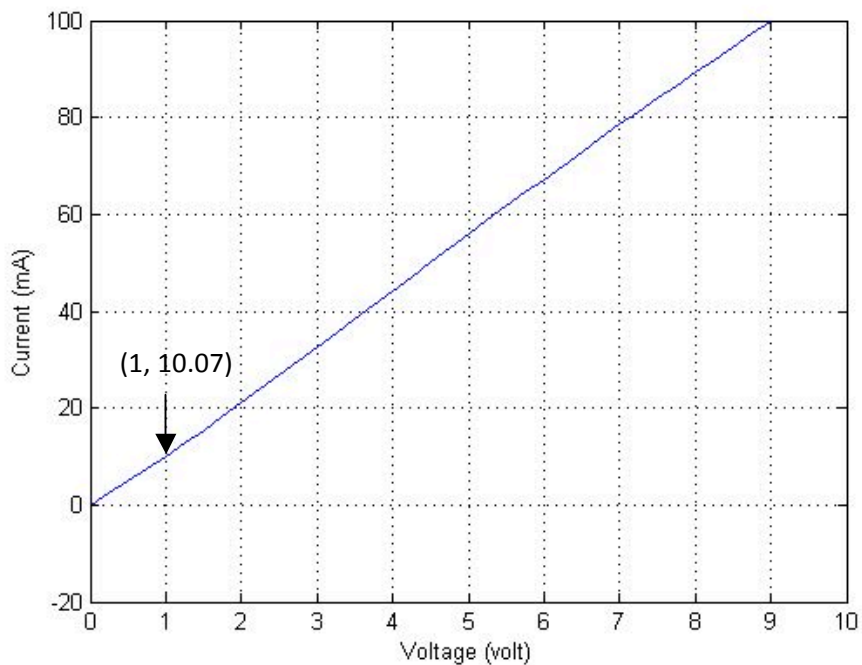


Figure 37. I-V curve of the CMUT cell structure with nitride insulation

The resistance of this short-circuit is found by calculating the slope of the plot and is

$$\frac{1V}{10.07mA} = 99.30\Omega.$$

The resistance value was also measured using a precise RLC meter and the obtained value was 104.5Ω , which is very close to the value calculated from the plot.

The second CMUT structure, which uses poly-silicon as the bottom electrode and the membrane as the top electrode, was also tested. Although, this CMUT structure did not use an insulation layer between electrodes, a short-circuit was observed much before the pull-in voltage was reached. The I-V curve of a CMUT of this kind is shown in figure 41.

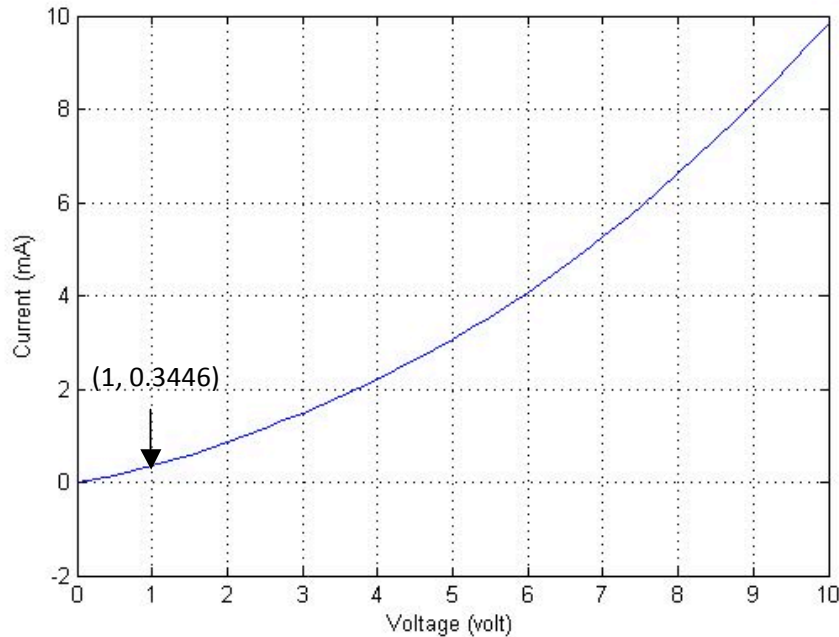


Figure 38. I-V curve of the CMUT cell structure without Nitride insulation

It is observed from the plot that a short-circuit has occurred. The relationship between the voltage and the current is not perfectly linear. Generally, the resistances of materials increase as their temperature increase; However, poly-Silicon in this case behaves differently and as the temperature rises, the resistance decreases. The increase in temperature is due to the increasing

current. At 1V, the current is 0.3446mA and thus the resistance is 2.9019 k Ω . This value is close to the measure value with RLC meter 2.389k Ω , which validates that the impedance is purely resistive. Note that to perform this measurement high currents were used and lead to sacrificing a few CMUT cells.

Another reason a short-circuit occurred, especially in the second kind of CMUT, was because the membrane had collapsed on the substrate during the fabrication process. To verify this mal-fabrication, the profile of the CMUT cell was observed using the Wyko NT1100 Optical Profiling System (Veeco, Tucson, AZ, USA). This equipment optically measures the topology of a sample in sub-nanometer resolution. Figure 42 illustrates the X profile of a CMUT cell. Note that the red horizontal line on the CMUT cell is the cross-sectional cutting line.

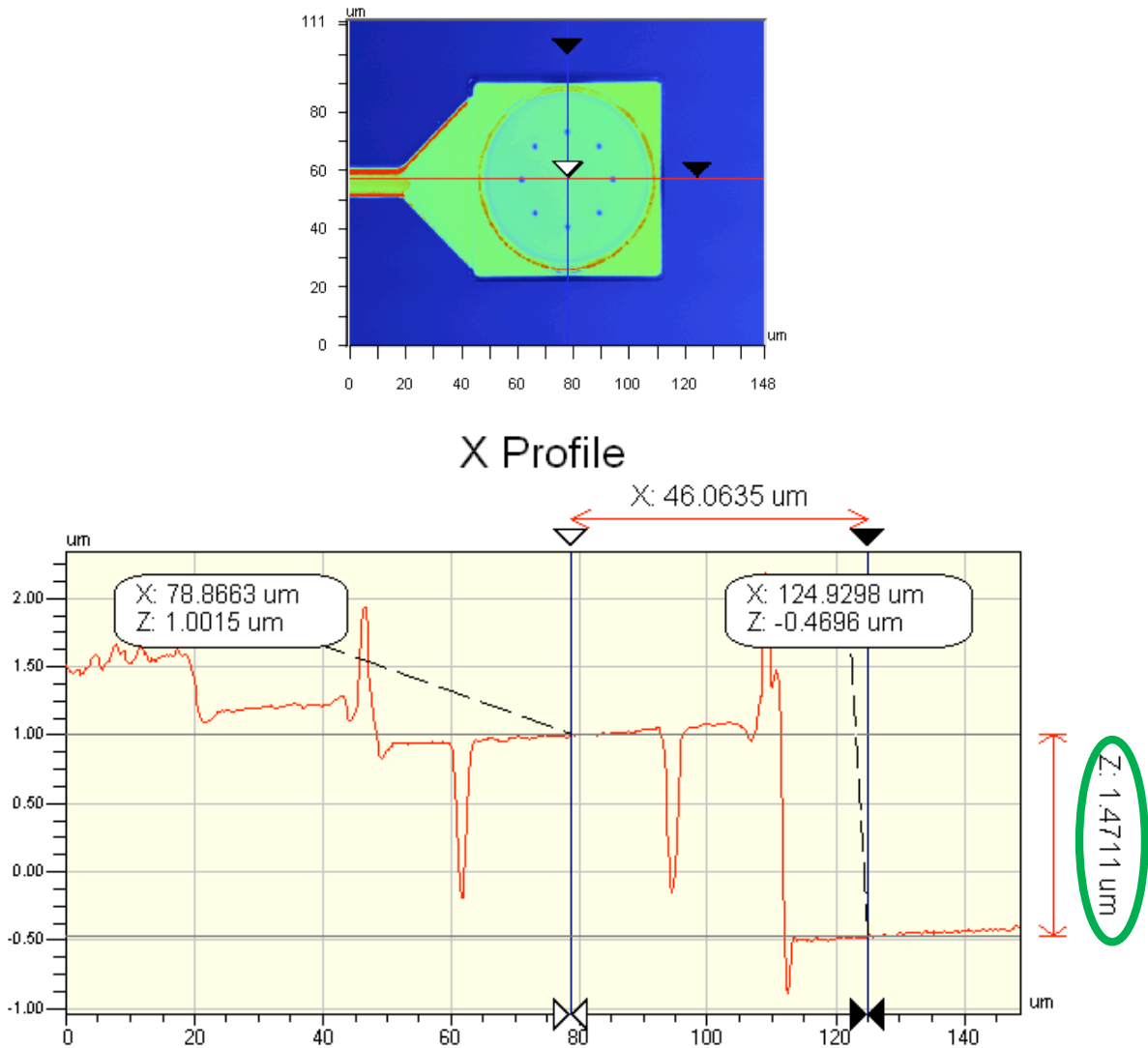


Figure 39. The X profile of a CMUT cell with insulation between the electrodes

As one can see, the membrane has collapsed and the substrate-to-membrane distance is about 1.5-micron (indicated by green oval). Observe that the peaks around the rim of the membrane are about $2\mu\text{m}$ (i.e. combination of Poly0 and Poly2) and that substrate-to-membrane distance indicates the thickness of the Poly2 layer only; thus, the conclusion can be drawn that there exists no oxide layer (i.e. thickness of $0.75\mu\text{m}$) and the membrane has simply collapsed on the substrate. Similar results were obtained for other CMUT structures on all the chips.

The mechanical and acoustical properties of CMUTs did not show any significant results to be addressed due to lack of movement of the membranes.

Chapter 6

Conclusions and Future Work

The capacitive micromachined ultrasound transducer is a relatively new transducer technology that has emerged from MEMS research community. CMUT element is made up from CMUT cells. A CMUT cell consists of a membrane suspended above a substrate. By applying an AC voltage on a fix DC bias voltage between the electrodes on the membrane and in the substrate, the membrane is perturbed and generates ultrasound waves. Conversely, incoming ultrasound pressure waves actuate the CMUT membrane causing a change in the device capacitance and the perturbation is readout electronically. Due to advantages such as electronics integration, high frequency, wide bandwidth, high sensitivity, ease of fabrication, low cost, and CMOS compatibility, CMUTs are thought to be a viable substitute to piezoelectric materials.

A thorough design and simulation of the CMUT behavior was performed. CMUT cell was linearly modeled and its static behavior was simulated in MATLAB software. To observe the inherent non-linear property of CMUT, it was simulated in COMSOL Multiphysics© FEM software. A novel approach was introduced to model the behavior of CMUT using VHDL-AMS. The CMUT was design and fabricated using PolyMUMPs technology.

In this work, CMUT geometries and parameters are designed to be used in medical ultrasound imaging, and were acquired considering that the fabrication would be performed using PolyMUMPs technology. The CMUTs are designed to generate ultrasound waves with a frequency of about 6 MHz, the frequency of which enables detection of breast tumors. Low pull-

in voltage is another requirement that was to be achieved. Other in-house fabrication approaches were also introduced.

Throughout the course of this research, analytical, behavioral and finite element modelings were developed. An analytical modeling was developed based on a moveable plate capacitor attached to a mass-spring-damper system. The model was programmed in MATLAB and results were obtained. The analytical frequency was **5.851MHz** and the pull-in voltage was **202.3V**. As an intermediate step between the analytical and finite element analyses, a behavioral model was developed. Unlike the analytical model, the behavioral model preserves the non-linearity of the CMUT's electro-mechanical interactions. It is also more time efficient than FEM analysis. The behavioral modeling was performed in VHDL-AMS using the Simplorer software. The obtained behavioral resonant frequency was **5.78MHz** and the pull-in voltage was **230V**. The pull-in occurred when the membrane deflected **0.265 μ m**.

A finite element analysis was developed to accurately measure the pull-in voltage, resonant frequency, capacitance, and spring constant. These values were compared to behavioral and analytical modelings. The FEM analysis was done in COMSOL Multiphysics® software coupling *electrostatics*, *structural mechanics* and *moving mesh* domains. The CMUT resonated at **5.85MHz** and the pull-in voltage was simulated to be **275V** at a membrane deflection of **0.315 μ m**. Excellent agreement was shown between behavioral and FEM models.

The CMUTs were fabricated with PolyMUMPs technology in cell and array (i.e. 128 by 118 cells) forms. Two distinct structures were fabricated on the same chip. The first structure uses the substrate as the bottom electrode and a poly-silicon layer (i.e. Poly2) as the membrane and top electrode. The second structure uses a poly-silicon layer (i.e. Poly0) as the bottom electrode and another poly-silicon layer (i.e. Poly2) as the membrane and top electrode. In both cases, the

cavity was made by depositing a layer of silicon-dioxide (i.e. oxide₂) and etching it away at the end of the fabrication process. The second CMUT structure also enabled us to fabricate multiple bottom electrodes, which would control the directionality of acoustic waves at electrical level. The CMUT dies were packaged using PGA 209.

The experimental setup for electrical, mechanical and acoustical domains were presented in detail. Unfortunately, the CMUTs were mal-fabricated by MEMSCAP company and short-circuits were observed in all the chips. The reason was lack of depositing the nitride insulation layer and collapse of the membrane during the fabrication process. The defectiveness of the chips was proved experimentally.

6.1 The Road Ahead

The CMUT is yet at its early stages and requires many improvements. The analytical design and behavioral modeling need to incorporate a better membrane shape modeling and eliminate the piston assumption. Time dependent finite element analysis is of crucial importance to observe the dynamic behavior of CMUT cells. The finite element analysis was only performed on a CMUT cell; however, analysis in array form would present a more profound insight in acoustic domain. The acoustic domain needs to be improved in all three analyses.

Fabrication in PolyMUMPs must be done once more to obtain a working structure and to be able to perform experimental tests.

To operate the CMUT electronically in array form it requires to be coupled with a CMOS layer. The CMOS layer was sent for fabrication and once received, needs to be attached to CMUTs using flip-chip bonding technique. Furthermore, to be able to embed the transducer in an

ultrasound machine, an intermediate circuitry should be used to match the CMUT and ultrasound machine in terms of power and other important parameters.

References

- [1] W.D. O'Brien Jr., "Assessing the Risks for Modern Diagnostic Ultrasound Imaging," *Japanese Journal of Applied Physics*, vol. 37, 1998, pp. 2781-2788.
- [2] F.V. Hunt, *Electroacoustics;: The analysis of transduction, and its historical background*, Harvard University Press, 1954.
- [3] F.V. Hunt, *Origins in Acoustics: The Science of Sound from Antiquity to the Age of Newton*, Yale University Press, 1978.
- [4] W.A. Smith, "Role of piezocomposites in ultrasonic transducers," *IEEE 1989 Ultrasonics Symposium, October 3, 1989 - October 6, 1989*, Montreal, Que, Can: Publ by IEEE, 1989, pp. 755-766.
- [5] K. Suzuki, K. Higuchi, and H. Tanigawa, "A silicon electrostatic ultrasonic transducer," *IEEE Transactions on Ultrasonics, Ferroelectrics and Frequency Control*, vol. 36, Nov. 1989, pp. 620-627.
- [6] D. Hohm, "A subminiature condenser microphone with silicon nitride membrane and silicon back plate," *The Journal of the Acoustical Society of America*, vol. 85, 1989, p. 476.
- [7] M.I. Haller and B.T. Khuri-Yakub, "Surface micromachined electrostatic ultrasonic air transducer," *Proceedings of the 1994 IEEE Ultrasonics Symposium. Part 1 (of 3), November 1, 1994 - November 4, 1994*, Cannes, Fr: IEEE, 1994, pp. 1241-1244.
- [8] D. Hutchins and D. Schindel, "Advances in non-contact and air-coupled transducers," *Proceedings of the 1994 IEEE Ultrasonics Symposium. Part 1 (of 3), November 1, 1994 - November 4, 1994*, Cannes, Fr: IEEE, 1994, pp. 1245-1254.
- [9] P. Eccardt, K. Niederer, T. Scheiter, and C. Hierold, "Surface micromachined ultrasound transducers in CMOS technology," *Proceedings of the 1996 IEEE Ultrasonics Symposium. Part 2 (of 2), November 3, 1996 - November 6, 1996*, San Antonio, TX, USA: IEEE, 1996, pp. 959-962.
- [10] B. Khuri-Yakub, F. Degertekin, X. Jin, S. Calmes, I. Ladabaum, S. Hansen, and X. Zhang, "Silicon micromachined ultrasonic transducers," *Proceedings of the IEEE Ultrasonics Symposium*, vol. 2, 1998, pp. 985-991.
- [11] K. Niederer and B. Fischer, "Micromachined transducers for ultrasound applications," *Proceedings of the 1997 IEEE Ultrasonics Symposium. Part 1 (of 2), October 5, 1997 - October 8, 1997*, Toronto, Can: IEEE, 1997, pp. 1609-1618.
- [12] C.H. Cheng, E.M. Chow, X. Jin, S. Ergun, and B.T. Khuri-Yakub, "An efficient electrical addressing method using through-wafer vias for two-dimensional ultrasonic arrays," *2000 IEEE Ultrasonics Symposium, October 22, 2000 - October 25, 2000*, San Juan, Puerto rico: Institute of

Electrical and Electronics Engineers Inc., 2000, pp. 1179-1182.

- [13] I. Wygant, X. Zhuang, D. Yeh, A. Nikoozadeh, O. Oralkan, A. Ergun, M. Karaman, and B. Khuri-Yakub, "Integrated ultrasonic imaging systems based on CMUT arrays: Recent progress," *2004 IEEE Ultrasonics Symposium, August 23, 2004 - August 27, 2004*, Montreal, Que., Canada: Institute of Electrical and Electronics Engineers Inc., 2004, pp. 391-394.
- [14] A. Caronti, G. Caliano, R. Carotenuto, A. Savoia, M. Pappalardo, E. Cianci, and V. Foglietti, "Capacitive micromachined ultrasonic transducer (CMUT) arrays for medical imaging," *Microelectronics Journal*, vol. 37, Aug. 2006, pp. 770-777.
- [15] S. Frew, H. Najar, and E. Cretu, "VHDL-AMS behavioural modelling of a CMUT element," *BMAS 2009 - 2009 IEEE International Behavioral Modeling and Simulation Workshop, September 17, 2009 - September 18, 2009*, San Jose, CA, United states: IEEE Computer Society, 2009, pp. 19-24.
- [16] A.S. Ergun, G.G. Yaralioglu, O. Oralkan, and B.T. Khuri-Yakub, "MEMS/NEMS Techniques and Applications," *MEMS/NEMS*, 2006, pp. 553-615.
- [17] J.A. Hossack, P. Mauchamp, and L. Ratsimandresy, "A high bandwidth transducer optimized for harmonic imaging," *2000 IEEE Ultrasonics Symposium, October 22, 2000 - October 25, 2000*, San Juan, Puerto rico: Institute of Electrical and Electronics Engineers Inc., 2000, pp. 1021-1024.
- [18] M.A. Averkiou, D.N. Roundhill, and J.E. Powers, "New imaging technique based on the nonlinear properties of tissues," *Proceedings of the 1997 IEEE Ultrasonics Symposium. Part 1 (of 2), October 5, 1997 - October 8, 1997*, Toronto, Can: IEEE, 1997, pp. 1561-1566.
- [19] U. Demirci, A.S. Ergun, O. Oralkan, M. Karaman, and B.T. Khuri-Yakub, "Forward-viewing CMUT arrays for medical imaging," *IEEE Transactions on Ultrasonics, Ferroelectrics, and Frequency Control*, vol. 51, 2004, pp. 887-895.
- [20] O. Oralkan, S.T. Hansen, B. Bayram, G.G. Yaralioglu, A.S. Ergun, and B.T. Khuri-Yakub, "CMUT ring arrays for forward-looking intravascular imaging," *2004 IEEE Ultrasonics Symposium, August 23, 2004 - August 27, 2004*, Montreal, Que., Canada: Institute of Electrical and Electronics Engineers Inc., 2004, pp. 403-406.
- [21] D.T. Yeh, O. Oralkan, A.S. Ergun, X. Zhuang, I.O. Wygant, and B.T. Khuri-Yakub, "High-frequency CMUT arrays for high-resolution medical imaging," *Medical Imaging 2005 - Ultrasonic Imaging and Signal Processing, February 15, 2005 - February 17, 2005*, San Diego, CA, United states: SPIE, 2005, pp. 87-98.
- [22] S.W. Smith, W. Lee, E.D. Light, J.T. Yen, P. Wolf, and S. Idriss, "Two dimensional arrays for 3-D ultrasound imaging," *2002 IEEE Ultrasonics Symposium, October 8, 2002 - October 11, 2002*, Munich, Germany: Institute of Electrical and Electronics Engineers Inc., 2002, pp. 1545-1553.
- [23] S. Vaithilingam, I.O. Wygant, P.S. Kuo, X. Zhuang, O. Oralkan, P.D. Olcott, and B.T. Khuri-Yakub, "Capacitive micromachined ultrasonic transducers (CMUTs) for photoacoustic imaging," *Photons Plus Ultrasound: Imaging and Sensing 2006: The Seventh Conference on Biomedical Thermoacoustics, Optoacoustics, and Acousto-optics*, A.A. Oraevsky and L.V. Wang, Eds., San

- Jose, CA, USA: SPIE, 2006, pp. 608603-11.
- [24] D. Christensen, *Ultrasonic Bioinstrumentation*, Wiley, 1988.
- [25] T. Hsu, *MEMS & Microsystems: Design, Manufacture, and Nanoscale Engineering*, Wiley, 2008.
- [26] I. Ladabaum, X. Jin, H.T. Soh, A. Atalar, and B.T. Khuri-Yakub, "Surface micromachined capacitive ultrasonic transducers," *IEEE Transactions on Ultrasonics, Ferroelectrics, and Frequency Control*, vol. 45, 1998, pp. 678-690.
- [27] R. Guldiken, "Dual-electrode capacitive micromachined ultrasonic transducers for medical ultrasound applications," Georgia Institute of Technology, 2009.
- [28] J. Liu, C. Oakley, and R. Shandas, "Capacitive micromachined ultrasonic transducers using commercial multi-user MUMPs process: Capability and limitations," *Ultrasonics*, vol. 49, 2009, pp. 765-773.
- [29] N. Nguyen and S. Wereley, *Fundamentals and Applications of Microfluidics*, Artech House Publishers, 2002.
- [30] E. Cretu, J.H. Huijsing, and D.U.O.T. TU Delft, "Inertial MEMS Devices: Modeling, design and applications."
- [31] W. Soedel, *Vibrations of Shells and Plates, Third Edition*, CRC Press, 2004.
- [32] G.G. Yaralioglu, A.S. Ergun, B. Bayram, E. Hggstrom, and B.T. Khuri-Yakub, "Calculation and measurement of electromechanical coupling coefficient of capacitive micromachined ultrasonic transducers," *IEEE Transactions on Ultrasonics, Ferroelectrics, and Frequency Control*, vol. 50, 2003, pp. 449-456.
- [33] J.D. Fraser and P. Reynolds, "Finite-element method for determination of electromechanical coupling coefficient for piezoelectric and capacitive micromachined ultrasonic transducers," Nov. 2000.
- [34] A.S. Ergun, G.G. Yaralioglu, and B.T. Khuri-Yakub, "Capacitive micromachined ultrasonic transducers: Theory and technology," *Journal of Aerospace Engineering*, vol. 16, 2003, pp. 76-84.
- [35] E. Cianci, V. Foglietti, A. Minotti, A. Caronti, G. Caliano, and M. Pappalardo, "Fabrication Techniques in Micromachined Capacitive Ultrasonic Transducers and their Applications," *MEMS/NEMS*, 2006, pp. 353-382.
- [36] C. Bayram, S. Olcum, M.N. Senlik, and A. Atalar, "Bandwidth improvement in a cMUT array with mixed sized elements," *2005 IEEE Ultrasonics Symposium, September 18, 2005 - September 21, 2005*, Rotterdam, Netherlands: Institute of Electrical and Electronics Engineers Inc., 2005, pp. 1956-1959.
- [37] C.B. Doody, R.D. White, J.S. Wadhwa, and D.F. Lemmerhirt, "Characterization and modeling of capacitive micromachined ultrasonic transducers for diagnostic ultrasound," *2008 ASME International Mechanical Engineering Congress and Exposition, IMECE 2008, October 31, 2008 -*

November 6, 2008, Boston, MA, United states: American Society of Mechanical Engineers, 2009, pp. 287-294.

- [38] W.P. Mason, *Electromechanical transducers and wave filters*, D. Van Nostrand Co, 1948.
- [39] B. Bayram, E. Hggstrom, G.G. Yaralioglu, and B.T. Khuri-Yakub, "A new regime for operating capacitive micromachined ultrasonic transducers," *IEEE Transactions on Ultrasonics, Ferroelectrics, and Frequency Control*, vol. 50, 2003, pp. 1184-1190.
- [40] G.G. Yaralioglu, A.S. Ergun, B. Bayram, E. Hggstrom, and B.T. Khuri-Yakub, "Calculation and measurement of electromechanical coupling coefficient of capacitive micromachined ultrasonic transducers," *IEEE Transactions on Ultrasonics, Ferroelectrics, and Frequency Control*, vol. 50, 2003, pp. 449-456.
- [41] B. Bayram, G.G. Yaralioglu, A.S. Ergun, and B. Khuri-Yakub, "Influence of the electrode size and location on the performance of a CMUT," *2001 Ultrasonics Symposium, October 6, 2001 - October 10, 2001*, Atlanta, GA, United states: Institute of Electrical and Electronics Engineers Inc., 2001, pp. 949-952.
- [42] A. Bozkurt, I. Ladabaum, A. Atalar, and B.T. Khuri-Yakub, "Theory and analysis of electrode size optimization for capacitive microfabricated ultrasonic transducers," *IEEE Transactions on Ultrasonics, Ferroelectrics, and Frequency Control*, vol. 46, 1999, pp. 1364-1374.
- [43] G.G. Yaralioglu, B. Bayram, A. Nikoozadeh, and B.T.P. Khuri-Yakub, "Finite element modeling of capacitive micromachined ultrasonic transducers," *Medical Imaging 2005 - Ultrasonic Imaging and Signal Processing, February 15, 2005 - February 17, 2005*, San Diego, CA, United states: SPIE, 2005, pp. 77-86.
- [44] G.G. Yaralioglu, M.H. Badi, A.S. Ergun, and B.T. Khuri-Yakub, "Improved equivalent circuit and finite element method modeling of capacitive micromachined ultrasonic transducers," *2003 IEEE Ultrasonics Symposium - Proceedings, October 5, 2003 - October 8, 2003*, Honolulu, HI, United states: Institute of Electrical and Electronics Engineers Inc., 2003, pp. 469-472.
- [45] Y. Roh and B.T. Khuri-Yakub, "Finite element analysis of underwater capacitor micromachined ultrasonic transducers," *IEEE Transactions on Ultrasonics, Ferroelectrics, and Frequency Control*, vol. 49, 2002, pp. 293-298.
- [46] S. Ballandras, A. Caronti, W. Steichen, M. Wilm, V. Iaude, T. Pastureaud, R. Lardat, and W. Daniau, "Simulation of cMUT radiating in water using a mixed finite element/boundary element approach," *2002 IEEE Ultrasonics Symposium, October 8, 2002 - October 11, 2002*, Munich, Germany: Institute of Electrical and Electronics Engineers Inc., 2002, pp. 1075-1078.
- [47] M. Kaltenbacher, H. Landes, K. Niederer, and R. Lerch, "3D simulation of controlled micromachined capacitive ultrasound transducers," *1999 IEEE Ultrasonics Symposium, October 17, 1999 - October 20, 1999*, Caesars Tahoe, NV, USA: IEEE, 1999, pp. 1155-1158.
- [48] M. Kaltenbacher, *Numerical Simulation of Mechatronic Sensors and Actuators*, Springer, 2004.

- [49] S.A. Anbalagan, G. Uma, and M. Umapathy, "Modeling and simulation of Capacitive Micromachined Ultrasonic Transducer (CMUT)," *Journal of Physics: Conference Series*, vol. 34, 2006, pp. 595-600.
- [50] R.K. Gupta, "Electrostatic pull-in test structure design for in situ mechanical property measurements of microelectromechanical systems (MEMS)," Massachusetts Institute of Technology, 1997.
- [51] B. Bayram, E. Haeggstrom, A.S. Ergun, G.G. Yaralioglu, and B.T. Khuri-Yakub, "Dynamic analysis of CMUTs in different regimes of operation," *2003 IEEE Ultrasonics Symposium - Proceedings, October 5, 2003 - October 8, 2003*, Honolulu, HI, United states: Institute of Electrical and Electronics Engineers Inc., 2003, pp. 481-484.
- [52] A. Nikoozadeh, B. Bayram, G.G. Yaralioglu, and B.T. Khuri-Yakub, "Analytical calculation of collapse voltage of CMUT membrane," *2004 IEEE Ultrasonics Symposium, August 23, 2004 - August 27, 2004*, Montreal, Que., Canada: Institute of Electrical and Electronics Engineers Inc., 2004, pp. 256-259.
- [53] A. Safari and E.K. Akdoğan, *Piezoelectric and Acoustic Materials for Transducer Applications*, 2008.
- [54] X. Zhuang, "Two-dimensional capacitive micromachined ultrasonic transducer (CMUT) arrays for a miniature integrated volumetric ultrasonic imaging system," *Proceedings of SPIE*, San Diego, CA, USA: 2005, pp. 37-46.
- [55] X. Jin, C. Cheng, O. Oralkan, S. Calmes, F. Degertekin, and B. Khur-Yakub, "Recent progress in capacitive micromachined ultrasonic immersion transducer array," *8th International Symposium on Integrated Circuits, Devices and Systems, ISIC 99, September 8, 1999 - September 10, 1999*, Singapore, Singapore: Nanyang Technological University, 1999, pp. 159-162.
- [56] H. Seidel, L. Csepregi, A. Heuberger, and H. Baumgaertel, "Anisotropic etching of crystalline silicon in alkaline solutions. I. Orientation dependence and behavior of passivation layers," *Journal of the Electrochemical Society*, vol. 137, 1990, pp. 3612-3626.
- [57] Y. Huang, A. Sanli Ergun, E. Hggstrom, M.H. Badi, and B. Khuri-Yakub, "Fabricating capacitive micromachined ultrasonic transducers with wafer-bonding technology," *Journal of Microelectromechanical Systems*, vol. 12, 2003, pp. 128-137.
- [58] D.T. Yeh, O. Oralkan, A.S. Ergun, X. Zhuang, I.O. Wygant, and B.T. Khuri-Yakub, "High-frequency CMUT arrays for high-resolution medical imaging," *Medical Imaging 2005 - Ultrasonic Imaging and Signal Processing, February 15, 2005 - February 17, 2005*, San Diego, CA, United states: SPIE, 2005, pp. 87-98.
- [59] Retrieved from World Wide Web on September 2009.
<http://www.memscap.com/mumps/documents/SOIMUMPs.dr.v4.pdf>
- [60] Y. Huang, E. Hggstrom, B. Bayram, X. Zhuang, A. Ergun, C. Cheng, and B. Khuri-Yakub, "Collapsed regime operation of capacitive micromachined ultrasonic transducers based on wafer-bonding technique," *2003 IEEE Ultrasonics Symposium - Proceedings, October 5, 2003 - October*

8, 2003, Honolulu, HI, United states: Institute of Electrical and Electronics Engineers Inc., 2003, pp. 1161-1164.

- [61] Retrieved from World Wide Web on January 2010. http://www-kyg.stanford.edu/khuriyakub/opencms/en/research/characterization/Impedence_Measurement/index.html
- [62] Y. Huang, E. Haeggström, B. Bayram, X. Zhuang, A.S. Ergun, C. Cheng, and B.T. Khuri-Yakub, "Comparison of conventional and collapsed region operation of capacitive micromachined ultrasonic transducers," *IEEE Transactions on Ultrasonics, Ferroelectrics, and Frequency Control*, vol. 53, Oct. 2006, pp. 1918-1933.
- [63] O. Oralkan, B. Bayram, G.G. Yaralioglu, A.S. Ergun, M. Kupnik, D.T. Yeh, I.O. Wygant, and B.T. Khuri-Yakub, "Experimental characterization of collapse-mode CMUT operation," *IEEE Transactions on Ultrasonics, Ferroelectrics, and Frequency Control*, vol. 53, Aug. 2006, pp. 1513-1523.
- [64] Retrieved from World Wide Web on January 2010. <http://www-kyg.stanford.edu/khuriyakub/opencms/en/research/characterization/Pulse-echo/index.html>

Appendices

Appendix A – COMSOL Multiphysics Simulation Setup for Parametric Analysis

This section explains how to setup a CMUT cell in COMSOL Multiphysics to perform parametric analysis. The parameter is input voltage.

Model Navigator

- 1- In the **Model Navigator** select **3D** in the **Space dimension** list, and then click **Multiphysics**.
- 2- From the list of application modes on the left side of the dialog box, select **MEMS Module > Structural Mechanics > Solid, Stress-Strain**. Click Add.
- 3- From the list of application modes, select **COMSOL Multiphysics > Deformed Mesh > Moving Mesh (ALE)** and then click Add.
- 4- In the **Multiphysics** list on the right side of the dialog box, select **Frame (ale)** then add **MEMS Module > Electrostatics > Electrostatics** to that list.
- 5- Click **OK** to close the **Model Navigator**.

Options and Settings

- 1- From the **Draw** menu, select **Work-Plane Settings**.
- 2- Click the **Quick** tab.
- 3- Choose the **x-y plane**, and for **z** use a value of 0.
- 4- Click **OK**.

Geometry Modeling

- 1- From the **Draw** menu, select **Work-Plane Settings**.
- 2- Shift-click the **Ellipse/Circle (Centered)** button on the Draw toolbar to create a circle.
- 3- Put $32e-6$ for **Radius** and for **x** and **y** positions put 0 and 0.
- 4- Click the **Zoom extents** from the Main toolbar at the top.
- 5- While holding down the Shift key, click the **Rectangle/Square** button on the Draw toolbar on the far left side of the graphical user interface; this action opens the **Rectangle** dialog box. Enter dimensions as in the following table, and then click **OK**.

Property	Value
Width	$70e-6$
Height	$35e-6$
X	$-35e-6$
Y	0

Table 5. Rectangle parameters in COMSOL

- 6- Click **Control+A** to select both geometries.
- 7- Click the **intersection** button on the Draw toolbar.
- 8- From the **Draw** menu select **Extrude** to open the extrude option box.
- 9- While **CO1** is selected, type $-0.6e-6$ in the **Distance** box.
- 10- Under **Extrude Object Name** type **Nitride Layer**.
- 11- Change the work plane to **Geom2** from the top tabs.
- 12- Open the **Extrude** box as in step 8 and while **CO1** is selected, type $0.75e-6$ in the **Distance** box.
- 13- In **Extrude Object Name** type **Gap distance**.
- 14- Change the work plane to **Geom2**, again.

- 15- Open the **Extrude** box for the third time as explained in step 8.
- 16- While **CO1** is selected, type $1.5e-6$ in the **Distance**.
- 17- In **Extrude Object Name** type **Membrane**.
- 18- Make sure **Membrane** geometry is selected and click on **Move** button from left toolbar.
- 19- Enter $0.75e-6$ in **Z Displacement**.
- 20- Change the work plane to **Geom2**.
- 21- Shift-click the **Rectangle/Square** button on the Draw toolbar.
- 22- Enter dimension values as in table 5.
- 23- Open the **Extrude** box as in step 8 and ensure **R1** is selected.
- 24- Enter $3.5e-6$ in the **Distance**, and in **Extrude Object Name** type **Medium**.
- 25- While the **Medium** rectangle is selected, click on **Move** button from left toolbar and enter $-0.6e-6$ in **Z Displacement**.

Physics Settings

Subdomain Settings – Electrostatics

- 1- Go to the **Multiphysics** menu and make sure that **Electrostatics (emes)** is selected.
- 2- Open the **Physics>Subdomain Settings** dialog box.
- 3- Select Subdomain 2 and enter 9.7 for relative permittivity of nitride, ϵ_r .
- 4- Select Subdomain 4 and enter 4.5 for relative permittivity of poly-silicon, ϵ_r .
- 5- Click the **Force** tab. In the first row enter **Fes**. The software automatically generates the variables Fes_nTx_emes and Fes_nTy_emes for the electrostatic force components. Later on you use these variables to define the boundary load in the Plane Strain application mode.
- 6- Click **OK**.

Boundary Conditions – Electrostatics

- 1- From the **Physics** menu, open the **Boundary** Settings dialog box.
- 2- Check the **Interior boundaries** box and then specify conditions as follows:

Settings	Boundaries 1-5, 7, 8, 10, 13, 19	Boundary 14	Boundary 8	Rest of Boundaries
Boundary Condition	Zero charge/Symmetry	Electric Potential	Ground	Continuity
V_0		V_{in}		

Table 6. Boundary settings for electrostatics in COMSOL

- 3- Click **OK**.

Subdomain Settings – Moving Mesh

- 1- From the **Multiphysics** menu, select **Moving Mesh (ale)**.
- 2- In the **Subdomain Settings** dialog box select Subdomain 2 and choose **No displacement** setting.
- 3- Select Subdomain 4 and choose **Physics induced displacement**. For the displacement variables, **dx**, **dy** and **dz**, enter u and v and w , respectively.
- 4- Click **OK**.

Boundary Conditions – Moving Mesh

- 1- In the **Boundary Settings** dialog box for the mesh displacements, enter these settings:

Settings	Boundaries 14, 15	Boundaries 10, 2	All other Boundaries
dx	u	Not selected	0
dy	v	0	0
dz	w	Not selected	0

Table 7. Boundary settings for moving mesh in COMSOL

2- Click **OK**.

Subdomain Settings – Solid, Stress-Strain

- 1- Go to the **Multiphysics** menu and ensure that the **Solid, Stress-Strain (smsld)** application mode is selected
- 2- Open **Subdomain Settings** and select Subdomains 1 and 3 and clear the **Active in this subdomain** check box.
- 3- Fill out the properties of Subdomains 2 and 4 according to the following:

Properties	Values of Subdomain 1	Values of Subdomain 2
E	$160e9$	$250e9$
ν	0.23	0.23
α	$4.15e-6$	$2.3e-6$
ρ	2330	3100

Table 8. Subdomain settings for solid, stress-stain in COMSOL

Boundary Conditions – Solid, Stress-Strain

- 1- Open **Boundary Conditions** and choose all the boundaries. From the **Constraint condition** choose **Fixed**.
- 2- Select Boundaries 13 and 7, and change the **Constraint condition** to **Symmetry Plane**.
- 3- Select Boundaries 14 and 15 and change the **Constraint condition** to **Free**.
- 4- Select Boundary 14 and change to **Load** tab. For F_x , F_y and F_z values enter Fes_nTx_emes , Fes_nTy_emes , and Fes_nTz_emes , respectively.
- 5- Click **OK**.
- 6- To obtain more precise results select, select **Properties** from the **Physics** menu and set the **Large Deformation** property option to **On**.

Mesh Generation

Click the **Initialize Mesh** button on the Main toolbar. The mesh consists of roughly 22061 elements.

Computing the Solution

- 1- Click the **Solver Parameters** button from the Main toolbar; the **Solver Parameters** dialog box then opens.
- 2- In the dialog box, change the **Analysis** to **Parametric** and the **Solver** to **Parametric Segregated**.
- 3- For **Parameter name** enter V_{in} , and for **Parameter values** enter $[5:5:300]$.
- 4- In **Segregated Groups** enter V for Group 1, “ $u\ v\ w$ ” for Group 2 and “ $x\ y\ z\ lm4\ lm5\ lm6$ ” for Group 3.
- 5- Click **OK** to close the dialog box
- 6- Click **Solve** button on the Main toolbar to solve for parametric analysis. It takes about a few hours.

Appendix B – Images of CMUT Masking Layouts, Fabricated Devices, and Pin Configuration

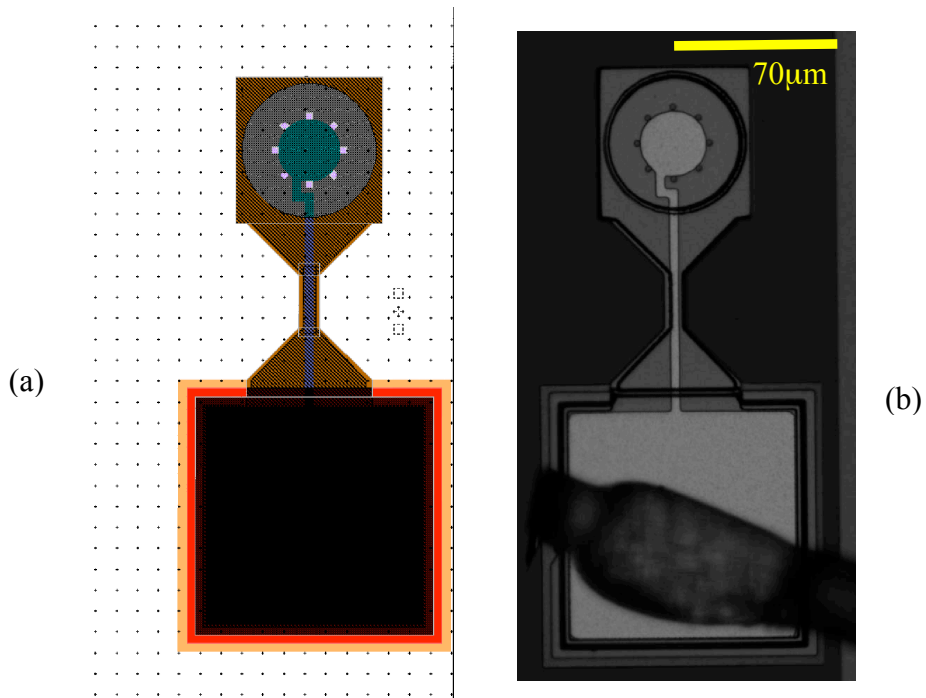


Figure 40. (a) Masking layout and, (b) fabricated device of a CMUT cell with a layer of metal atop and using substrate as the ground electrode

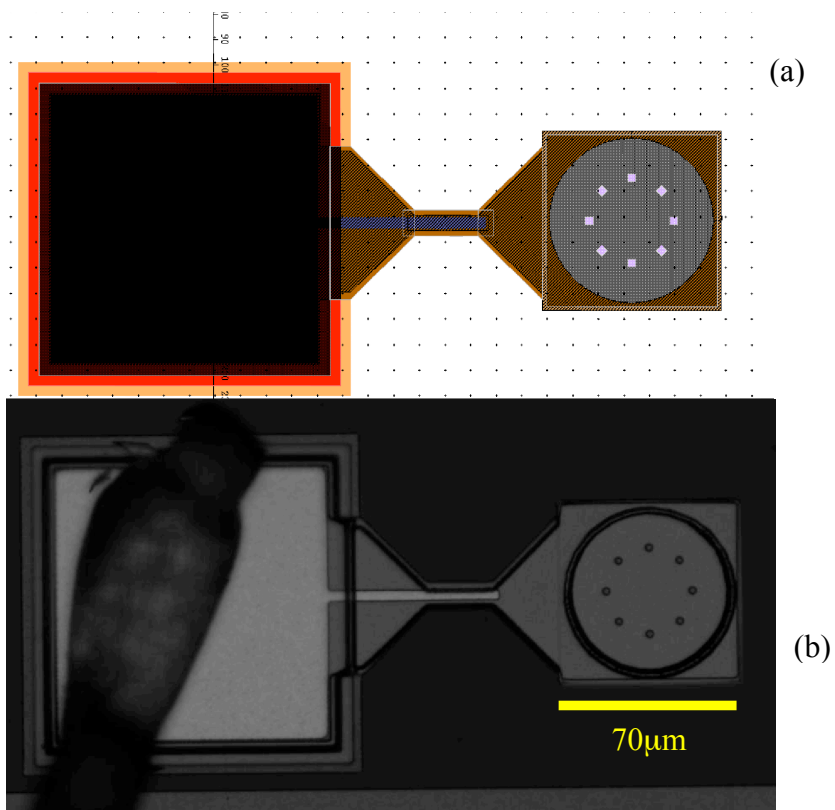


Figure 41. (a) Masking layout and, (b) fabricated device of a CMUT cell structure using the substrate as the ground electrode

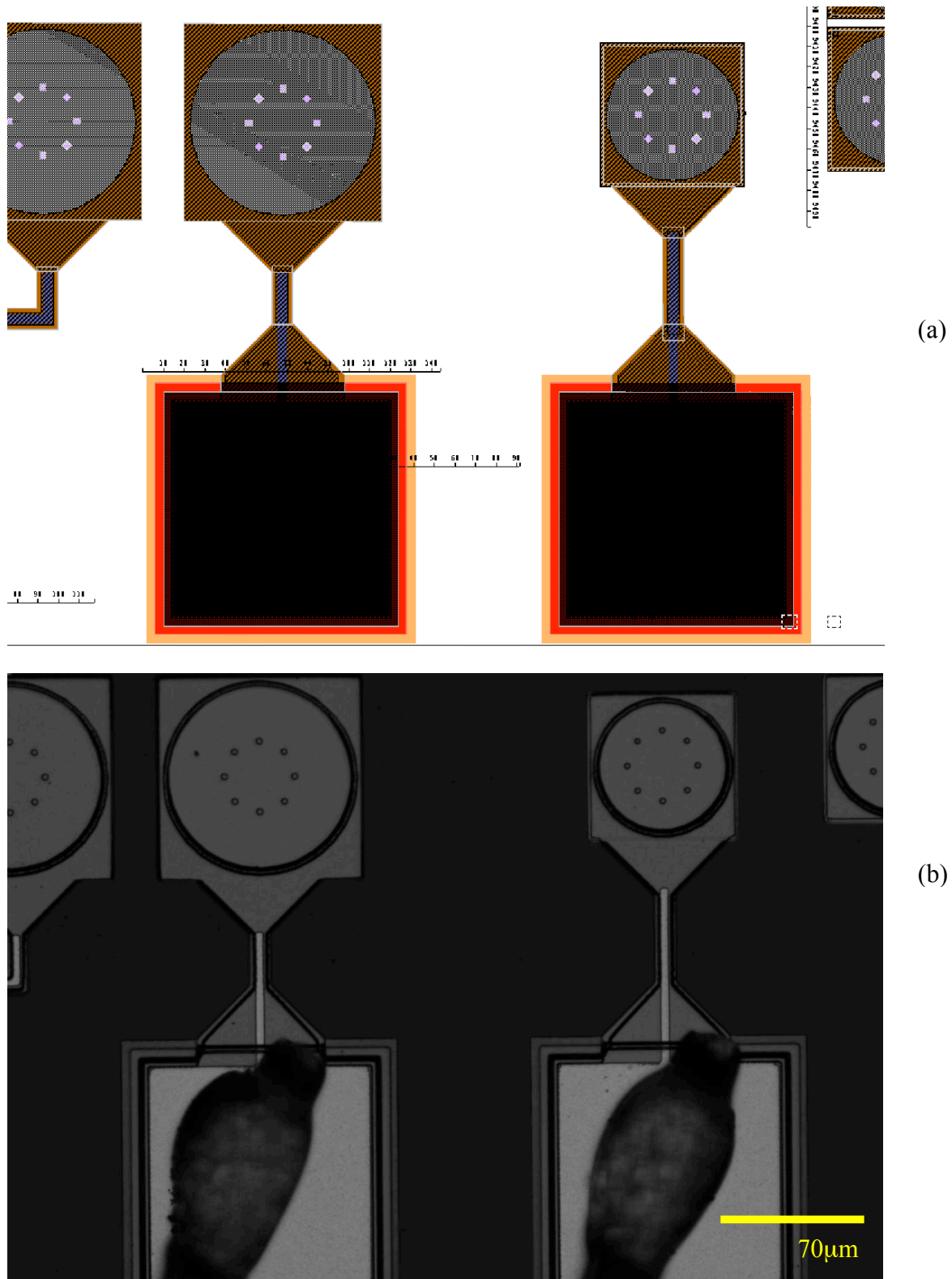


Figure 42. (a) Masking layout and,(b) fabricated device of CMUT cells with different radii and using substrate as the ground electrode

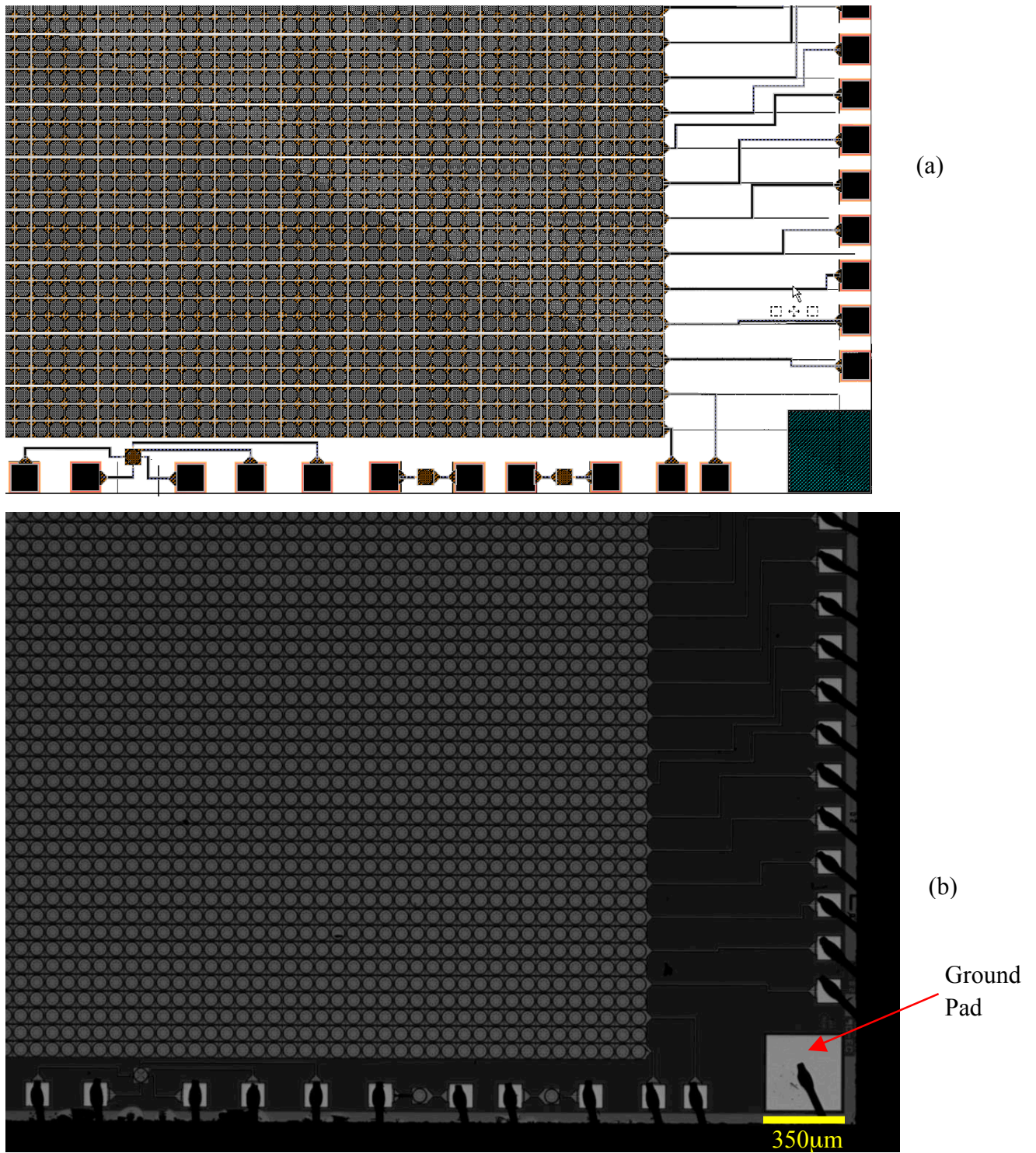


Figure 43. (a) Masking layout and, (b) fabricated device of CMUT arrays and the ground pad

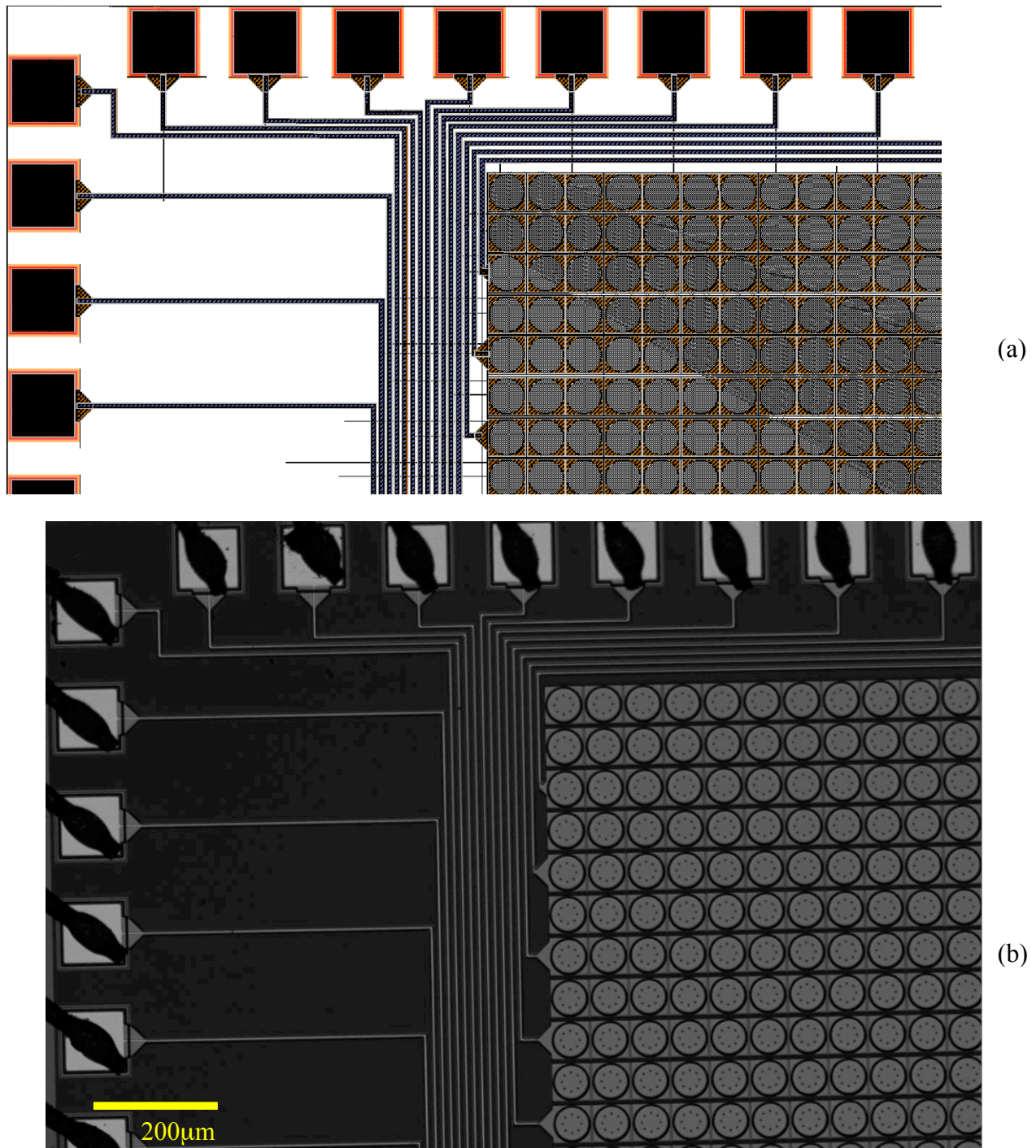


Figure 44. (a) Masking layout and, (b) fabricated device of CMUT arrays and their interconnecting tracks

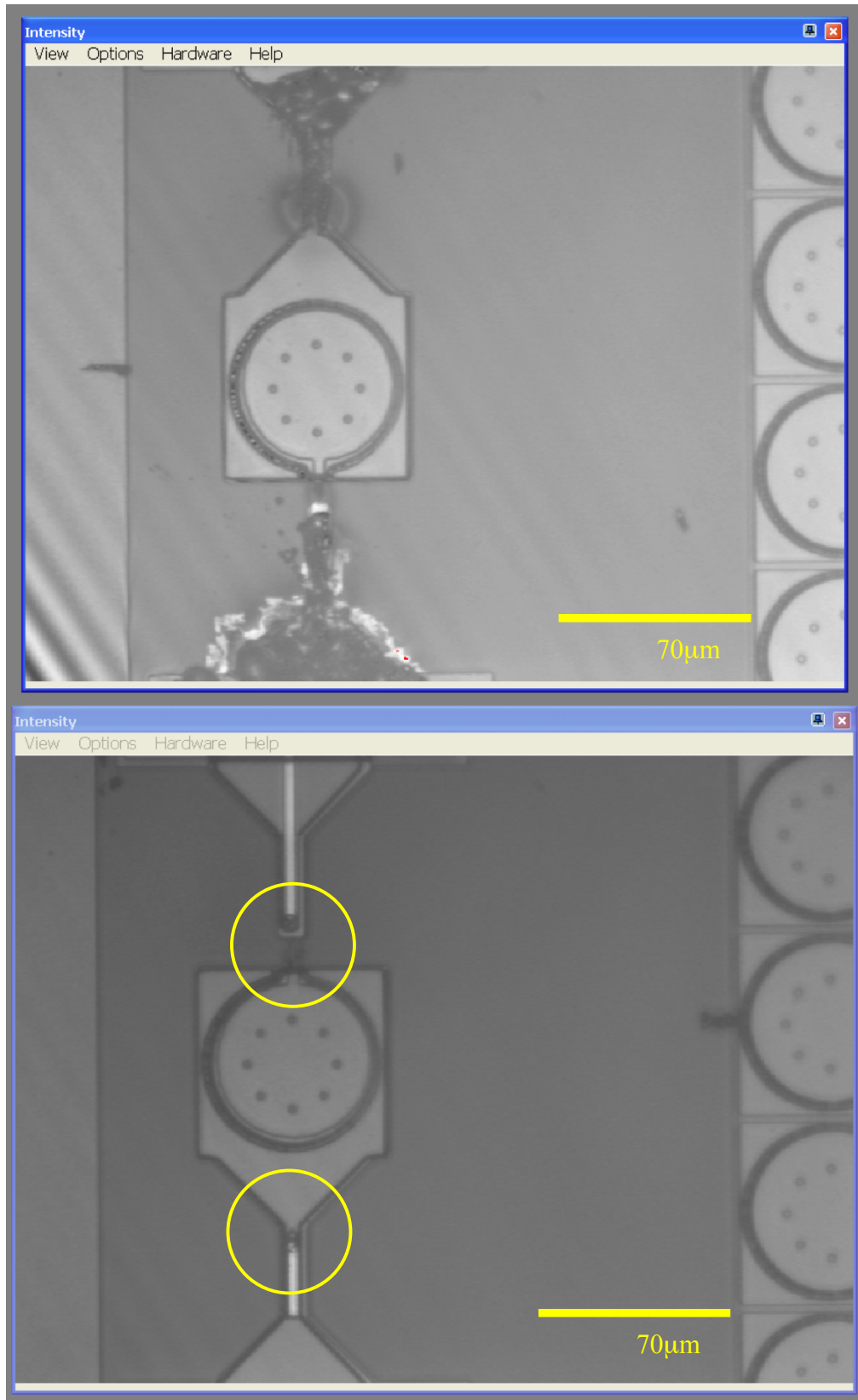


Figure 45. Photos of CMUT cells with burnt tracks after high current I-V characterization indicating presence of short-circuit on the dies

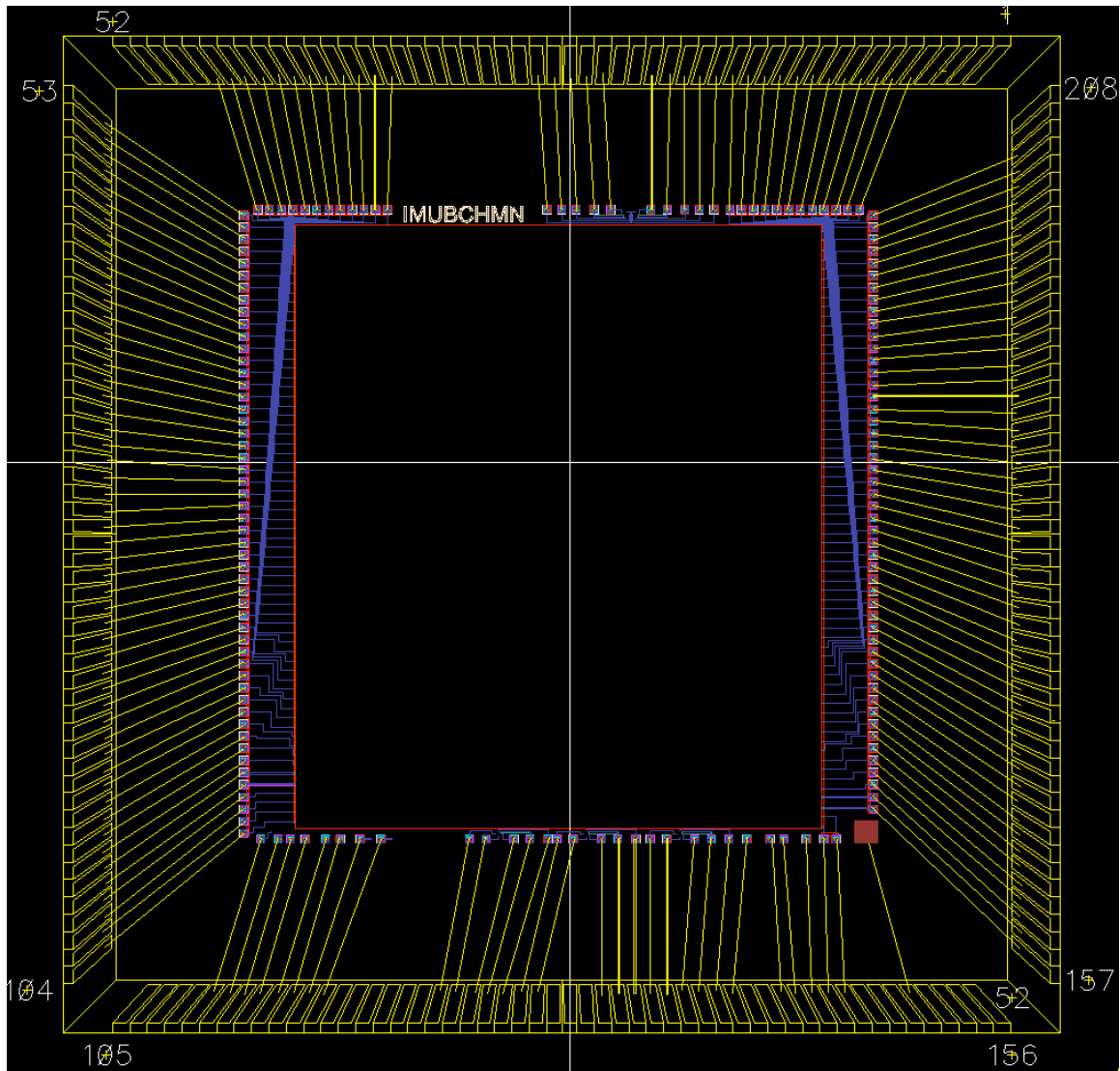
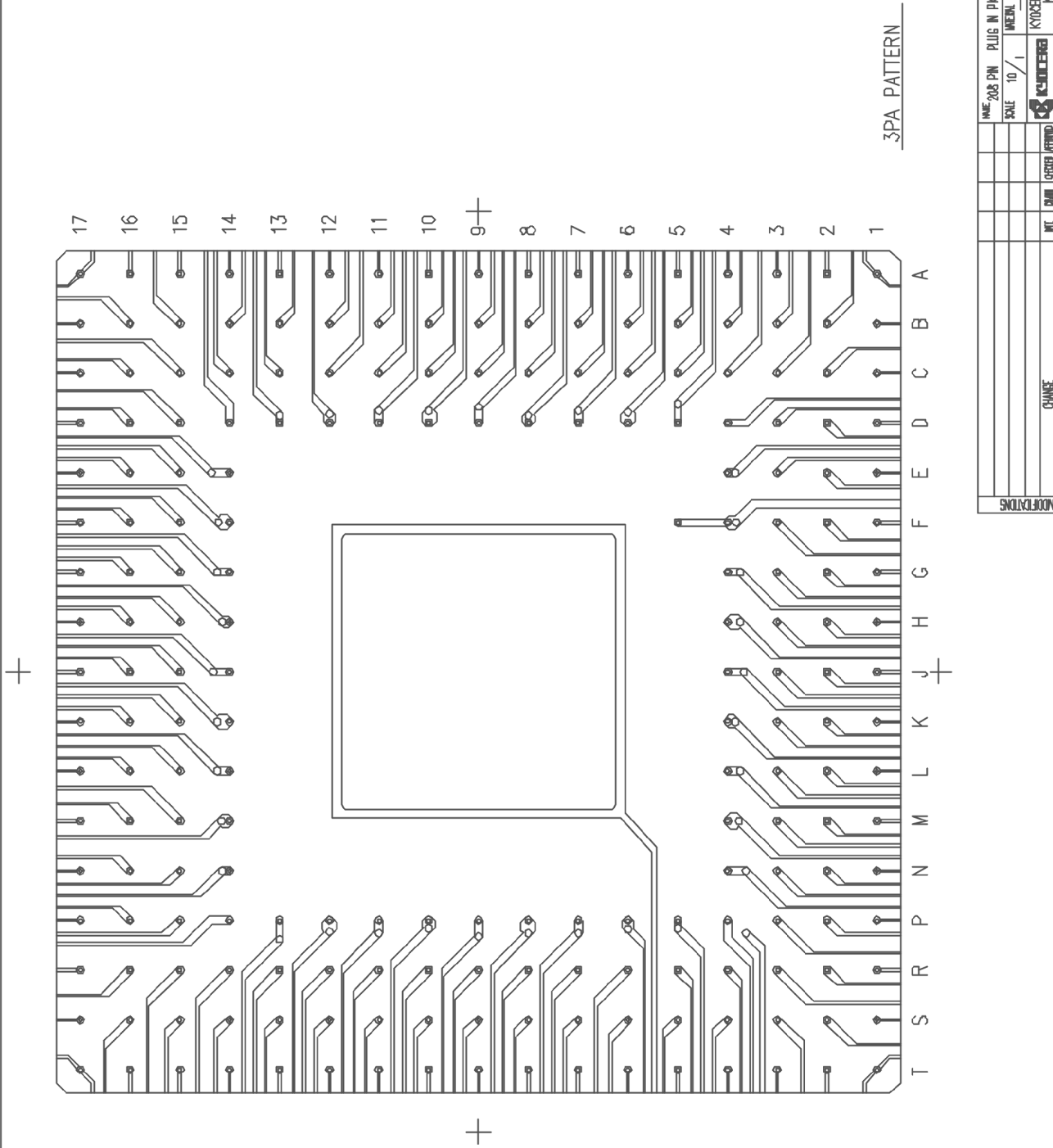


Figure 46. Pin configuration and the interconnecting tracks to the bond pads

Figure 47. PGA 209 package pin layout



REV. 1	DATE	12-27-78	DESIGNER	HI	CHKD	HI
REV. 2	DATE		DESIGNER		CHKD	
REV. 3	DATE		DESIGNER		CHKD	
REV. 4	DATE		DESIGNER		CHKD	
REV. 5	DATE		DESIGNER		CHKD	
REV. 6	DATE		DESIGNER		CHKD	
REV. 7	DATE		DESIGNER		CHKD	
REV. 8	DATE		DESIGNER		CHKD	
REV. 9	DATE		DESIGNER		CHKD	
REV. 10	DATE		DESIGNER		CHKD	
REV. 11	DATE		DESIGNER		CHKD	
REV. 12	DATE		DESIGNER		CHKD	
REV. 13	DATE		DESIGNER		CHKD	
REV. 14	DATE		DESIGNER		CHKD	
REV. 15	DATE		DESIGNER		CHKD	
REV. 16	DATE		DESIGNER		CHKD	
REV. 17	DATE		DESIGNER		CHKD	
REV. 18	DATE		DESIGNER		CHKD	
REV. 19	DATE		DESIGNER		CHKD	
REV. 20	DATE		DESIGNER		CHKD	
REV. 21	DATE		DESIGNER		CHKD	
REV. 22	DATE		DESIGNER		CHKD	
REV. 23	DATE		DESIGNER		CHKD	
REV. 24	DATE		DESIGNER		CHKD	
REV. 25	DATE		DESIGNER		CHKD	
REV. 26	DATE		DESIGNER		CHKD	
REV. 27	DATE		DESIGNER		CHKD	
REV. 28	DATE		DESIGNER		CHKD	
REV. 29	DATE		DESIGNER		CHKD	
REV. 30	DATE		DESIGNER		CHKD	
REV. 31	DATE		DESIGNER		CHKD	
REV. 32	DATE		DESIGNER		CHKD	
REV. 33	DATE		DESIGNER		CHKD	
REV. 34	DATE		DESIGNER		CHKD	
REV. 35	DATE		DESIGNER		CHKD	
REV. 36	DATE		DESIGNER		CHKD	
REV. 37	DATE		DESIGNER		CHKD	
REV. 38	DATE		DESIGNER		CHKD	
REV. 39	DATE		DESIGNER		CHKD	
REV. 40	DATE		DESIGNER		CHKD	
REV. 41	DATE		DESIGNER		CHKD	
REV. 42	DATE		DESIGNER		CHKD	
REV. 43	DATE		DESIGNER		CHKD	
REV. 44	DATE		DESIGNER		CHKD	
REV. 45	DATE		DESIGNER		CHKD	
REV. 46	DATE		DESIGNER		CHKD	
REV. 47	DATE		DESIGNER		CHKD	
REV. 48	DATE		DESIGNER		CHKD	
REV. 49	DATE		DESIGNER		CHKD	
REV. 50	DATE		DESIGNER		CHKD	
REV. 51	DATE		DESIGNER		CHKD	
REV. 52	DATE		DESIGNER		CHKD	
REV. 53	DATE		DESIGNER		CHKD	
REV. 54	DATE		DESIGNER		CHKD	
REV. 55	DATE		DESIGNER		CHKD	
REV. 56	DATE		DESIGNER		CHKD	
REV. 57	DATE		DESIGNER		CHKD	
REV. 58	DATE		DESIGNER		CHKD	
REV. 59	DATE		DESIGNER		CHKD	
REV. 60	DATE		DESIGNER		CHKD	
REV. 61	DATE		DESIGNER		CHKD	
REV. 62	DATE		DESIGNER		CHKD	
REV. 63	DATE		DESIGNER		CHKD	
REV. 64	DATE		DESIGNER		CHKD	
REV. 65	DATE		DESIGNER		CHKD	
REV. 66	DATE		DESIGNER		CHKD	
REV. 67	DATE		DESIGNER		CHKD	
REV. 68	DATE		DESIGNER		CHKD	
REV. 69	DATE		DESIGNER		CHKD	
REV. 70	DATE		DESIGNER		CHKD	
REV. 71	DATE		DESIGNER		CHKD	
REV. 72	DATE		DESIGNER		CHKD	
REV. 73	DATE		DESIGNER		CHKD	
REV. 74	DATE		DESIGNER		CHKD	
REV. 75	DATE		DESIGNER		CHKD	
REV. 76	DATE		DESIGNER		CHKD	
REV. 77	DATE		DESIGNER		CHKD	
REV. 78	DATE		DESIGNER		CHKD	
REV. 79	DATE		DESIGNER		CHKD	
REV. 80	DATE		DESIGNER		CHKD	
REV. 81	DATE		DESIGNER		CHKD	
REV. 82	DATE		DESIGNER		CHKD	
REV. 83	DATE		DESIGNER		CHKD	
REV. 84	DATE		DESIGNER		CHKD	
REV. 85	DATE		DESIGNER		CHKD	
REV. 86	DATE		DESIGNER		CHKD	
REV. 87	DATE		DESIGNER		CHKD	
REV. 88	DATE		DESIGNER		CHKD	
REV. 89	DATE		DESIGNER		CHKD	
REV. 90	DATE		DESIGNER		CHKD	
REV. 91	DATE		DESIGNER		CHKD	
REV. 92	DATE		DESIGNER		CHKD	
REV. 93	DATE		DESIGNER		CHKD	
REV. 94	DATE		DESIGNER		CHKD	
REV. 95	DATE		DESIGNER		CHKD	
REV. 96	DATE		DESIGNER		CHKD	
REV. 97	DATE		DESIGNER		CHKD	
REV. 98	DATE		DESIGNER		CHKD	
REV. 99	DATE		DESIGNER		CHKD	
REV. 100	DATE		DESIGNER		CHKD	

www.spectrum-semi.com Phone: 408.435.5555 Fax: 408.435.8226

